Structural analysis of the northeastern Mohns Ridge

Tor Erik Svendsen

Master of Science Thesis

Department of Earth Science
University of Bergen
2009

Abstract

A structural analysis of the northeastern Mohns Ridge situated in the Norwegian-Greenland Sea has been conducted using bathymetric data acquired during surveys in 2000 and 2001. Fault pattern and volcanic features are interpreted from this bathymetry as well as dip, length and displacement. These measurements have further been used to produce fault maps, profiles and models. The study area comprises the oblique spreading northern Mohns Ridge, the orthogonal spreading Mohns-Knipovich Ridge Bend and the southernmost highly oblique spreading Knipovich Ridge. Spreading rates lie between the slow- and ultraslow class of spreading ridges and the ridge is characterized by a deep rift valley.

Observations and interpretations of relay structures illustrate how faults link together and grow in both horizontal and vertical direction. Maximum displacement-length relation of the study area conforms to maximum displacement-length data from continental rift settings and other fault populations in spite of differences in crustal thickness and rheology.

The study area has been subdivided at segment scale. Area 1 is situated in between two axial volcanic ridges (AVRs) and area 2 has an AVR directly adjacent in the rift valley. Area 1 is characterized by rather symmetric fault geometry and in profile the faults are equally spaced and show a slight decrease in dip as distance off-axis increases. In contrast area 2 is characterized by great variations in topographic expression. It is characterized by several outward facing low-angle detachment faults with varying degrees of displacement as well as basins situated off-axis in relation to the detachment fault. These outwards facing faults have previously been interpreted to represent core complexes based on petrologic data although they are not structurally confined. Analysis has better confined these structures and their characteristics and proposed evolutionary models are presented. It is further suggested that several evolutionary stages of core complex formation is present in area 2.

The relative thermal state of the lithosphere is inferred to be the main reason for the difference in topographic characterization. It is suggested that higher heat flow and lithospheric temperatures at the AVRs result in local elevation of the brittle-ductile transition altering the rheological properties. This interplay between magmatic (volcanic) and amagmatic (tectonic) accretion is believed to result in oceanic core complex formation. Lateral termination of core complexes has not earlier been subject for debate. The higher heat flow and lithospheric temperatures in the vicinity of the AVR are believed to result in the lateral faults not propagating past the locally elevated brittle-ductile transition. This principal appears to conform to data from core complexes identified further south along the Mid-Atlantic Ridge.

Acknowledgements

I would like to express my gratitude to my supervisors Rolf-Birger Pedersen and Haakon Fossen. Thank you for interesting data to work with, as well as inspiring discussions. I am also sincerely appreciative for the input and guidance while analyzing and writing this thesis.

Thanks to Henry Dick for taking time to answering questions. A special thanks to Audun Libak for helping out whenever possible.

I would further like to thanks all my fellow students for great times at sea and in the field, as well here at the top of Nygårdshøyden at the University in Bergen.

To all my friends for support and patience, love all. Special thanks to Ida for being her wonderful self.

To my mother, father and brother, thank you for love and support as well as helping me achieve the goals I set for myself. I am forever grateful.

Tor Erik Svendsen
Bergen, June 2008

Table of content

1. INTRODUCTION

1.1. The study area

The study area is situated in the Norwegian-Greenland Sea and comprises the oblique spreading northern Mohns Ridge, the locally orthogonal spreading Mohns-Knipovich Ridge Bend as well as the highly oblique spreading southern Knipovich Ridge (red box in Figure 1.1). The ridge system is intermediate between the slow and ultraslow class of spreading ridges (Dick et al., 2003), and is therefore not intersected by first order transform faults. Instead the ridge is characterized by oblique segments defining second order segmentation. The complexity of this area result in several interesting features. The most striking is a dome-shaped structure off-axis that is elevated 2600 m in comparison to the rift valley. This structure has recently been reported to represent an oceanic core complex (Pedersen et al., 2007).

1.2. Main objectives

The data presented in this thesis consists of multibeam bathymetric data that was collected on behalf of the Norwegian Oil Directorate in collaboration with the University of Bergen in 2000-2001 as part of the "Law of Sea" project. The main objectives for this study are:

- Fault population and evolution – the role of relay structures
- Interplay between magmatic (volcanic) and amagmatic (tectonic) processes - comparison of two areas characterized by different heat flow and lithospheric temperatures
- Identify and constrain the presence of oceanic core complexes in the study area
- Constrain and discuss mechanisms controlling lateral termination of core complexes

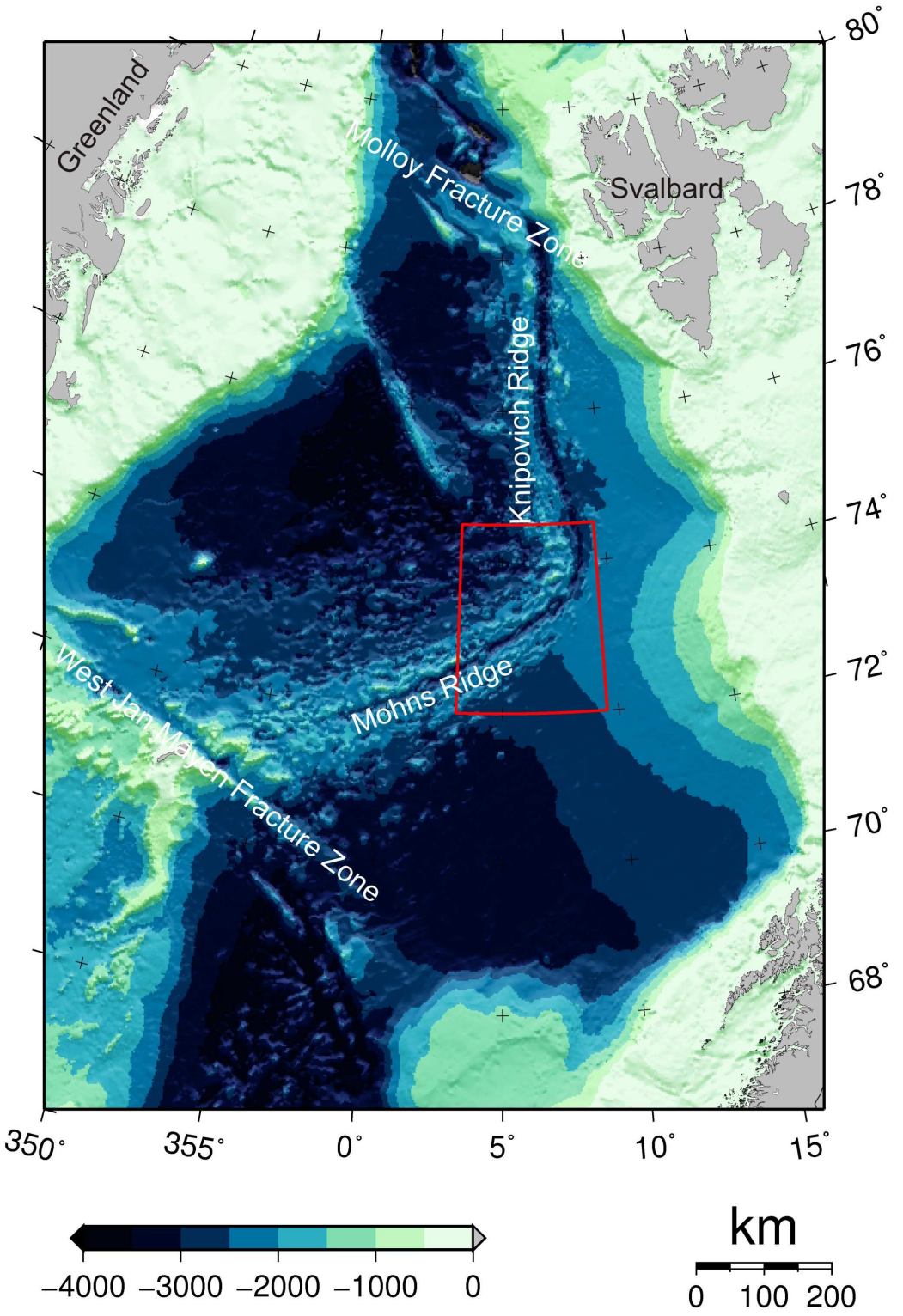

Figure 1.1: Depth-coded bathymetric map of the Norwegian-Greenland Sea with following continental margins. The red box shows the study area consisting of the northern Mohns Ridge, the Mohns-Knipovich Ridge and the southern Knipovich Ridge. The ridge segment is delimited by the West Jan Mayen Fracture Zone and the Molloy Fracture Zone. IBCAO bathymetric grid is used to generate this map (Jakobsson et al., 2008).

The objectives described above are to aid in better understanding of fault activity and mechanisms, spreading mechanisms and the role of AVRs at slow to ultraslow spreading ridges. Thus, the primary objective of the thesis is to better understand the tectonic complexity of the study area.

1.3. Approach

The approach has been to define two areas exhibiting different topographic expressions and proceed with structural geologic analysis. The results are presented in Chapter 4 where results concerning the axial valley for the study area are presented. Further the structural geologic results from the western flank for the subdivided areas are presented. Following is a section where detailed studies of structural features that aid to understanding the aims and objectives for this thesis are presented. The results presented in Chapter 4 are further discussed in Chapter 5 in light of the objectives.

2. GEOLOGICAL BACKGROUND

2.1. Mid-ocean ridges

Mid-ocean ridges are constructive plate boundaries where generation of new oceanic crust originates. They have been classified into three different classes (slow, intermediate and fast) based on their spreading rates (Macdonald, 1982). Each class has distinct morphologic characters (Figure 2.1). Fast spreading ridges have spreading rates greater than 90 mm/yr and have an axial high instead of a rift valley and show smooth topography with fine-scale horst and graben structures. Intermediate spreading ridges have spreading rates of 50 – 90 mm/yr with a 50 – 200 m deep median rift**.** Slow spreading ridges have spreading rates of 10 – 50 mm/yr. They exhibit a deep rift valley with depth of 1.5 – 3.0 km and the topography is rough and faulted (Macdonald, 1982).

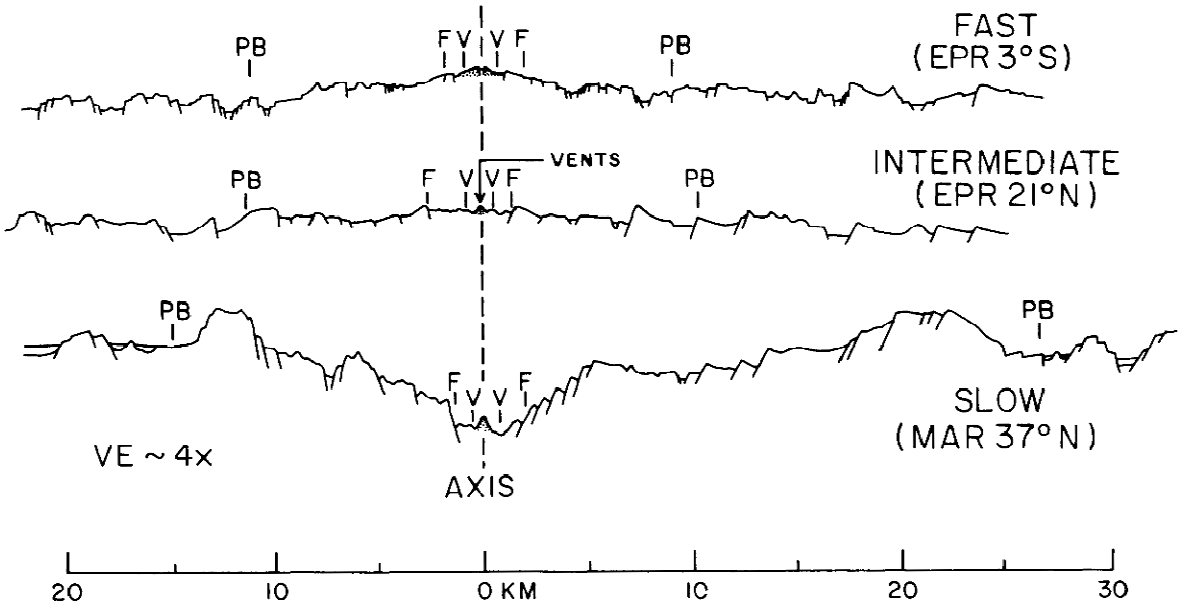

Figure 2.1: Bathymetric profiles for fast, intermediate and slow spreading ridges. PB indicates the extent of active faulting, F the zone of fissuring and V the zone of volcanism. Vertical exaggeration is 4 times. EPR – East Pacific Rise, MAR – Mid Atlantic Ridge (Macdonald, 1982).

The global mid-ocean ridge system is approximately 70.000 km long and the ridges are ~5 to 30 km wide. The mid-ocean ridges are structurally segmented by

discontinuities of different magnitude (Macdonald et al., 1988; Macdonald et al., 1991). First order segmentation is tectonically defined by transform faults that separate the spreading axis up to 1000 km and have a duration of ~10 Ma. The offsets are large enough that the lithosphere along the plate boundary behaves rigidly. The discontinuities divide parts of the global ridge system into 300 – 500 km long segments and these segments are associated with axial depth anomalies from 500 – 3000 m. Second order segmentation has lengths of 50 – 300 km and behaves non-rigidly in contrast to first order segmentation. The discontinuities are defined by smaller offsets of the spreading centre ranging from 2 – 30 km. At fast and intermediate spreading centers this is in form of overlapping spreading centers and at slow spreading centers in form of oblique shear zones. Second order segments have depth anomalies of ~100 – 1000 m and a duration between 0.5 – 10 Ma. Third and fourth order segmentation have a duration of 100 – 100000 Ma and have shallow depth anomalies ranging from 0 – 300 m. Third order segments are 30 – 100 km long and defined by small, 0.5 – 3 km, offsets in overlapping spreading centers. Fourth order segments are 10 – 50 km long and characterized by very small lateral offsets, <0.5 km, of the ridge. Third and fourth order discontinuities on slow spreading ridges are gaps in the axial neo-volcanic zone between volcanoes within the rift valley (Macdonald et al., 1988; Macdonald et al., 1991).

Phipps Morgan et al. (1994) suggests a balance between magmatic heat input and hydrothermal heat removal determining the thickness of the axial lithosphere, which in turn controls the axial morphology. Fast spreading ridges have continuous magma lenses at shallow depths implying a thin upper brittle layer that can easily be faulted or dissected by dikes. Slow spreading ridges have discrete and ephemeral magma chambers. Their lithosphere is thick and therefore exhibits a greater lithospheric strength and deep rift valley reliefs (Searle & Escartin, 2004).

Dick et al. (2003) proposed a new, ultraslow, class of spreading ridges. The subdivision of spreading ridges above is inadequate to characterize the ocean ridges' full variability. It is suggested that the classes should be divided into fast-, slow- and ultra-slow spreading ridges with two intermediates representing transition from fast-

to slow-spreading and slow- to ultra-slow spreading ridges. This is based on investigations of the Southwest Indian Ridge and the Arctic Ridges.

The ultraslow spreading class of ocean ridges have spreading rates less than 12 mm/yr and their characteristics can also be found where spreading rates approach 20 mm/yr. They are characterized by lack of transform faults and intermittent volcanism. The crust is thin and often absent, exposing mantle rocks on the seafloor and at fault scarps. Accretion of ridge segments happens by magmatic and amagmatic spreading, the latter newly recognized as a spreading mechanism (Dick et al., 2003)**.** The only ultraslow spreading ridge is the Gakkel Ridge in the Arctic Ocean which is without transform faults and spreading 8 - 13 mm/yr. The rest of the Arctic spreading system as well as the Southwest Indian Ridge show characteristics of this class with spreading rates ranging between 13 – 18 mm/yr (Dick et al., 2003).

The seismically determined oceanic crust is 7+/−1 km thick and decreases sharply at spreading rates lower than 20 mm/yr, indicating reduction of melt volume generated. The reduction is caused by conductive heat loss from the mantle welling up beneath rifts. Conduction is especially important for slow and ultraslow spreading ridges due to their large normal faults and thin crust that promotes penetration of water into the lithosphere (Bown & White, 1994; White et al., 2001; Robinson et al., 2001).Thus changes in ridge geometry, mantle composition, flow and thermal structures greatly affect crustal production and tectonics at very slow spreading rates (Dick et al., 2003)**.** From earlier work the ultraslow Gakkel Ridge would be predicted to have sparse volcanism, diminishing as the spreading rate decreased, and little hydrothermal activity (Baker et al., 1996; Bown & White, 1994). Michael et al.'s (2003) work on the ultraslow Gakkel Ridge revealed that magmatic variations are irregular and more robust than anticipated and that hydrothermal activity is abundant.

Ultraslow spreading ridges consist of magmatic (volcanic) as well as amagmatic (tectonic) segments. Magmatic segments are morphologically linear axial highs or troughs formed sub-perpendicular to the least principal compressive stress. Amagmatic accretionary ridge segments are the key component of ultraslow spreading ridges as they replace transform faults while extending the zone of

lithospheric accretion. They assume any orientation relative to the spreading direction and are distinguished by an axial through typically at depth up to 1 km and may extend 50 km or more. The ridges have scattered volcanics and or a thin basalt cover and oceanic layer 3 is thin and often absent. They expose abundant mantle peridotite, exhibit weak magnetization and a relatively positive Mantle Bouger Anomali (Dick et al., 2003). Further Dick et al. (2003) shows that the basic accretion unit appears to be mantle horst blocks that are subsequently uplifted to create an axial trough wall often creating low-angle (14°-20°) fault surfaces exposing peridotite ridges.

2.2. The opening of the Norwegian-Greenland Sea

The Norwegian-Greenland Sea (Figure 2.2) is defined as the deep ocean between northwest Europe and Greenland delimited in the north by the Spitsbergen Fracture Zone and in the south by the Greenland-Iceland-Faeroe shallow transverse (Eldholm et al., 1990). Comprehensive reviews of the Norwegian-Greenland Sea have been published (e.g. Eldholm et al., 1990; Talwani & Eldholm, 1977; Vogt, 1986) and it is evident that the sea comprises a complex system of active and aborted spreading ridges.

The Iceland-Faeroe Ridge, the Reykjanes Ridge to the south and the Kolbeisey Ridge to the north are unusually shallow (Talwani & Eldholm, 1977). The Mohns Ridge is symmetrical, situated between Greenland and Norway, and has a well developed magnetic pattern associated with seafloor spreading (Talwani & Eldholm, 1977). The Kolbeisey ridge south of the Mohns Ridge and the Knipovich Ridge to the north are situated asymmetrically between Greenland and Europe and this has affected the general physiography of the Norwegian-Greenland Sea (Eldholm et al., 1990). The deep ocean divides into three regions separated by fracture zones (Figure 2.2). The southern region consists of the Iceland Plateau and the Norwegian basin including the Aegir Ridge. The region is bounded by the Greenland-Iceland-Faeroe shallow transverse to the south and the Jan Mayen Fracture Zone (JMFZ) to the north. The central region comprises the Lofoten Basin and the Greenland Basin and is bounded by the JMFZ to the south and the Greenland-Senja Fracture Zone to the north. The northern region lies between the Greenland-Senja and Spitzbergen fracture zone and

consists of the Boreas Basin and a smaller basin between the Hovgaard and Molloy fracture zones (Eldholm et al., 1990).

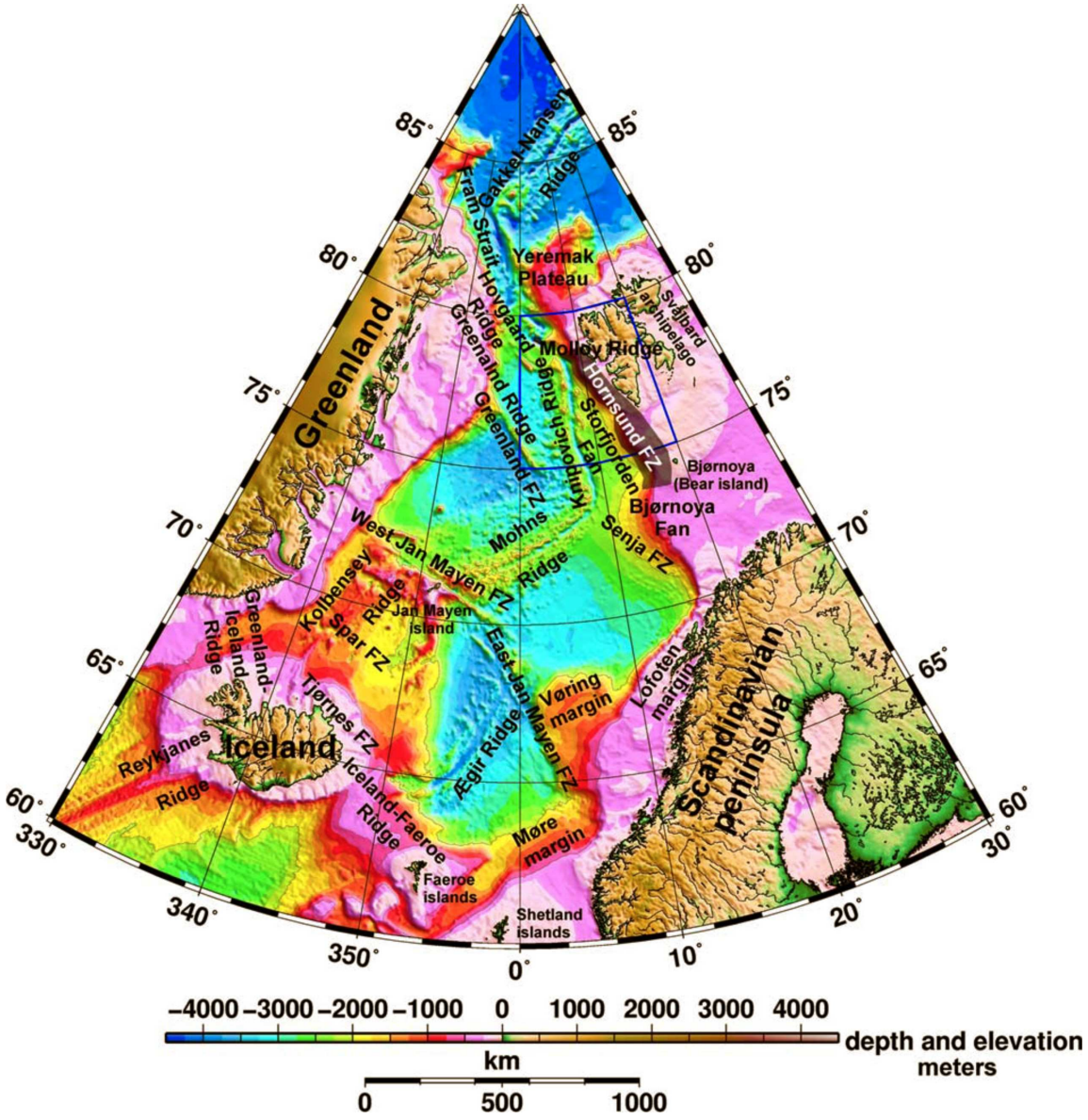

Figure 2.2: Bathymetric map with main geological features of the Norwegian-Greenland Sea (Kandilarov et al., 2008).

The separation of Norway and Greenland started with the collapse of the Caledonian mountain range in Devonian. From the collapse of the Caledonians until the beginning of Tertiary the area between Norway and Greenland was characterized by continental extension. Although the opening is a newer feature its segmentation and evolution are governed by pre-opening events (Hinz et al., 1993).

It is assumed that seafloor spreading in the Norwegian-Greenland Sea started in Early Eocene time (chron 24B, 53.7Ma) (Lundin & Dore, 2002; Talwani & Eldholm, 1977). From the initial break up until early Oligocene (chron 13, 35Ma) seafloor spreading occurred along the Reykjanes, the now extinct Aegir and the Mohns spreading axes (Figure 2.3a). The spreading in the Norwegian-Greenland Sea was connected to the Gakkel Ridge in the Arctic-Eurasian basin by a right-lateral transform consisting of the Senja Fracture zone, Hornsund fracture zone and Greenland fracture zone (Lundin & Dore, 2002).

In early Oligocene, chron 13 (Figure 2.3b), the spreading in the Labrador Sea and Baffin Bay ceased and the Greenland plate merged with the North American Plate (Lawver et al., 1990). The plate geometry in the vicinity of the Norwegian-Greenland Sea went from a three-plate to a two-plate configuration. Thus, the opening can be described as a separation of the North American Plate and the Eurasian Plate (Kristoffersen & Talwani, 1977). The spreading direction had thus changed from a NNW-SSE to a NW-SE orientation (Lundin & Dore, 2002). This rotation can be seen in the difference in trend between the East and West JMFZ. The change in plate motion caused rifting along the continental right lateral transform between SW Barents Sea and NNE Greenland initiating seafloor spreading along the Knipovich Ridge (Lundin & Dore, 2002). At the same time the Mohns Ridge went from orthogonal to oblique spreading. Crane (1988) proposes that the Knipovich Ridge formed by propagation from the south into the ancient Spitzbergen Shear Zone. Oceanic crust formed en echelon with smaller spreading basins propagating northward.

Spreading ceased along the Aegir Ridge around chron 6 (Figure 2.3c) and the spreading shifted westward (Lundin & Dore, 2002; Talwani & Eldholm, 1977). Talwani and Eldholm (1977) suggested a complex westward migration of the ridge to its present position, the Kolbeinsey Ridge. Other authors suggest a ridge jump directly from the Aegir Ridge to the Kolbeinsey Ridge (Kodaira et al., 1998a). ~20 Ma ago the Kolbeinsey Ridge and the Mohns Ridge were connected through the West JMFZ (Vogt, 1980). The Jan Mayen micro continent was evidently a part of eastern

Greenland before the spreading axis shifted to underneath the east coast of Greenland (Eldholm et al., 1990; Kodaira et al., 1998b). The plate configuration that followed the separation of the Jan Mayen micro continent and the linkage of the Kolbeinsey Ridge and the Mohns Ridge is the same configuration as is present today (Lundin & Dore, 2002).

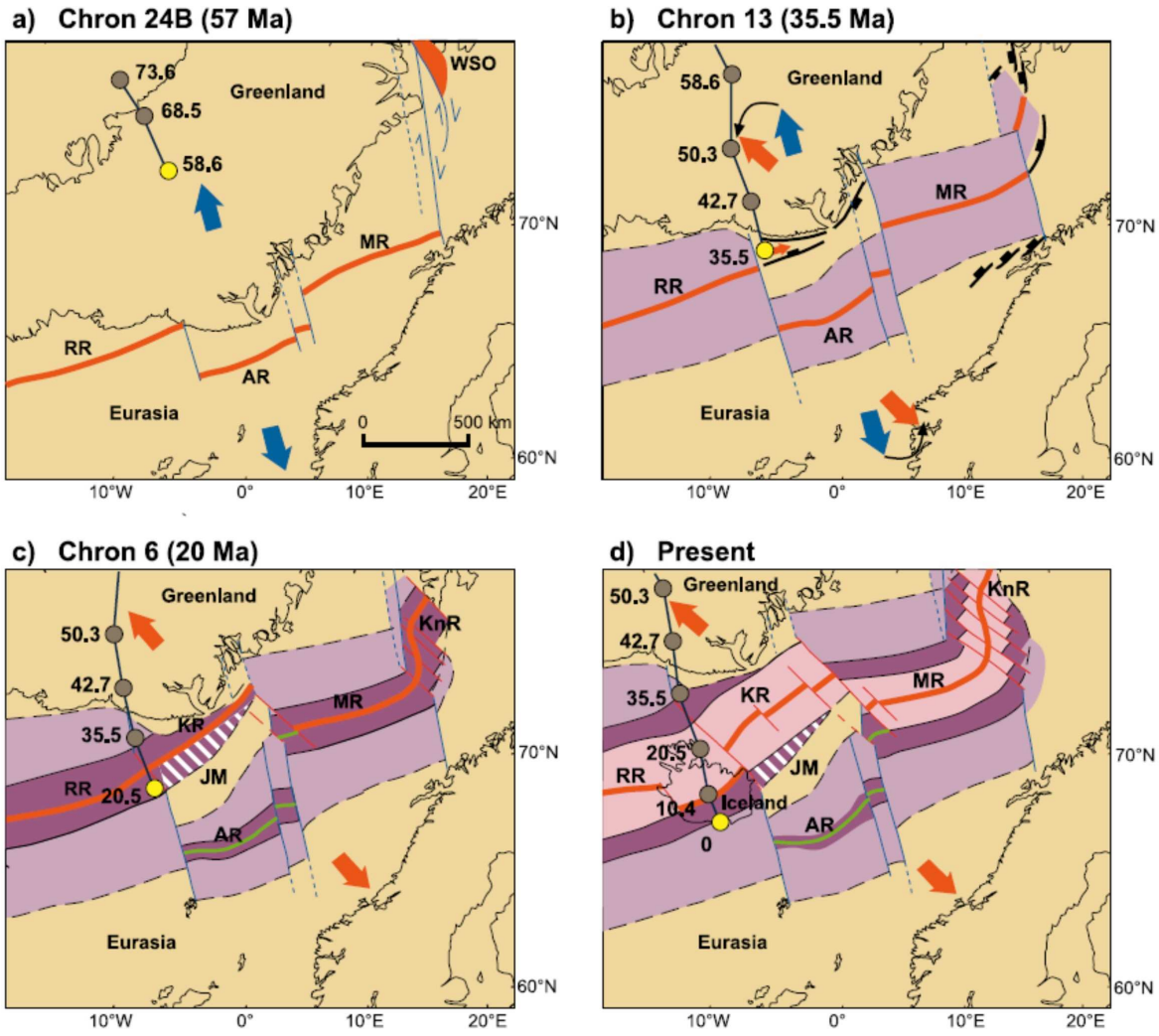

Figure 2.3: Plate tectonic evolution of the Norwegian-Greenland Sea (Lundin & Dore, 2002). RR – Reykjanes Ridge, AR – Aegir Ridge, MR – Mohns Ridge, WSO – West Spitzbergen Orogeny, KR – Kolbeinsey Ridge, KnR – Knipovich Ridge, JM – Jan Mayen micro continent. Gray and yellow dots respectively represent the paleo and current position of the Iceland Plume for the reconstruction (Torsvik et al., 2001). Blue arrows show spreading until Chron 13, and the red arrows show spreading directions after Chron 13 until present (Ludin & Dore, 2002).

a) Initiation of seafloor spreading along RR, AR and MR, the spreading direction has the same orientation as the Jan Mayen Fracture Zone. Shear movement along the Barents Sea margin.

b) Rotation of the spreading direction as a consequence of the Greenland Plate merging with the north American plate. Initiation of spreading in the northern Greenland Sea along KnR.

c) The Aegir Spreading Ridge ceases to exist as the spreading jumps westward forming the Kolbeinsey Ridge which connects with the Mohns Ridge. The Jan Mayen micro continent becomes separated from Greenland
d) The plate configuration in Chron 6 is maintained to the present.

The anomalous amount of magmatism in the North Atlantic area, from ~70 Ma to present, has been attributed to the Icelandic plume (Figure 2.3 shows the plumes path). This may have implication for the post breakup volcanism in the Labrador Sea rift as well as the separation of the Jan Mayen micro continent, the latter propagating northward as it split from Greenland (Mjelde et al, 2008). Breivik et al. (2006) proposed that the unusually thin oceanic crust at the ultraslow spreading morphology in the Norwegian Basin is caused by an interaction with the Iceland plume. The mantle was depleted during the construction of the magmatic Greenland-Iceland-Faeroe Ridge resulting in slow but persistent asthenospheric flow northeastwards to the Norwegian Basin giving a lower than normal magma productivity during seafloor spreading. Figure 2.2 and 2.3d show present configuration of the Norwegian-Greenland Sea.

2.3. The Mohns Ridge

The Mohns Ridge (Figure 1.1) extends from the Jan Mayen Fracture Zone northeastwards until it bends northwards into the Knipovich Ridge at 74°N and is approximately 600 km long (Hellevang & Pedersen, 2003). The ridge is oriented ~60° and the spreading direction since magnetic anomaly 7 is 115° (Vogt, 1986) thus this is an oblique spreading ridge. The degree of oblique spreading is defined by the angle between the normal to the axis and the direction of spreading (Abelson & Agnon, 1997), giving a spreading that is oblique by 35°. Hellevang and Pedersen (2003) calculated the obliquity to change from 30° east of Jan Mayen to 24° in the northeast part of the ridge and orthogonal in the Mohns–Knipovich Bend. Analyzing magnetic anomalies, Talwani and Eldholm (1977) calculated the spreading rate to be ~9 mm/yr for the last 10 Ma while newer calculation by Mosar et al. (2002) calculated the spreading rate to be ~16 mm/yr for the last 10.3 Ma. Thus the Mohns Ridge is

intermediate between slow and ultraslow spreading according to Dick et al. (2003) classification of spreading ridges.

Klingelhofer et al. (2000a & b) interpreted the crust at the Mohns Ridge to be 4.0 ± 0.5 km thick using seismic refraction data. Oceanic layer 2a and 2b show nearly normal thickness and oceanic layer 3 is very thin. Variations in crustal thickness are due to changes in seismic layer 3 and it appears to thicken below topographic highs and to thin below local basins. Due to the presence of the Iceland hot spot, and also perhaps the Jan Mayen hot spot (Neumann & Schilling, 1984), the rift valley is relatively shallow compared to the rest of the Mid-Atlantic Ridge. It deepens progressively from 2500 – 3000 m near the JMFZ northeastwards to depths of 2800 – 3500 m. The rift valley is generally 10 – 20 km wide and 1 – 2 km deep with exception of a width of 1.5 km on the Jan Mayen Platform and approximately 5 km at the Mohns – Knipovich Bend (Geli et al., 1994; Hellevang & Pedersen 2003). The Mohns Ridge, as well as the Knipovich Ridge, is not cut by transform faults defining first-order segments. Instead they are regions of linked magmatic and amagmatic ridge segments (Dick et al., 2003).

There are several articles covering the central part of the Mohns Ridge (2°W - 4°E) discussing fault-pattern and segmentation based on detailed swath bathymetry as well as seismic, gravity and magnetic data (Dauteuil & Brun, 1993 & 1996; Geli et al. 1994; Hellevang & Pedersen, 2003). The central Mohns Ridge is characterized by large-scale segmentation with en echelon arranged topographic highs separated by transfer zones (Dauteuil & Brun, 1993 & 1996). Dauteuil & Brun (1993) proposed that the topographic highs in the axial valley are of tectonic origin, being bounded by large vertical offset indicate that they are horsts. Geli et al. (1994) suggests that the topographic highs are of volcanic origin due to sharp positive magnetic anomalies. The latter is consistent with side-scan images from the northern Mohns Ridge and Mohns-Knipovich Ridge Bend where the topographic highs occurring every 32 to 67 km are interpreted as volcanically active areas (Crane et al., 1999). Crane et al. (2001) and Okino et al. (2002) show that the Knipovich Ridge is segmented similarly to the Mohns Ridge but with larger distances between the topographic highs (85 - 100 km).

The Mohns Ridge border faults are asymmetric with larger throws on the northwestern flanks resulting in shallower bathymetry. The southeastern flank shows an apparently more simple morphology due to thicker sediment piles than the northwestern flanks (Talwani & Eldholm, 1977; Dauteuil & Brun, 1996). The faults within the axial valley are linear or smoothly curved, forming a mean 30° angle to the rift valley. As the faults approach the rift valley walls they are curved and become parallel to the valley walls (Dauteuil & Brun, 1993).

Hellevang & Pedersen (2003) subdivided the Mohns Ridge into 15 second-order segments with distances of 18 to 64 km. The second-order segment centers are identified by shallower bathymetry and stronger magnetic anomalies within the rift valley, defining axial volcanic ridges (AVRs). The transition between the segments is considered to represent second-order discontinuities and the Jan Mayen Fracture Zone and Molloy Fracture Zone are considered to represent first order ridge discontinuities. The entire Mohns and Knipovich Ridge can thus be described as a “supersegment” (Dick et al., 2003). Subdivision into third and fourth order segments is related to depth variations associated with the discontinuities and offsets between the segments. They are believed to be controlled mainly by variations in along-axis magmatic activity. Increasing mantle bouguer anomalies (MBA) away from the Jan Mayen Platform indicates decreasing crustal thickness and lower magmatic activity northeastwards resulting in deeper bathymetry and longer distances between AVRs.

2.4. Oceanic core complexes

Oceanic core complexes are massifs in which lower crust and upper mantle material are exposed on the seafloor. They are comparable to continental core complexes and are interpreted to be rotated footwall blocks associated with low-angle detachment faults (e.g. Tucholke & Lin, 1994; Blackman et al., 1998; Tucholke et al., 1998; Ranero & Reston, 1999; Cann et al., 2001; Reston et al., 2002). The core complexes where initially discovered at the inside corners of ridge transform intersections along slow spreading ridges. More recent research (e.g. Okino et al. 2004; Smith et al., 2006) reports oceanic core complexes between ridge-transform intersections as well.

Pedersen et al. (2007) and Bruvoll et al. (2009) report the presence of core complexes west of the Mohns-Knipovich Ridge Bend where gabbro and serpentinite have been recovered on low-angle fault surfaces.

It is believed that prolonged slip on a detachment fault occurs where a ridge segment experiences a phase of relatively amagmatic (tectonic) extension as it is easier to maintain slip on an existing fault than it is to initiate a new fault in the strong rift valley lithosphere of a slow spreading ridge. The detachment fault will be terminated when a magmatic phase occurs, because magmatism will weaken the axial lithosphere so that it becomes easier to initiate a fault closer to the rift valley (Tucholke et al., 1998). The transition from dislocation creep to diffusion creep in shear zones near the brittle-plastic transition in the mantle contributes to fault weakening (Jaroslow et al., 1996). Escartin et al. (1997) suggests that variations in faulting style can be explained by rheological effects of serpentinization. Here strength versus depth profiles calculated to suit slow spreading ridge systems indicate that the presence of serpentinite can reduce the strength of the lithosphere by up to 30%, favoring more widely spaced faults with greater throw in contrast to deformation where serpentinite is scarce. Thus the long-lived slip can be explained by amagmatic extension as well as fault weakening due to presence of serpentinite and change in deformation mechanism.

Morphological characteristics common for oceanic core complexes can be illustrated from an inactive core complex near 30°N at the Mid Atlantic Ridge (Figure 2.4). An isochron-parallel ridge exhibiting a steep slope facing away from the spreading axis is present. Rocks recovered from this particular ridge show that it is composed of basalt and interpreted to represent volcanic seafloor created at the axis (Smith et al., 2006). A not as illustrious feature in the example presented, but commonly found immediately towards the rift axis, is a narrow zone of depressed crust. A basin is situated immediately behind the former mentioned ridge (away from the axis), and such basins are believed to be formed by outward footwall rotation as the ridge evolves (Smith et al., 2006). Towards the axis from the ridge a broad uplifted dome-shaped massif is present. The surface of this massif is corrugated and dredges have recovered serpentinized peridotite (Smith et al., 2006). Such massifs have been

interpreted to be fault surfaces of detachment faults in association with core complexes (Tucholke et al., 1998; Smith et al., 2006). In Figure 2.4 a normal fault scarp cuts the feature on its inner (younger) side and the scope to the northwest of the massif indicates mass wasting (Smith et al., 2006).

An additional common feature for an extinct core complex is that the corrugated massif often dips at a low angle intersecting the seafloor. This is interpreted as the termination of the detachment fault which is in association with the core complex. This is due to a new fault that has formed further towards the axis (Tucholke et al., 1998). Throughout this thesis the fault forming towards the axis, aborting the core complex evolution, is referred to as the termination fault. The expression termination used by Tucholke et al. (1998) is referred to as the tip of the detachment. The exposed detachment surface comprising the core complex is referred to as the core complex extent in map view. The detachment fault for an active fault in a core complex setting is rooted below the spreading axis when active (Tucholke et al., 1998).

The corrugated fault surfaces, also referred to as mullion structures, are parallel to the spreading direction and consist of synforms and antiforms with amplitude up to ~100 m (Tucholke et al., 1998; Smith et al., 2006). The origin of the corrugations is still not fully understood. Direct observations have showed that they are not produced by faults parallel to the spreading direction (Tucholke et al., 2001). A possibility is that they originate by continuous casting where the footwall behaves in a ductile manner and is deformed with respect to irregularities in a strong and brittle hanging wall (Spencer, 1999). The domed massif can be explained by regional isostatic compensation and flexure due to large fault throw (>5 km) which domes the fault surface of the footwall (e.g. Buck, 1988). Numerical modeling ascribes the domed feature to be due to plastic and elastic deformation (Lavier et al., 1999). The zone of depressed crust, between the outward dipping slope and the dome, is interpreted to be formed by high angle faults dissecting the detachment surface (Tucholke et al., 1998). Newer research (Smith et al., 2006) alternatively assumes that the depressed zone corresponds to upper crust that is not characterized by flexure and isostatic compensation.

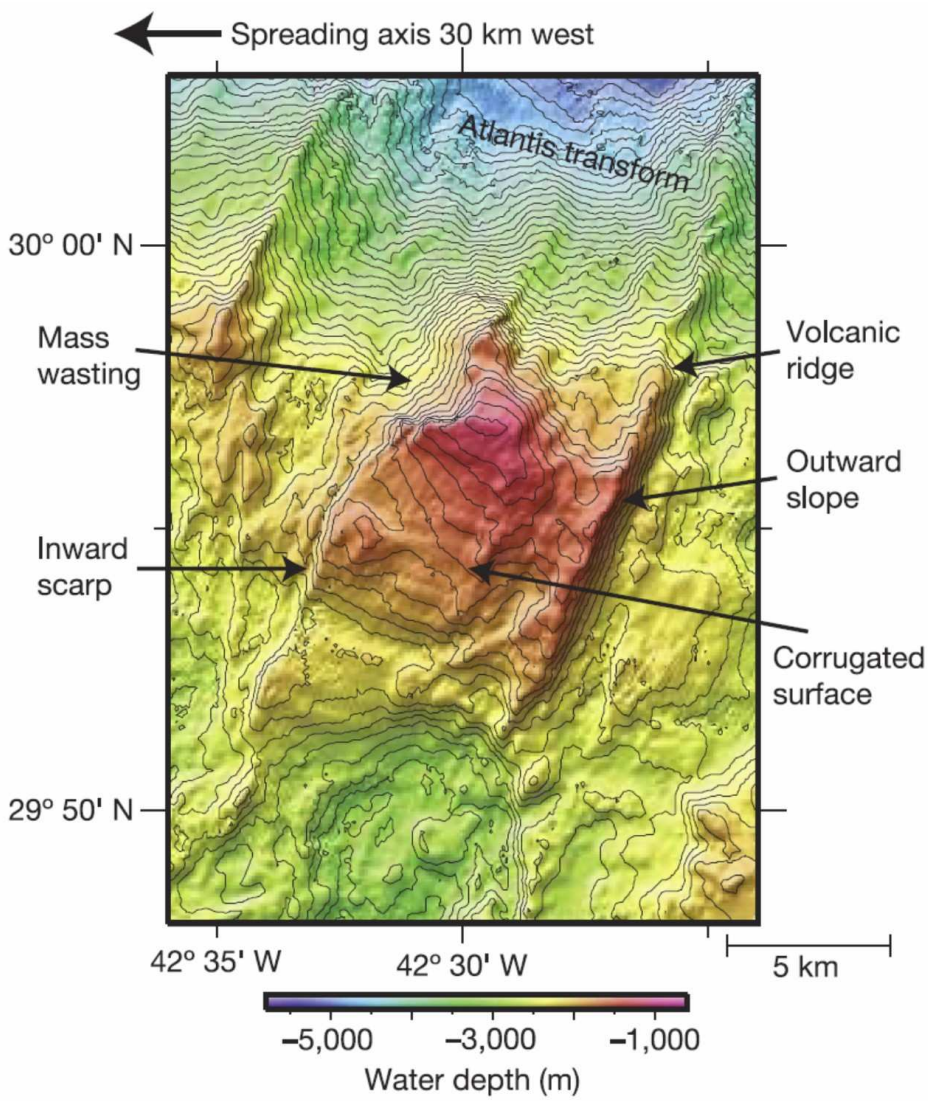

Figure 2.4: Color coded bathymetric map of a well-exposed, extinct core complex south of the Atlantis fracture zone on the Mid Atlantic Ridge. Map contour interval is 100 m. Morphological characteristics are shown by arrows and discussed in the text (Smith et al., 2006).

3. DATA AND METHOD

3.1. Data

Bathymetric data covering the northern Mohns Ridge and the Mohns-Knipovich Ridge Bend (Figure 3.1) is interpreted and presented in this thesis. The data was collected on behalf of the Norwegian Oil Directorate in 2000 – 2001 by Gardline Surveys and Fugro Geoteam for the "Law of Sea" mapping. Multi-beam bathymetric data (swath bathymetry) was collected using a Simrad EM120 echosounder (12 kHz transducer frequency) installed onboard MV Ocean Endeavour. The quality of the data was improved by removing the outer 5 beams on both sides of the swathe and filtering the remaining data to compensate for weather conditions, sound velocity errors, standard deviations, noise and residual differences. Additional interference was caused by the sub bottom profiler and was addressed by a synchronization unit that was fitted to the pinger suit (Gardline Surveys Limited, 2001). The final charts where gridded and the program Fledermaus was used to view and shade the bathymetry. The data was produced with a resolution of 200 m x 200 m. The University of Bergen has since re-gridded the bathymetric maps in Fledermaus to a resolution of 75 m x 75 m.

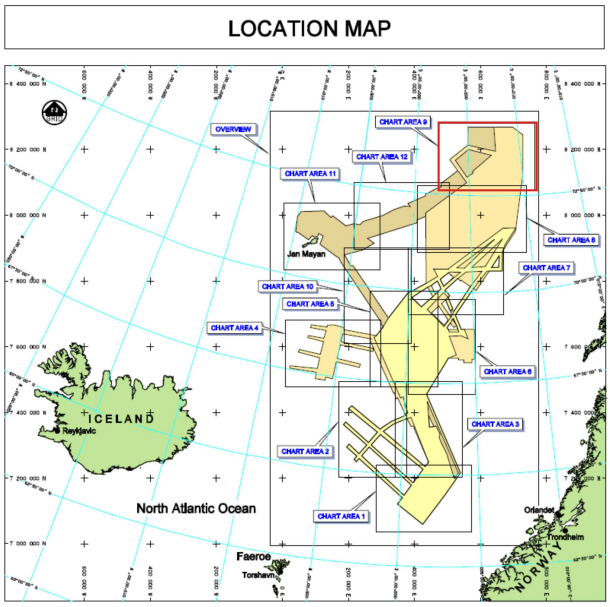

Figure 3.1: "Law of Sea" data acquisition. Chart area 12 (red outline) is subject to this thesis (Gardline Surveys Limited, 2001).

Fledermaus uses a UTM (Universal Transverse Mercator) based coordinate system. The system is based on representing a portion of the Earth as a flat surface. The data presented is in UTM zone 32 WGS 84. Captures from Fledermaus have shading from the northeast. On regional figures and maps UTM coordinates have been converted to geographical coordinates with exception of smaller detail studies where an outline is presented in a regional figure to illustrate its position. A regional map of the Norwegian-Greenland Sea has also been generated in GMT (Generic Mapping Tools) (Figure 1.1**)** to better illustrate the geographic position of the data.

3.2. Method and approach

Several tools are available to map deformation at mid-ocean ridges such as bathymetric data, seismic reflection and refraction data, acoustic imagery and submersible investigations. What makes bathymetry a powerful tool is the ability to visualize and correlate lineaments and structures at a large scale. In this thesis bathymetric data, from chart area 12 (Figure 3.1), is used to interpret the ridge system by studying the morphologies and doing measurements using the three-dimensional visualization program Fledermaus.

Tectonic interpretation of morphology seen on ridges is relatively straightforward as there are only two main processes controlling the bathymetry; tectonics and volcanism. Volcanism produces two identifiable features: conical structures and elongated domes with lower relief related to fissure eruption. Tectonic processes generate faults where vertical throw disturbs the bathymetry. This makes strike-slip faults barely visible except where they affect pre-existing structures (Dauteuil, 1995). It is thus important to remember that interpreted normal faults may have a strike-slip component. Due to resolution limitations only larger faults and volcanoes are visible and interpreted faults may in fact represent fault zones (Dauteuil & Brun, 1993; Hellevang & Pedersen, 2003).

A factor that disturbs interpretation is sedimentation and erosion altering the faulted topography. It has been shown by Bruvoll et al. (2009) that the proximity of the Mohns-Knipovich Bend to a glacial margin has resulted in accumulation of a

sediment cover that locally exceeds several hundred meters. This cover becomes progressively thinner away from the margin. Gravity cores from the upper 4 meters show iron- and glass-rich laminas and layers representing a history of hydrothermal deposits and volcanic activity in the area (Pedersen et al., 2007). Thus volcanism may alter the tectonic expression. Degradation of fault block crests due to mass wasting processes are recognized, causing accumulation of sediments in hanging wall depressions. This may be caused by gravitational instabilities in sediments or oceanic rocks overlaying the faults and may be triggered by earthquakes (e.g. Hesthammer & Fossen, 1999).

Measurements of fault throw have been extracted from profiles drawn perpendicular to faults and derived from the bathymetric data in Fledermaus. The footwall and hanging wall have to be interpolated to account for sediment accumulation in the depression as well as the footwall being interpolated to account for erosion. Figure 3.2 shows a schematic profile typical to the area demonstrating apparent throw and heave compared to interpreted throw and heave.

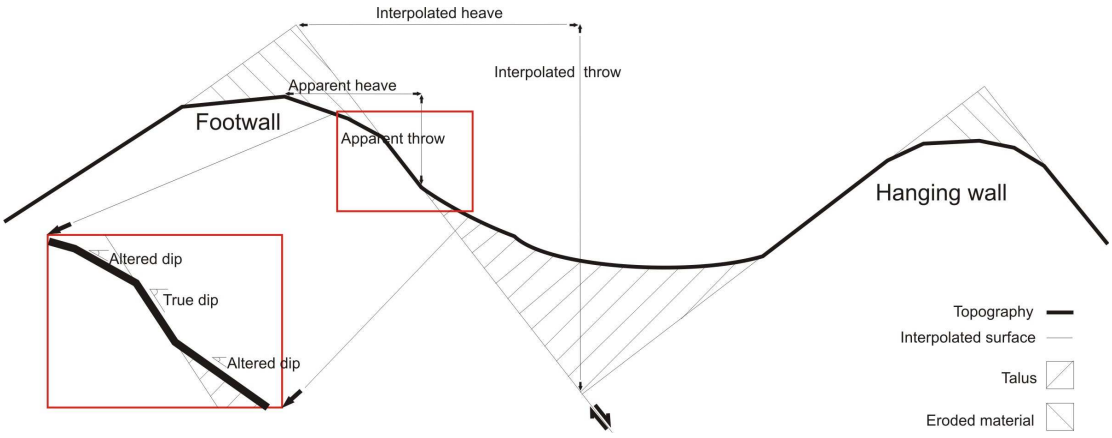

Figure 3.2: Illustration of some of the possible errors associated with measurements of fault throw and fault dip from bathymetric data. The uncertainties are due to mass wasting resulting in eroded crests and downslope accumulation of talus, as illustrated. As illustrated throw and dip easily becomes underestimated in the presence of mass wasting and fault-scarp degeneration.

Figure 3.3 shows an example how a profile drawn over a fault may look and how debris is identified in the bathymetric data. Throughout the study area there is a varying degree of depression infill and erosion of footwall tops, and this has been

accounted for in each measurement. Errors in measurements occur due to wrongful interpolation of footwalls and hanging walls and uncertainties when reading off values from the axis of the profiles in Fledermaus.

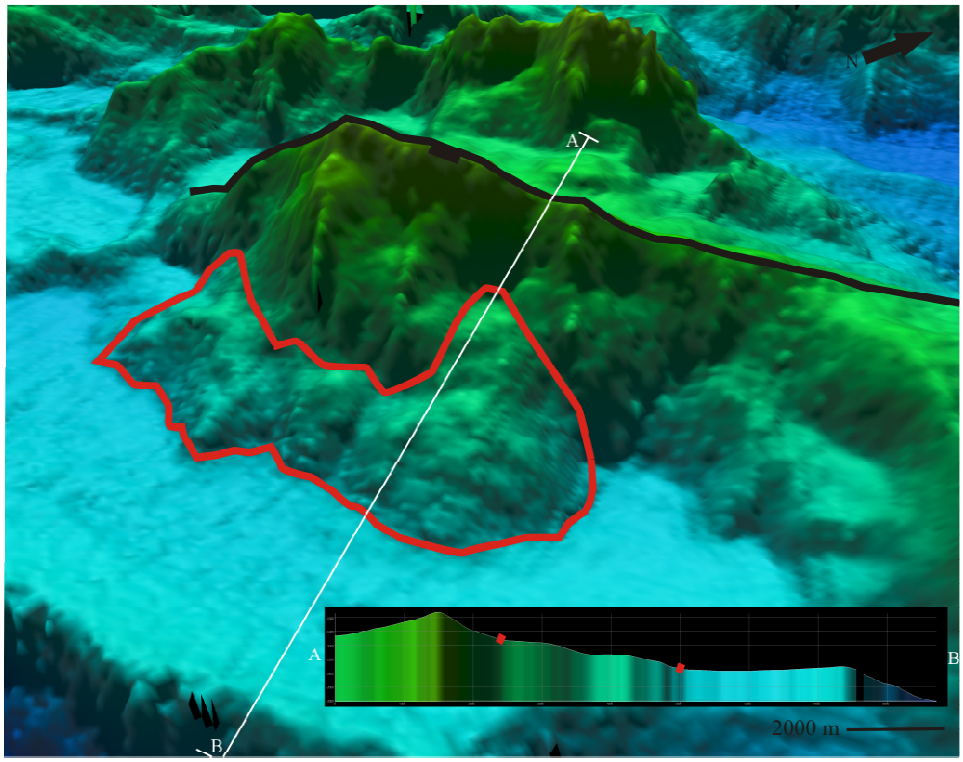

Figure 3.3: Example of what a profile (lower right corner) may look like and how a talus (red outline) is identified. Red ticks on the profile correspond to outline in the profile.

Additional factors to consider during interpolation is flexure (increasing relevance when fault spacing increases) and rugged (pre faulted) topography. This can be illustrated on a seismic line crossing the west flank of the southern Knipovich Ridge at 75°N (Figure 3.4). The seismic line shows how Figure 3.2 may be a reasonable approach for interpolation in some cases, e.g. faults with close spacing seen to the right in the blue box. To the left in the red box two faults with large spacing (ca. 6.5 km) show that the scheme illustrated in Figure 3.2 is not accurate. The area between the two major faults displays rugged topography and/or flexure of the hanging wall towards the footwall. In Allerton et al. (1996) investigation of valley-wall faulting and its relationship to bathymetry illustrates the fault scarp evolution. In the illustration two faults initiate at an immature stage. At a mature stage only one fault is active and the other fault becomes buried by sediments and may not be visible in the bathymetry. Figure 3.4 also illustrates how fault surfaces become altered by erosion and

sedimentation and may become buried after the faults become inactive. This is seen east of the blue box in the figure and makes the faults invisible from bathymetric data alone. There are several factors that may deviate from the schematic figure presented in Figure 3.2. The throw estimates used as a basis for the analyses in this work are thus an interpretation where such factors are taken into consideration.

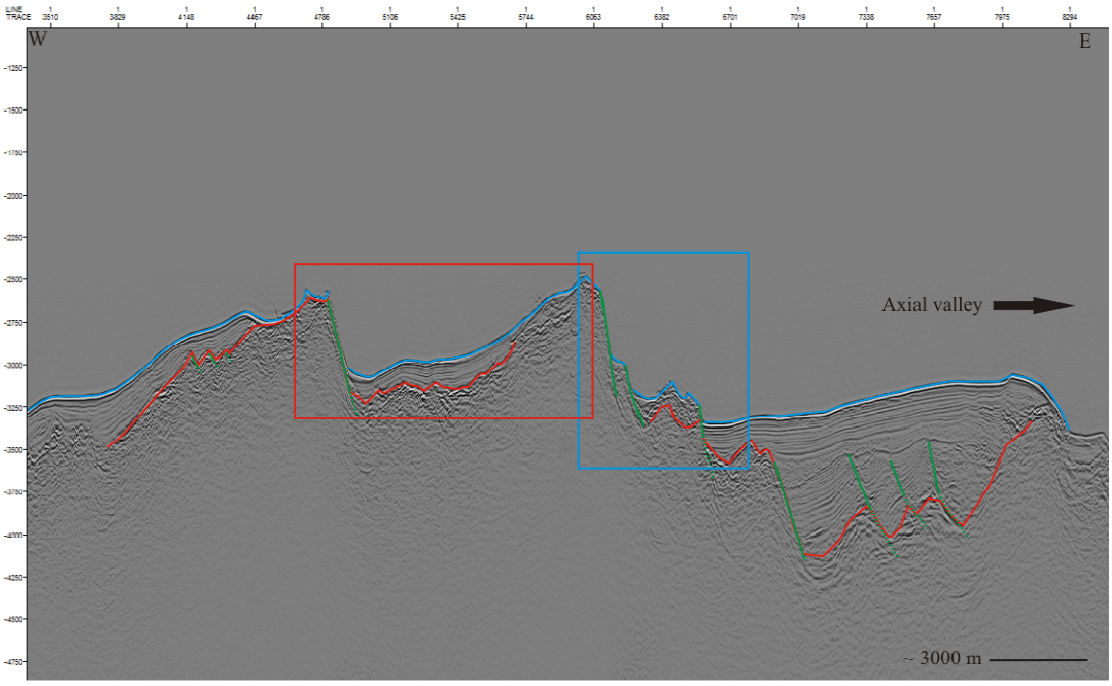

Figure 3.4: Seismic profile of the western Knipovich Ridge flank at 75°N. Blue line is interpreted seafloor, red line is interpreted basement, and green line is interpreted fault. Vertical axis is in ms and the horizontal axis is noted in CMP (common mid point).

The apparent lengths of faults are measured in map view. In cases where actual fault length is needed estimates are made by plotting throw and length in a graph and interpolating based on an expected displacement distribution, thus estimating actual length. Throw versus length was plotted in a log-log diagram for a number of single and linked faults to distinguish eventual trends. Figure 3.2 shows how dip can be wrongfully measured, this has been a challenge and the approach has been to measure along the lineament of interest and find an average estimate from areas where erosion and altering of the fault surface has not occurred. In the following “apparent throw” is referred to as “throw” unless otherwise noted. Profiles are made to document measurements as dip and fault spacing and are an important parameters for further interpretation of the tectonic characterization. Measurements of fault orientation have been presented as stereographic projections. The measurements are of the mean

orientation of the fault unless otherwise noted and the right-hand rule has been used. Obliquity of the axial highs has been measured by measuring the angle between the trend of the AVR and the trend of the mid ocean ridge orientation. Fault maps have been made for the study areas and specific structures of interest to better understand population and geometries. The faults are interpreted from ridges in the shaded bathymetry, and the dip direction is determined in profile by comparing dips on either side along the ridge. Few faults dipping away from the ridge have been observed, although there are reasons to believe that they may exist as others have interpreted horst blocks and antithetic faults in slow spreading ridge systems (Macdonald, 1982; Bruvoll et al., 2009).

4. RESULTS

4.1. Introduction

4.1.1. Subdivision of the study area

The study area (red box Figure 1.1) has been divided into two areas showing different topographic expressions of the western flank of the rift system (red boxes in Figure 4.1). The eastern flank is not as well exposed due to sediment cover derived from the glacial continental margin to the east. Area 1 is the northern part of the Mohns Ridge (~3.30°-6.30°E 72.30°-73.20°N) and is situated between segment center 12 and 13. Area 2 is the Mohns-Knipovich Bend (~6.30°-9.30°E 73.10°-74.20°N) and consists of segment 14 and 15 as well as the southern part of the Knipovich Ridge.

The results presented in this chapter are from profiles, stereographic projections, fault maps and throw-length relationships derived from the bathymetric data as well as the shaded bathymetric data itself. Before presenting the results a brief description of some of the terminology used in this and preceding chapters is presented.

4.1.2. Terminology

Rift segments are distinguished after Hellevang and Pedersens (2003) subdivision of the Mohns Ridge. Here the AVRs define centers of second-order ridge segments, and the gradual boundaries between these segments are second-order ridge discontinuities. Offsets between segments and tectonic dominated deep basins correspond to higher-order 3rd and 4th order segments.

Major faults with significant throw bounding and defining the rift valley and its trend are referred to as border faults whereas faults within the rift valley are referred to as intra-rift faults. The segment width is defined as the distance between the bordering normal faults. Relay ramps occur where two faults overlap. If the two faults are connected in map view they represent a hard-link structure. If they are not connected

in map view they represent a soft-link structure (Walsh & Watterson, 1991). Faults with low-angle dip and large amount of displacement are referred to as detachment faults.

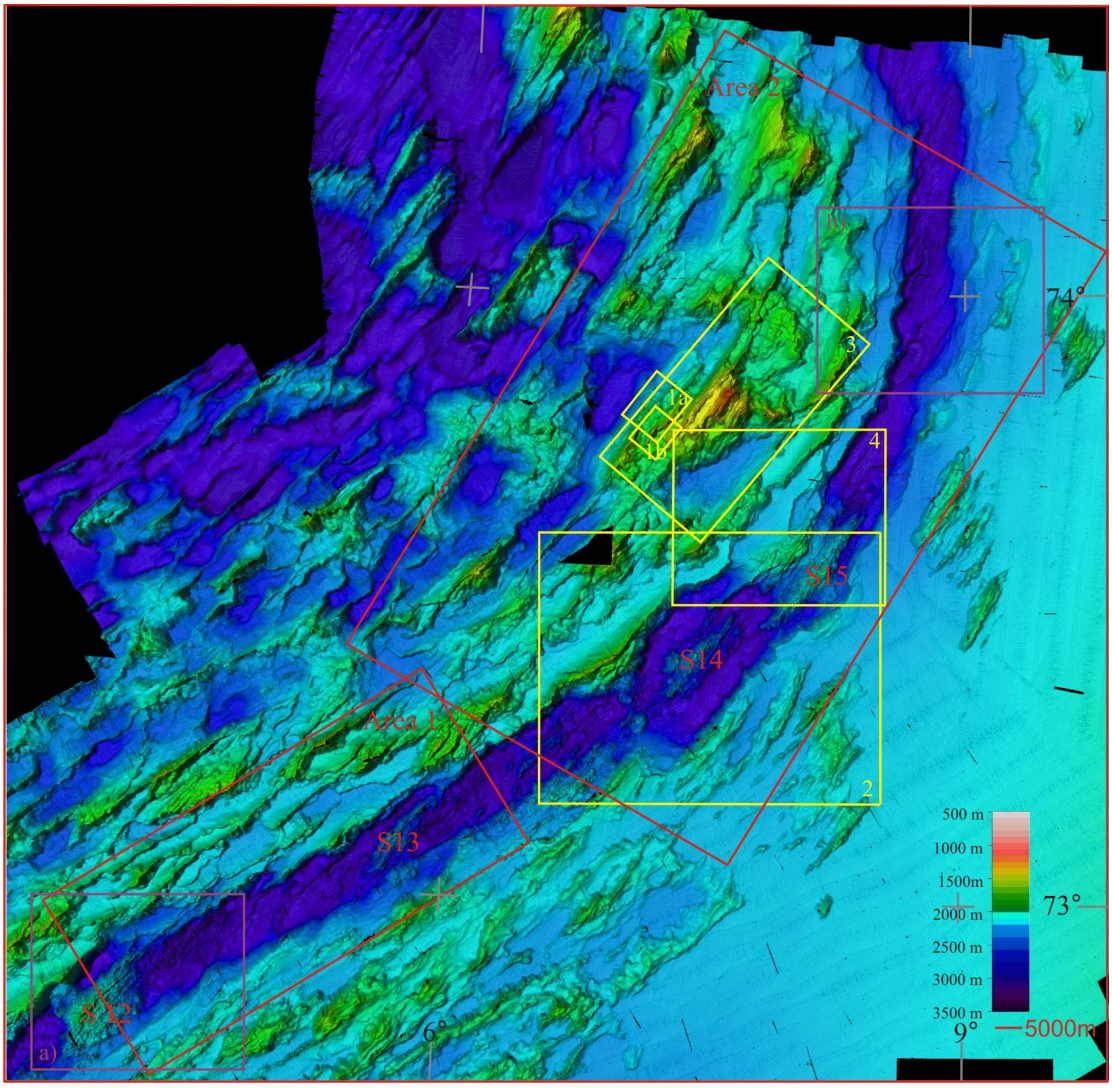

Figure 4.1: Shaded color-coded bathymetric map of the study area. Depth scale is indicated by the color bar. Red boxes show the subdivided areas 1 (southwest) and 2 (northeast). S12 – S15 indicate AVRs defined by Hellevang & Pedersen (2003) as second-order segment centers. Purple boxes labeled a) and b) are the location of the captures presented in figure 4.2. Yellow numbered boxes are areas described in more detail en Section 4.4.

4.2. Axial valley

The axial valley is characterized by both oblique and parallel highs situated within the basins and spaced 28 – 64 km apart. Segment 12 delimits the study area (Figure 4.1) of the ridge to the southwest and is approximately 19 km wide. The center of the segment is defined by a large AVR (amongst the largest on the entire Mohns Ridge) rising 1200 m above the valley floor. The AVR is oblique to the rift valley trend by an angle of 21º with the northern tip curving clockwise towards the valley wall with a slightly sigmoidal shape (Figure 4.2a). Just east-northeast of the AVR is an over 3500 m deep tectonic-dominated basin (Figure 4.2b). Segment 13 is approximately 16 km wide and shows a well defined sigmoid AVR (Figure 4.1). It is 19º oblique at the center of the segment and rises 900 m above the valley floor.

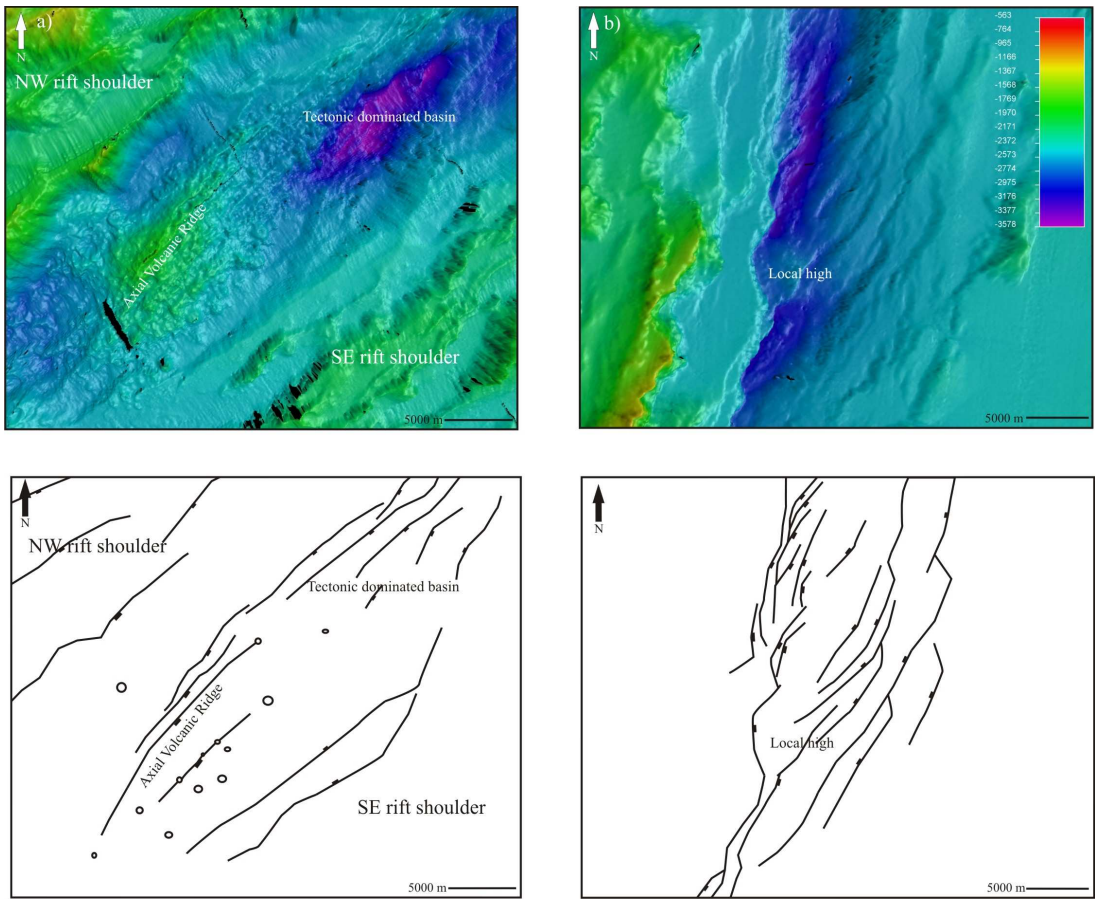

Figure 4.2: Shaded color-coded bathymetric map, depth scale is indicated by color bar in figure b). For position of capture see purple boxes in figure 4.1. The illustration beneath each bathymetric map is an interpretation of the intra-rift faults as well as border faults, volcanoes and feature discussed in the text. Faults are marked by black lines with tick marks indicating the downthrown side. Circular volcanoes are marked with circles. The AVR present in figure a) corresponds to ridge segment center no. 12 as defined by Hellevang and Pedersen (2003).

Segment 14 and 15 show well-defined AVRs oriented parallel to the rift valley and rising 600 and 800 m above the valley floor (Figure 4.1). The segments are approximately 22 km and 12 km wide. The AVR for segment 15 is situated in the Mohns-Knipovich Bend and the southern tip curves towards segment 14 (Figure 4.1). Both segment 13 and 15 are relatively narrow compared with the other segments (Figure 4.1), and the AVRs are not thoroughly faulted in contrast to AVR 12 (Figure 4.2a). This indicates that these ridges are young and thus at an earlier growth stage (Parson et al. 1993).

Deep basins are identified throughout the rift valley with the deepest and most extensive just north-northwest of AVR 12 (Figure 4.2a), east-southeast of AVR 13 and the most southern part of the Knipovich Ridge just north of the bend (Figure 4.2b). They are characterized by faults forming grabens and sparse volcanism. These depths are interpreted as amagmatic (tectonic) dominated basins and thus correspond to higher-order segments (3^{rd} of 4^{th} order) (Macdonald et al. 1988 & 1991; Hellevang & Pedersen, 2003).

The intra-rift faults roughly tend to follow the trend of the AVR. In area 1 they thus exhibit oblique and sigmoid trends and in area 2 a parallel trend (see orientation of AVRs in Figure 4.1). The intra-rift faults are difficult to interpret. This is believed to be because they have not yet developed a fault surface that is easily distinguishable due to the bathymetric resolution. In addition volcanism is believed to have altered the fault surface and topography. Intra-rift faults are therefore not very well represented in the fault maps presented in Section 4.3. An exception to this is the southern Knipovich Ridge where intra-rift faults are more apparent (Figure 4.2b). The reason they are more apparent is believed to be due to lesser volcanism as few volcanoes are identified in the area. In area 1, as well as the southern Knipovich Ridge, the intra-rift faults commonly intersect with the border faults (Figure 4.2b, Figure 4.3 and 4.8).

The southern part of the Knipovich ridge is characterized by hard-linked intra-rift faults in an en echelon pattern (Figure 4.2b & 4.8). Due to the highly oblique character of the ridges, faults on the western border overlap with oppositely dipping

faults on the eastern border, thus forming horst ridges when faults dip away from each other and basins (grabens) when the faults dip towards each other. This can be seen in Figure 4.2b where the “local high” is a feature 400 m above the seafloor just below 74ºN. This feature is interpreted to be a horst block where faults are partly overlapping and dipping away from each other. Grabens are identified both to the north and to the south of the horst structure where en echelon arranged faults dip towards each other (Figure 4.2b). The local high could alternatively correspond to an AVR, although the horst block interpretation is more feasible as no volcanism has been identified adjacent to the height.

The axial valley rift changes orientation along axis trending 59° in the vicinity of segment 12 and 13 to trending 37° at the Mohns-Knipovich Ridge (see Figure 4.5 which includes ridge trend for area 1 and the Mohns-Knipovich Bend in area 2). The southern part of the Knipovich Ridge, in the vicinity of 74°N has a measured trend of 9°. Thus the along axis rotation is 50° anticlockwise for the 240 km ridge comprising the study area (Figure 4.1).

4.3. Western rift flanks

4.3.1. Rift flank area 1

The topography seen in the shaded bathymetric map shows that the northwestern rift flank in area 1 consists of up to 27 km long lineaments (Figure 4.3). The lineaments are interpreted as faults (fault map Figure 4.3). They curve slightly forming overlap structures. The fault geometry directly northeast of the AVR 12 (corresponding to S 12 in Figure 4.1) is anastomosed. The faults commonly show smaller jogs or curves in the fault trace, which implies hard-linked relay structures. The geometry west of AVR 13 (corresponding to S13 in Figure 4.1) shows parallel fault geometry with major faults soft-linked with respect to one another.

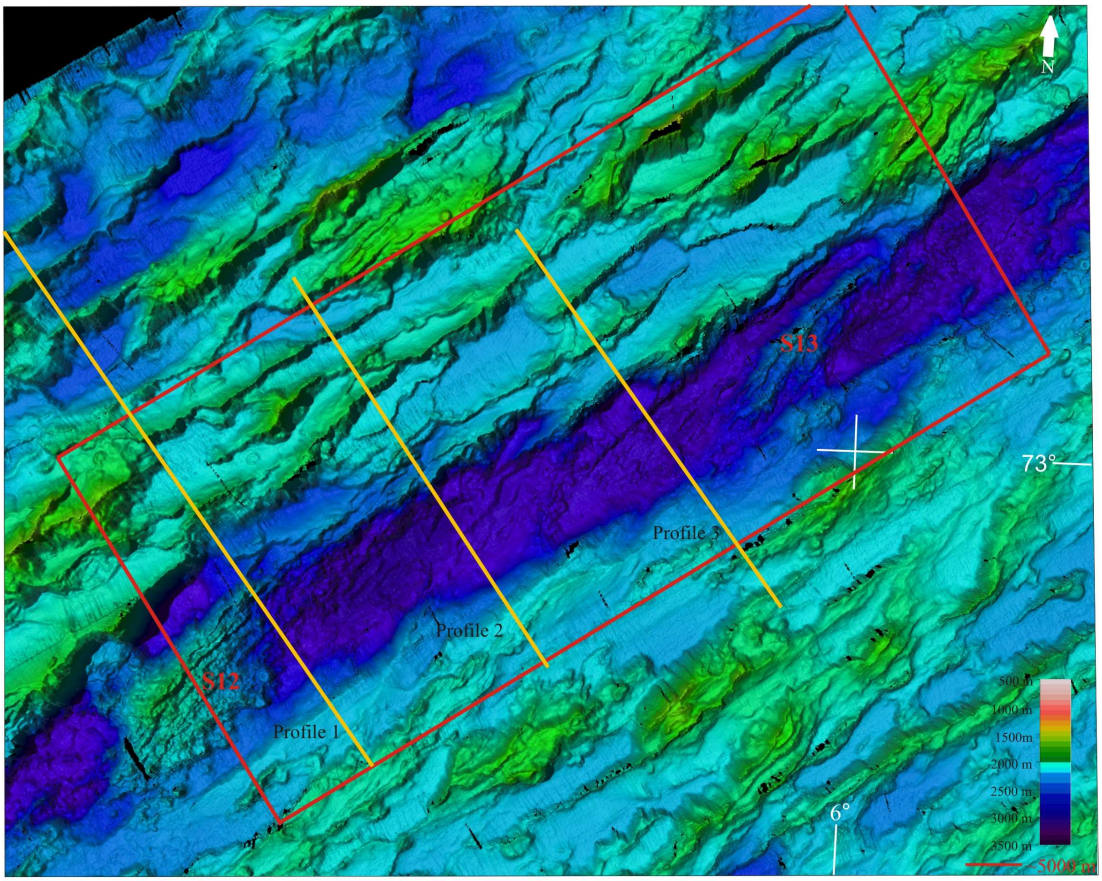
N
S13
73°
Profile 3
Profile 2
S12
Profile 1
500 m
1000 m
1500m
2000 m
2500 m
3000 m
3500 m
6°
~5000 m

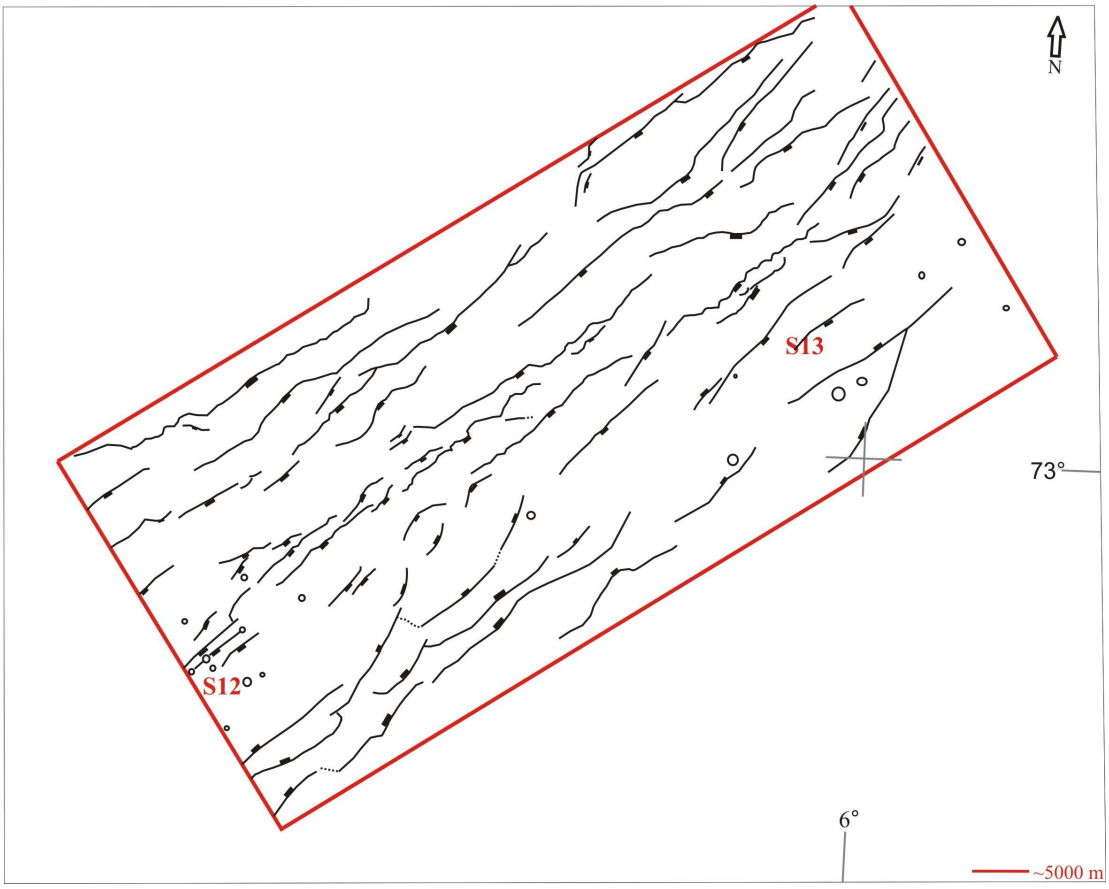
N
S13
73°
S12
6°
~5000 m

Figure 4.3: (previous page) Shaded color-coded detailed bathymetric map covering area 1 (red box). Depth scale is indicated by the color bar. S12 and S13 represent the segment centers. Yellow lines represent the position of the profiles presented in Figure 4.6. The illustration beneath the bathymetry is an interpretation of faults and volcanoes. Faults are marked by black lines with a tick marks indicating the downthrown side. Black lines without ticks represent undifferentiated lineaments. Circular volcanoes are marked with circles.

Displacement maximums are plotted against fault length in a logarithmic diagram (Figure 4.4) showing a range from 300 to over 1000 m for the faults throw maximum and 3500-27000 m for the fault lengths. The data defines a linear trend. Hard-linked faults plot closer to γ =0.01 whereas the single faults plot towards γ =0.1. The orientation of the faults in area 1 is illustrated in the stereographic projection in Figure 4.5. The mean trend for the faults on the west shoulder is 051/47, and for the east shoulder 230/47, thus, implying symmetry in fault orientation across the axis. The axial valley orientation, 059, is plotted in the stereographic projection showing an 8° angle between axial valley orientation and fault orientation.

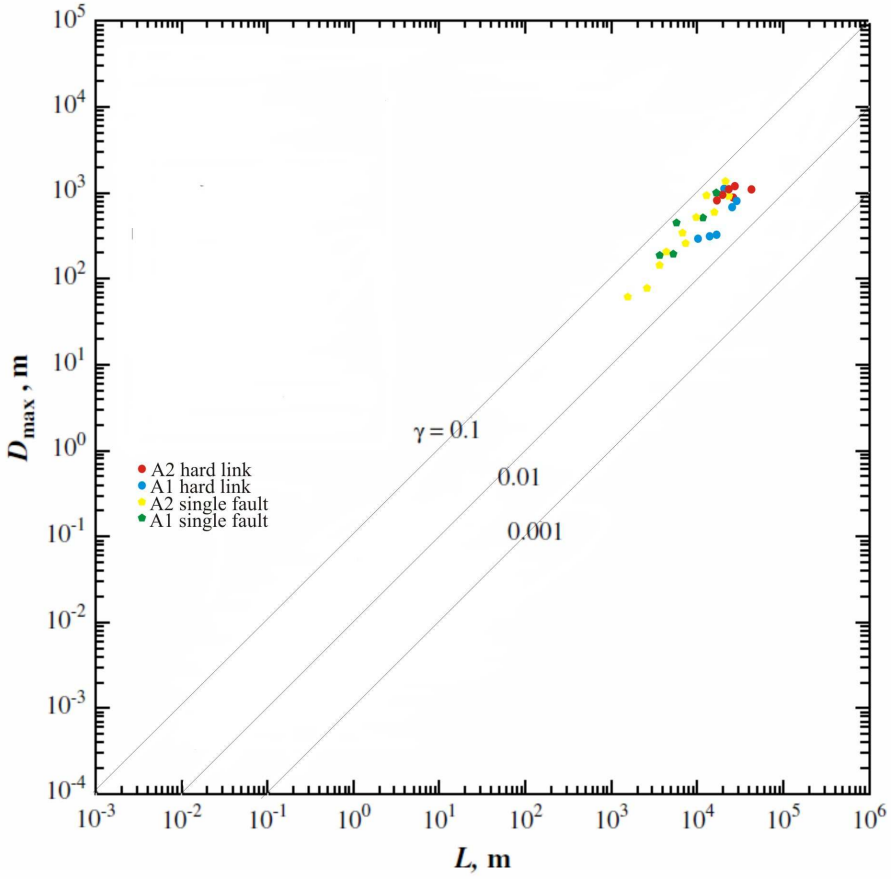

Figure 4.4: Maximum throw plotted against length for both single and hard-linked faults. γ=D/L. Scale is logarithmic and in meters.

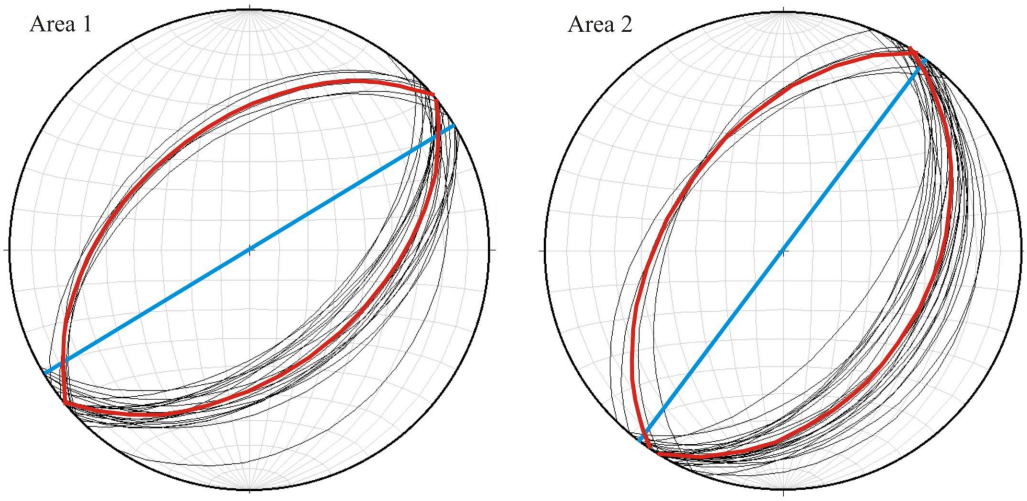

Figure 4.5: Stereographic projections for the two areas. Red lines represent best fit and blue lines illustrate the ridge orientation. All faults measured are done on the rift shoulders. The faults are all synthetic and therefore dip towards the rift valley.

The profiles 1 through 3 (Figure 4.6) are spaced approximately 20 km apart (profile location in Figure 4.3). The faults northwest in vicinity of the axial valley exhibit steep dips, ranging 45° in profile 1, just north of the AVR tip, to 55° and 57° in profile 2 and 3. As the distance away from the axis increases the fault dips tend to decrease slightly to an average of ~44°. Thus a slight decrease in fault dip away from the axis is identified. The only low angle fault (23°) identified on the western flank is a poor fault surface identified between two steep faults (49° and 53°) in profile 2. The low dip reading is thought to be due to erosion and sedimentation as the fault is barley visible in the bathymetry. Where measurements have been possible on the southeastern flank they range between 38° and 48° and the general morphology gives the impression of down faulted terraces (Figure 4.3 and profile 3 and to some extent 1 in Figure 4.6). Dip measurements of intra-rift faults are spares due to their misleading low dip readings (which are not noted on the fault profiles). The low dip reading can be explained by either extremely low angle, 10°-20°, faults generating in the rift valley, or perhaps more feasible, they represent a cluster of faults altering the dip reading and may be further degraded by sedimentation and volcanism. The profiles do not show great amounts of disturbances and are, instead, rather systematic with respect to faults spacing and throw.

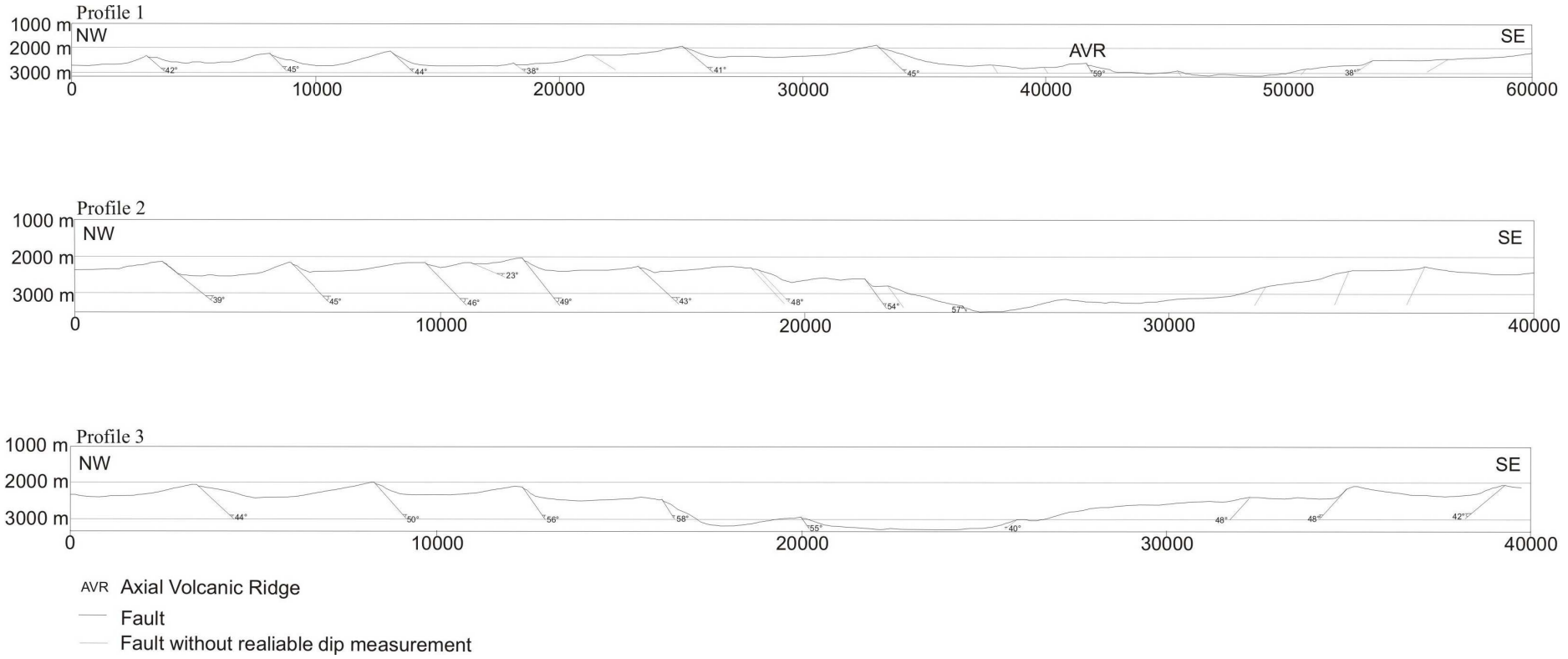

Figure 4.6: Profiles 1-3 with no vertical exaggeration. Horizontal and vertical axes are in meters. Fault dips are noted and the fault trace is interpolated downwards.

4.3.2. Rift flank area 2

The topographic expression present in area 2 (Figure 4.7) differs from area 1. The most apparent difference is domed structures (Section 4.4.3 and 4.4.4) and local basins. In map view, the faults (Figure 4.8) show linear, wavy and curved geometry. Smaller jogs on larger faults often correspond to relay ramps. A distinct morphology characteristic is present. This consists of two parallel faults curving slightly towards each other on either side, culminating into one or several faults characterized by a rugged terrain (Section 4.4.4).

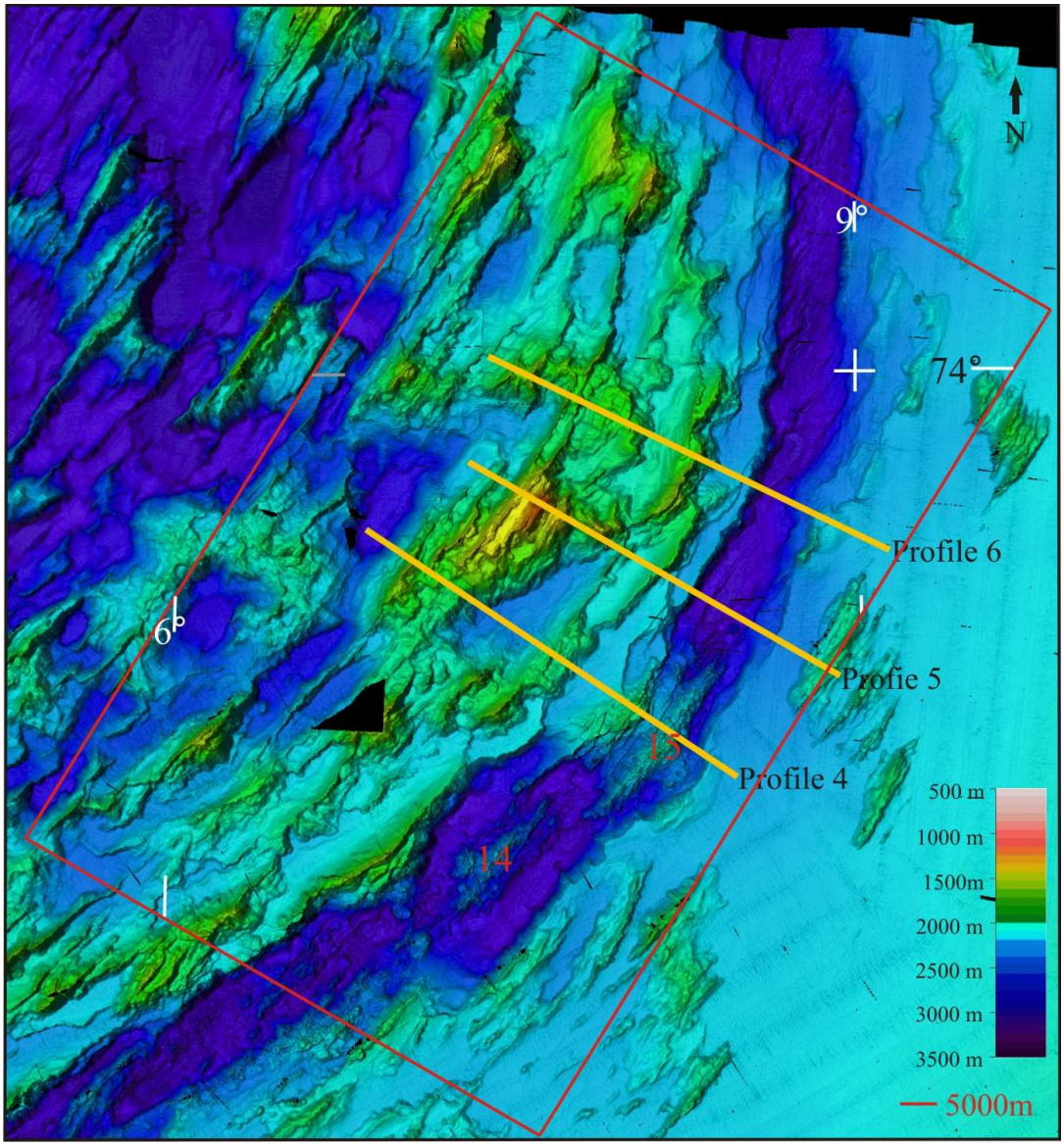

Figure 4.7: Shaded color-coded detailed bathymetric map covering area 2 (red box). Depth scale is indicated by the color bar. S14 and S15 represent the segment centers. Yellow lines represent the position of the profiles presented in Figure 4.9.

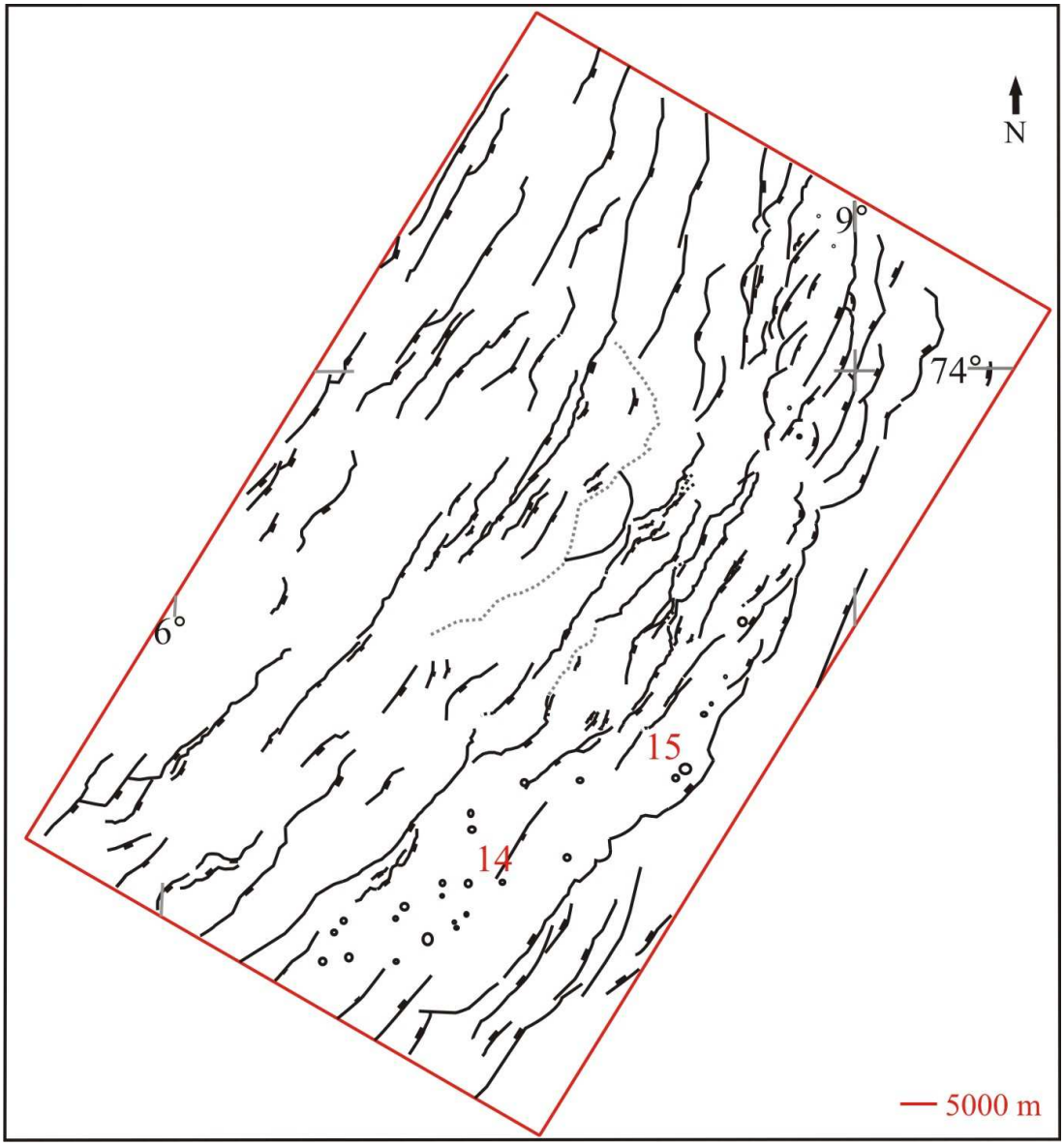

Figure 4.8: Fault map covering area 2 (same scale and view as Figure 4.7). Faults are marked by black lines with a tickmarks indicating the downthrown side. Black lines without ticks represent undifferentiated lineaments. Circular volcanoes are marked with circles. Stippled gray lines indicate possible core complex extent and are described and interpreted in more detail in Section 4.4.3 and 4.4.4.

Maximum displacement versus length is plotted in the same figure as data from area 1 (Figure 4.4). Maximum displacement ranges between 60 – 1300 m and the fault lengths for these faults range between 1500-40000 m. The faults in relation to the domed structures are not plotted with this dataset. Hard-linked and single faults show a similar linear trend as for area 1. They differ from area 1 in not being as clearly segregated with respect to hard-linked faults plotting closer to γ =0.01 and single faults closer to γ =0.1. Stereographic projection illustrates the orientation of the faults

in area 2, giving a best fit of 032/37 for the west shoulder and 214/50 for the east shoulder (Figure 4.5). Thus the data indicates that the faults on either side of the rift have approximately similar orientation but opposite dip directions. The axial valley, trending 37°N, is thus oriented 4° to the stereographic best fit.

The profiles 4 through 6 (Figure 4.9) are spaced approximately 15 - 20 km apart (profile location in Figure 4.7). WNW towards ESE profile 4 is distinguished by two low angle faults of 26° and 28° followed by ~ 10000 m rugged/corrugated topography showing minor faulting. These low angle faults are rotated showing an outward dipping surface. The topography further ESE dips ~13° from 1500 m depth down to a basin at 2650 m where it intersects the seafloor. After a 6 – 7 km wide basin a dome-shaped structure without a well expressed fault trance is present with a 20° dip (Section 4.4.4). The dome-shaped surface shows similar characteristics, this being a rugged surface, as the rugged/corrugated topography that is present adjacent to the first major fault WNW in the profile. Gabbroic rocks have been recovered when dredging the ESE side of the dome (Figure 4.9). Further along the profile a local high with dips in the range of 38° - 56° is present 3000 m before the AVR. ESE of this local high, the AVR 15 is present, making fault readings difficult. The eastern flank shows a fault dip measurement of 44°.

Profile 5 (Figure 4.9) is distinguished by a 27° dipping fault to the west followed by an elevated outward dipping dome consisting of a 26° dipping fault followed by steeper 34° - 41° faults (see Section 4.4.3). The dome dips 15° to the ESE and rock dredges have recovered serpentinized mantle peridotite (Pedersen et al., 2009) on this dipping surface. Another domed structure is apparent further ESE where dikes have been identified by submersibles (Pedersen et al., 2009). No clear fault surfaces for dip measurements are apparent. ESE towards the axial valley four faults are identified dipping between 38° and 50°. Profile 5 further shows a trend of lower angle faults WSW becoming progressively steeper towards the axial valley. The east flank shows signs of faulting though the only measurable faults dip 36° and 41° to the ESE. The former, representing the border fault and the latter, one of the few exposed fault clusters on the east flank.

Two faults dipping 29° and 36° are present WNW on profile 6 (Figure 4.9) followed by two more faults dipping 34° and 32° and are the WNW boundary of a 12000 m wide slightly domed feature (Section 4.4.3). The domed feature is characterized by rugged topography and corrugations and apparently ends dipping 20°, intersecting the seafloor. It is followed by a fault with over a 1000 m throw. This large fault corresponds to the outer border faults described by Hellevang and Pedersen (2003) and ESE the inner border fault is present dipping 50° towards the rift valley. No reliable dip measurements were identified on the east flank.

The border faults are uneven, although more prominent with larger throw on the northwest side aiding an asymmetry across the valley as seen in the profiles. To the east of segment 15 the topography is less rugged and only a few exposed fault clusters are seen in the bathymetry (Figure 4.7). A striking asymmetric feature of these fault clusters is that they appear to consist of several faults stepping northwest with respect to one another. On a larger scale the clusters show the same pattern stepping northwestwards with respect to each other. This is apparent from the bathymetric map presented in Figure 4.7.

The three profiles produced for area 2 show great variations in topographic expression opposed to area 1. They exhibit domed structures, low angle faults and a clear fault trend with steeper dips close to the axial valley and low angle faults away from the axis. The low angle faults often exhibit steep outward dipping slopes to the WNW where basins are commonly identified. Narrow zones of depressed crust are apparent for the second domed feature in profile 4 as well as for the domed features in profile 5 and 6.

Several features of interest, as mentioned when describing the profiles, will be described and interpreted in more detail in the following sections of this chapter.

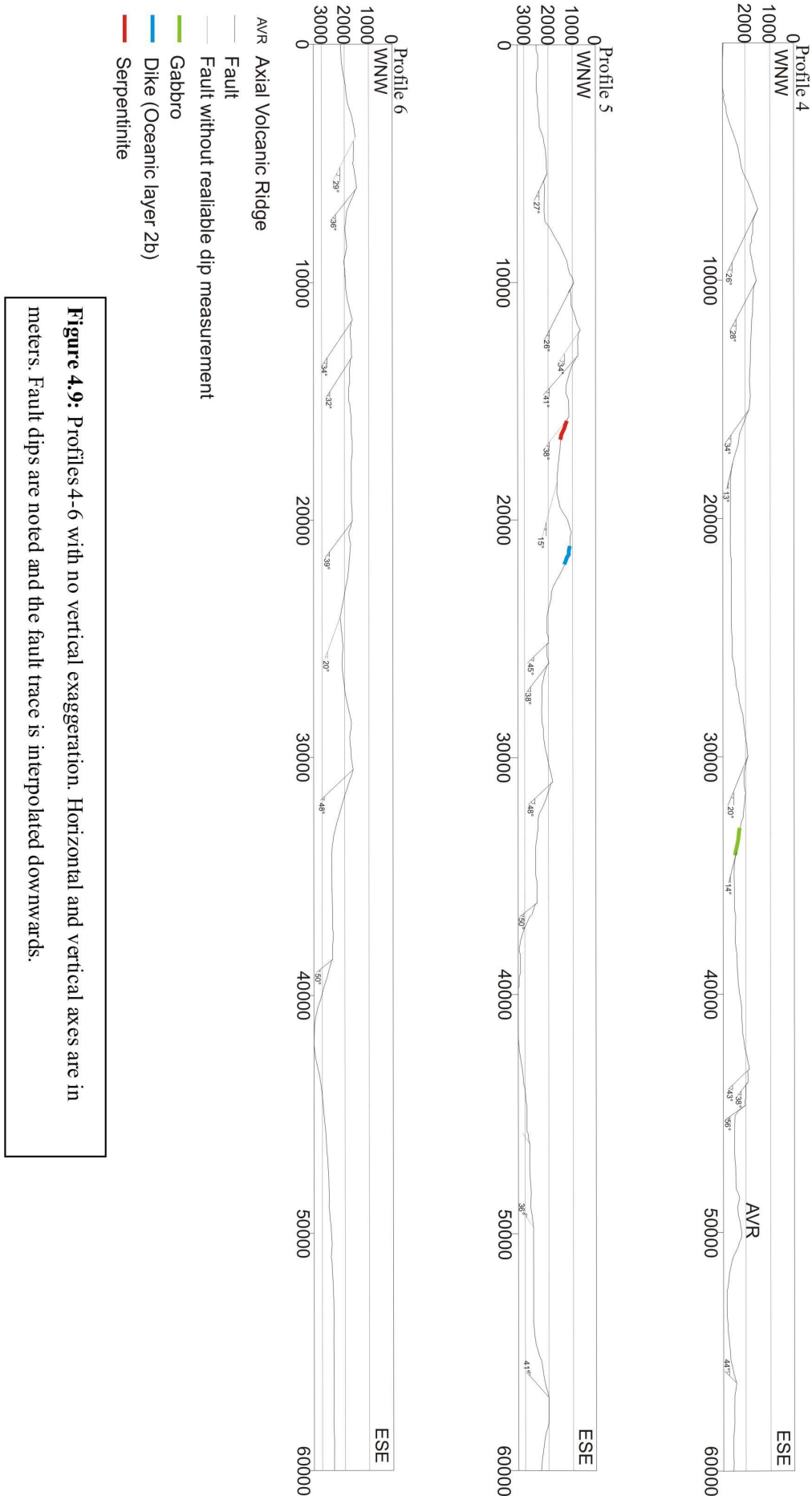

Figure 4.9: Profiles 4-6 with no vertical exaggeration. Horizontal and vertical axes are in meters. Fault dips are noted and the fault trace is interpolated downwards.

4.4. Detailed description

4.4.1. Relay structures – soft- and hard- link

Throughout the study area, there are numerous relay structures both hard-linked and soft-linked, as seen from the fault maps (Figure 4.3 and 4.8). In this section an example of both structures are presented. Figure 4.10a shows a relay ramp ca. 700 m wide bounded by two overlapping southwest-northeast striking normal faults dipping ca. 20°-30° southeast. In map view they do not appear to connect, thus this is classified as a soft-link structure. The southwestern fault has ca. 700 m fault throw which dies out to the northeast, whereas the norhteastern fault has ca. 420 m fault throw which dies out to the southwest. This is seen in the throw-length diagram in Figure 4.10a.

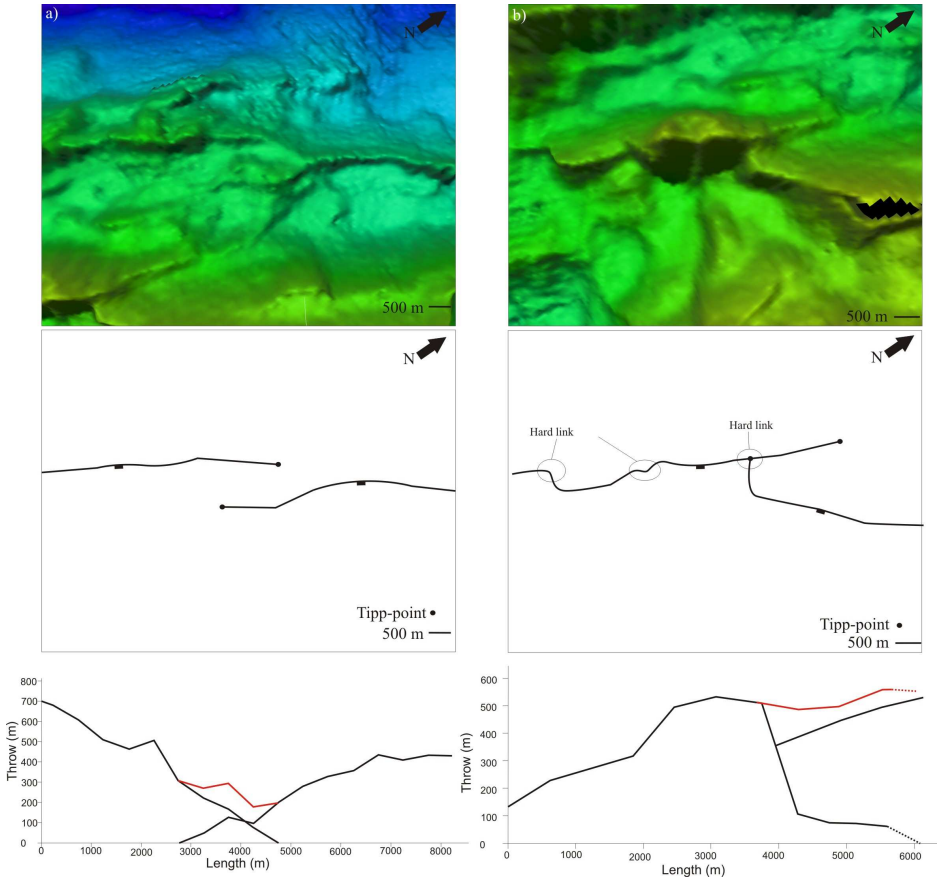

Figure 4.10: Detailed color-coded shaded bathymetric map of a) a soft-link structure and b) a hard-link structure. Depth scale is indicated by the color bar in Figure 4.1. The middle two illustrations are of the faults and tickmarks indicate the downthrown side. Throw length plot is presented and black lines represent the individual faults whereas the red line represents the sum of the black lines. Yellow box numbers 1a and 1b in Figure 4.1 represent the location of a) and b).

Figure 4.10b shows a relay structure consisting of two southwest-northeast striking normal faults dipping ca. 35°- 40° southeast. The southwestern fault apparently consists of several hard-link structures evident by the small jogs in the faults trace (fault map Figure 4.10b). The southwestern fault has a maximum throw of ca. 530 m which dies out extremely rapidly past the breaching point (throw-length diagram Figure 4.10b). The portion of the northeastern fault in the map view slightly decreases its throw and abruptly terminates at ca. 370 m where it merges with the southwestern fault. Thus, this can be interpreted as a hard-link structure where the northeastern hanging wall has propagated towards the southwestern foot wall resulting in a hard-linked fault.

4.4.2. Relay structure on segment scale

Segment 14 is 22 km wide and shows a pronounced right step in the bathymetry (Figure 4.11). The main trend can be inferred from the stereographic projection to be ca. 55°N. The segment is characterized by a well defined AVR oriented parallel to the rift valley walls. The border faults have throws between 1200 m – 1800 m northwest and throws between 800 m – 1150 m southeast. The two axial valley walls are bounded by overlapping normal faults dipping ca. 35° - 58° for the northwestern valley walls and 25° - 39° for the southeastern valley walls. The northwestern wall is hard-linked to segment 15 which is seen from the fault map (Figure 4.11). The northwestern border fault is large and displays splay geometry southward with faults comprised of smaller lengths and throws interfering with the main fault. The southeastern wall is connected in fault plane with segment 15 and is thus hard-linked. Southwards, the fault becomes bent towards the border fault of segment 13. It is unclear from the bathymetry if the fault is fully connected with the border fault in segment 13. There are two faults interpreted dipping north-northeast in this relay structure. Two more lineaments are indicated in the bathymetry further north-northeast and may represent faults or, alternatively, debris flows or slide scars due to their low dips.

The stereographic projection in Figure 4.11 illustrates the fault trends for most faults are parallel with respect to the rift axis (being ca. 55°). The fault bends comprising the relay structures give strike at an angle sub-perpendicular to the mean trend.

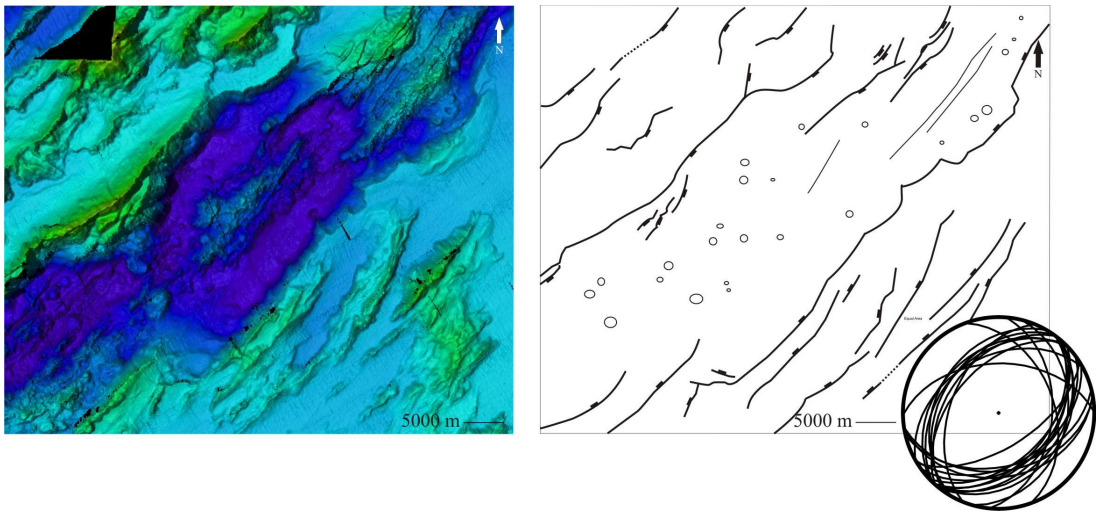

Figure 4.11: Detailed color-coded shaded bathymetric map of segment 14. Depth scale is indicated by color bar in Figure 4.1. A fault map, including a stereographic projection, is presented. For the fault map black lines represent fault whereas the tickmarks indicate the downthrown side. Yellow box number 2 in Figure 4.1 represents the location of the figure.

4.4.3. Core complex

Pedersen et al. (2007) has described the area represented in Figure 4.12 as a core complex based on seafloor dredges recovering lower crustal and upper mantle rocks. The area is approximately 45 km long and 10 km wide and the center of the dome is ca. 25 km away from the spreading axis. A 3000 m deep basin is present to the west-northwest and a 2650 m deep basin is present to the southeast. The maximum height of the complex is at 570 m depth. Viewed in the bathymetry the dome-shaped structure is prolonged and can be divides into two domes with the highest to the southwest and the lowest to the northeast (Figure 4.12). There is a dome-shaped structure to the east-southeast of the southwestern complex where a submersible investigation has identified dikes (Pedersen et al., 2009) (Figure 4.9, profile 5). The geological interpretation (Figure 4.12) illustrates how the fault system consists of relay structures with both examples of hard-link and soft-link structures present. Seen in the geological interpretation for the southwestern dome, is faults stepping towards northeast in two major faults, *a* and *b* (Figure 4.12), before a larger fault, *d*, is present

connecting the southwestern dome with the northeastern dome. Both the *c* and *d* fault towards east-southeast in profile 6 (see correlation in Figure 4.13) cross the northeastern dome and extends to the southeastern dome. Fault *d* is continuous throughout the entire complex length, with exception of the left step southwest, while the *c* fault terminates in a hard-link structure northwest of the maximum height for the southwestern dome. Corrugated surfaces are present on the northeastern dome as well as southwest of the southwestern dome. The corrugations to the southwest of the southwestern dome are adjacent to fault *a* and is interpreted to represent a core complex that has initiated at an earlier stage. Thus the system of northeast stepping faults (*a*, *b* and *d*) and the dome-shaped structure represents a compound core complex and is interpreted to have evolved towards the northeast.

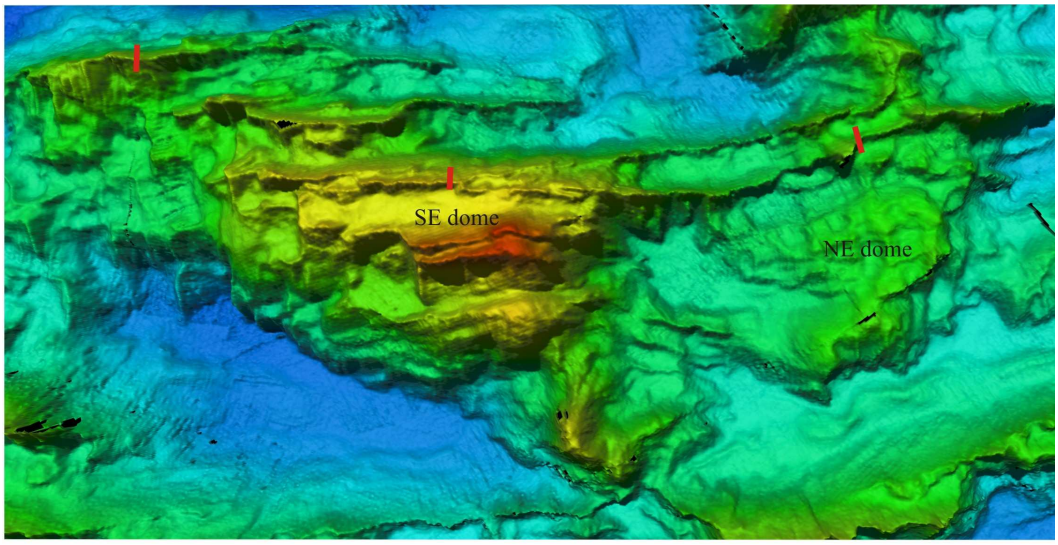

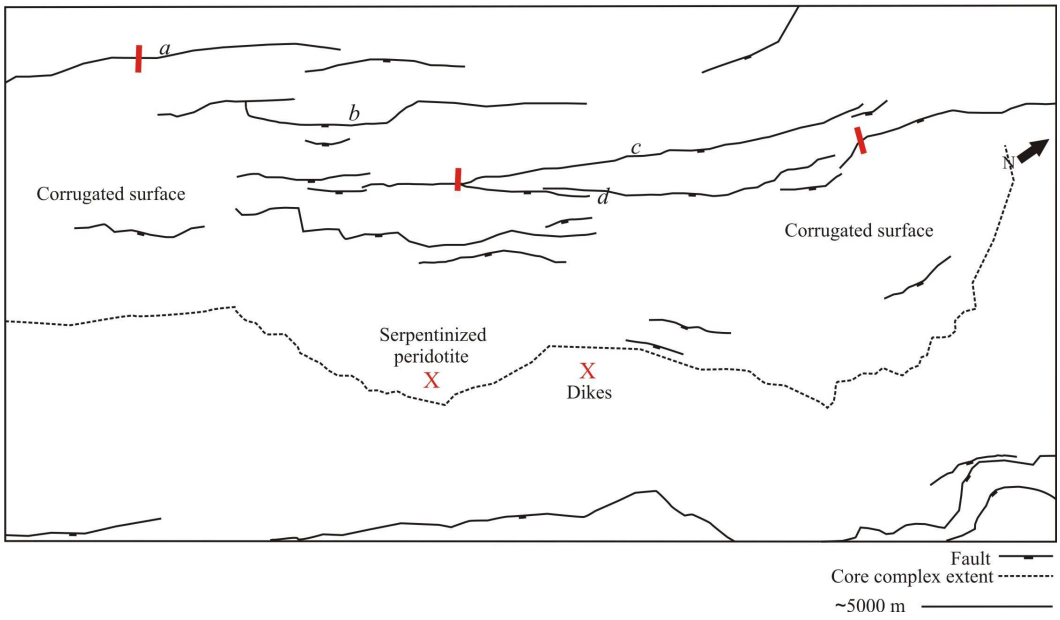

Figure 4.12 (previous page): Close-up shaded color-coded bathymetric map of the compound core complex. Depth scale is indicated by the color bar in Figure 4.1. Yellow box number 3 in Figure 4.1 indicates the figures location. The illustration beneath is a geological interpretation. The faults are marked with black lines and tickmarks indicate the downthrown side. Stippled line indicates the core complex extent towards the ridge axis. Red ticks indicate the detachment fault crest from the detachment surface interpretation in figure 4.13. Letters a through d are faults discussed in the text. Lithology identified by dredges and submersibles are identified by red X.

The profiles crossing the complex (Figure 4.9) show low angle faults WNW. Higher angle faults are present within the domed structure before the dome intersects with the seabed dipping 13° - 20°. An interpretation of the detachment fault surface is presented Figure 4.13 which shows a portion of the profiles presented in Figure 4.9. Fault *a* WNW in profile 4 is interpreted to be the detachment fault. The purple color indicates the fault surface of the detachment fault. The next fault, *b*, in the profile correlates with profile 5 as seen in the fault map (Figure 4.12).The downward 13° dipping surface is interpreted as the tip of the detachment corresponding to the detachment fault extent in map view.

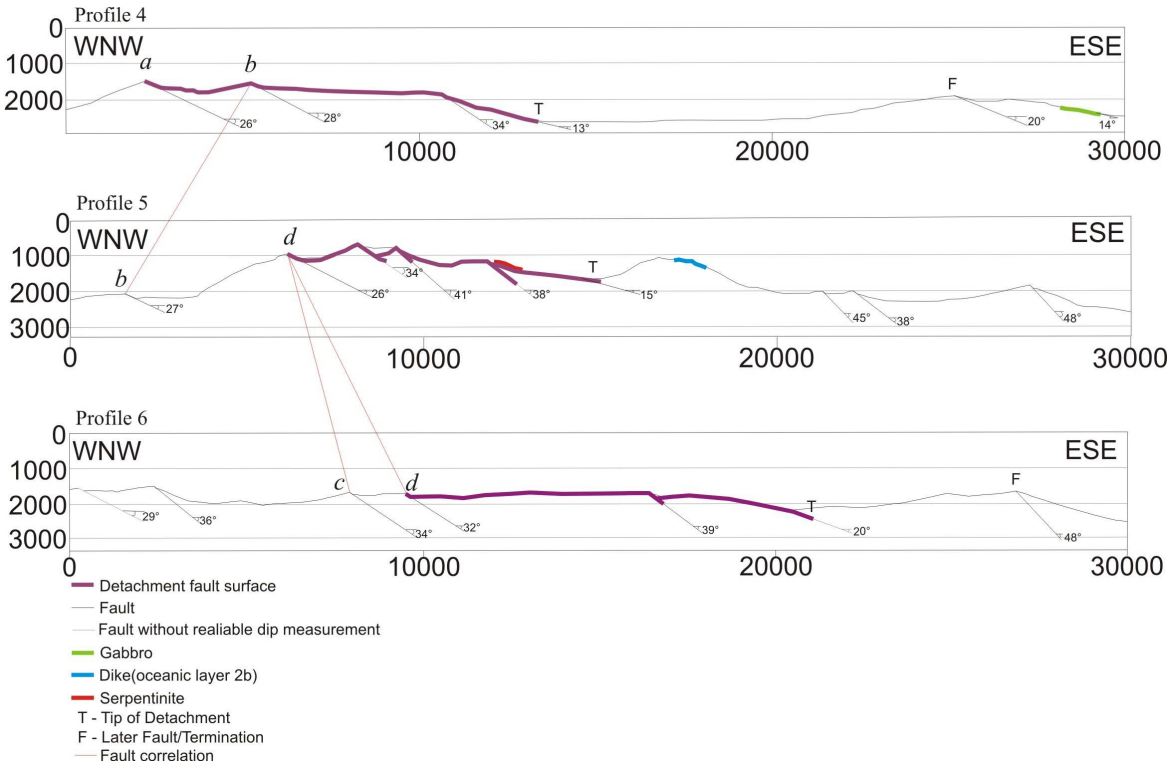

Figure 4.13: Detachment surface interpreted on portions of the profiles 4-6 presented in Figure 4.9. The position of profiles can be seen in Figure 4.7. No vertical exaggeration. Horizontal and vertical

axes are in meters. The detachment fault crest is marked with a red tick in Figure 4.12 and the tip of the detachment (T) corresponds to the dotted line in the geological interpretation presented in Figure 4.12. Letters *a* through *d* are faults discussed in the text.

Fault *b* WNW in profile 5 is the opposite tip of the NE stepping fault present in profile 4 (see fault correlation Figure 4.13). Further ESE the topography domes and the fault dipping 26° is interpreted to represent the detachment fault. The detachment fault is followed by a zone of depressed crust. The following three steeper dipping faults, 34° - 41°, are interpreted to be rafted fault blocks or, alternatively, faults generated on an already exhumed fault surface. The fault surface intersecting the seafloor at approximately 15° is where serpentinite has been recovered. The termination of this dip is interpreted as the tip of the detachment surface corresponding to the detachment fault extent in map view. Another ~900 m high domed feature is present ESE where dikes have been identified by submersibles. The presence of dikes indicates layer 2B/C and therefore represents a higher crustal level than gabbroic/serpentinite rock representing layer 3 (Keary & Vine, 1990). Dips on either side of the dome are hard to constrain exactly but tend to range 25°-50°. This feature is interpreted to represent the hanging wall or alternatively a rafted block produced during exhumation of the core complex. In profile 6 (Figure 4.13) crossing the northeastern dome fault *d* is interpreted as the detachment fault followed by a narrow zone of depressed crust. This fault correlates to the detachment fault for the southwestern dome shown in Figure 4.13. Further ESE the dome is intersected by a higher angle fault (~39°) interpreted to represent a fault intersecting the exhumed detachment surface. The domed structure intersects the seafloor dipping 20°.

All the morphological characteristics common for core complexes (see Section 2.4) are present in the profiles for area 2. In order, towards the rift axis, these characteristics are; a deep basin, an outward sloping ridge, a narrow zone of depressed crust, a slightly domed massif with or without identifiable corrugations.

4.4.4. Features of interest

The area presented in Figure 4.14 shows three distinct morphologies of interest (red boxes in fault map Figure 4.14). The feature represented by red box A in Figure 4.14 is situated directly to the northeast of the AVR in segment 15 and southwest of a 2450 m deep basin. The area peaks at a depth of 1810 m and is characterized by multiple faults dipping towards the axial valley (fault map Figure 4.14). The faults are closely spaced and only one fault, closest to the axis, is exhibiting a large amount of throw. Measured dips range in the order 38° - 56° (profile 4 Figure 4.9). It is striking how the faults on either side of the feature tend to curve in (non-planar fault surface) and form hard-link structures towards the height as seen in the fault map (Figure 4.14). Red box B in Figure 4.14 shows a similar fault pattern. Here two border faults on either side of a local 2300 m high bend inwards. Sub parallel to the border faults is flank faults distinguishing the same characteristics. Thus, there is a mid point of thoroughly faulted rock.

The largest feature (C in Figure 4.14) to the northwest, striking 047, consists of two faults joining together on both sides of an 11 km long and 5 km wide rugged surface (red box number 3, Figure 4.14). Investigations have recovered gabbroic rock from the southeast side of the morphology (profile 4 Figure 4.9). In profile, the structure is domed rising 700 m above a basin situated to the northwest. There is a linear ridge seen in the bathymetry and interpreted as a fault (see Figure 4.14) dipping 20° towards the rift axis (profile 4 Figure 4.9). The slope intersects 14° into a basin situated towards the rift valley where the rugged topography ceases. The rugged topography shows similar characteristics to the surfaces interpreted as fault surfaces in the detachments in Section 4.4.3 although no corrugations are apparent in the bathymetry. There also appear to be smaller faults within the structure. The surface is also similar to the fault scarp morphology seen in Figure 3.3 although gullies are not identified.

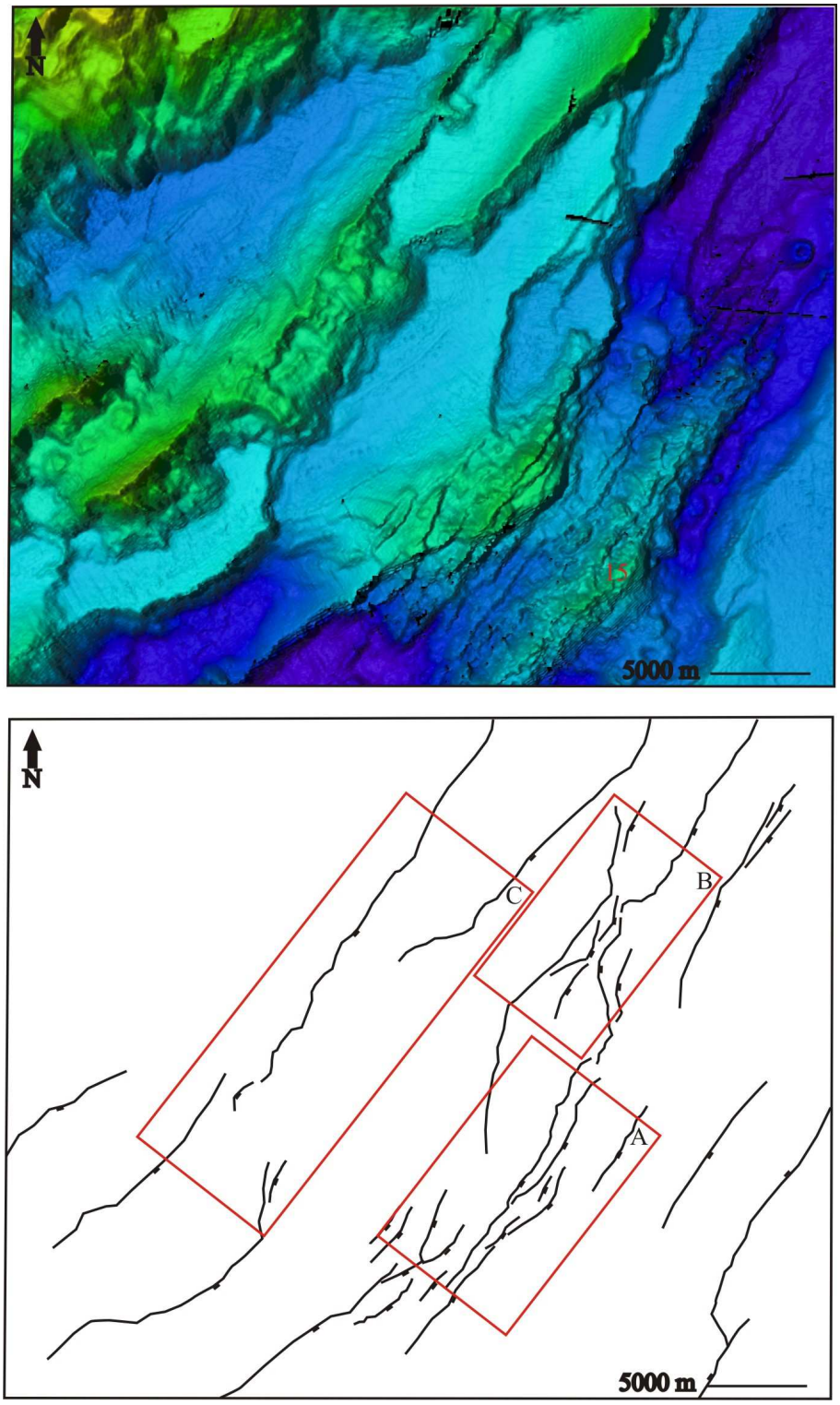

Figure 4.14: Close-up shaded color-coded bathymetric map of features of interest labeled A, B and C. Depth scale is indicated by the color bar in Figure 4.1. Yellow box number 4 in Figure 4.1 indicates the figures location. The illustration beneath is an interpretation of faults and are marked with black lines and tickmarks indicate the downthrown side. Red boxes illustrate the three areas displaying similar fault characteristics. Number 15 in the bathymetric map represents the location of AVR 15.

To the southwest a border fault curves and splits inwards towards the rugged topography (fault map Figure 4.14). Fault throw diminishes from 700 m to 170 m (graph Figure 4.15). Parallel to the border fault a sub parallel fault apparently overlaps with the fault interpreted within the rugged topography showing throw maximum of 1070 m diminishing to 650 m towards the rugged surface (fault map Figure 4.14 and graph Figure 4.15). The fault interpreted in the rugged topography can be traced further NE as seen in the fault map (Figure 4.14). Further northeast past the rugged topography the fault shows characteristics of a normal fault (no prolonged slip) showing dip readings increasing up to 45°. From the throw length diagram (Figure 4.15) it is seen that the fault throw slightly increases from 300 m for the remaining fault segment. Towards the rift valley sub parallel to this fault a normal fault is present. This fault curves strongly towards the rugged topography southwest forming a relay structure. The fault forming the relay structure has a throw of 135 m whereas the remaining fault has throw of approximately 400 m. It can be tempting to interpret a fault between the two southeast faults curving towards the rugged topography and argue that this fault has been buried. But if one interpolates the faults to the southeast they cease. The fault interpreted within the rugged topography has been plotted in the same graph in Figure 4.15 using the scheme illustrated in Figure 3.2 showing fault throws between 600 – 800 m. In profile (Figure 4.9) it is apparent that the amount of debris the rugged topography would represent does not correspond to the amount of eroded material expected. Thus if the rugged topography corresponds to debris it cannot be a result of just one normal fault.

The presence of gabbroic rock indicates a great amount of displacement. Klingelhofer et al. (2000a &b) interpreted the crust at the central Mohns Ridge to be 4.0 ± 0.5 km with variations occurring in the lower crustal layer 3 which is the layer consisting of gabbroic rock. The crustal layer 2 shows an average of 2 ± 0.5 km. If one assumes the crustal thickness is similar further north to the area of interest in this thesis there is two possible mechanisms which may lead to exposure of gabbroic rock on the seabed. The first is a gravity collapse where one large fault, not exhuming upper mantle rocks, collapses by an intersecting fault leading to exhuming mantel rock. This process is illustrated in Figure 4.16.

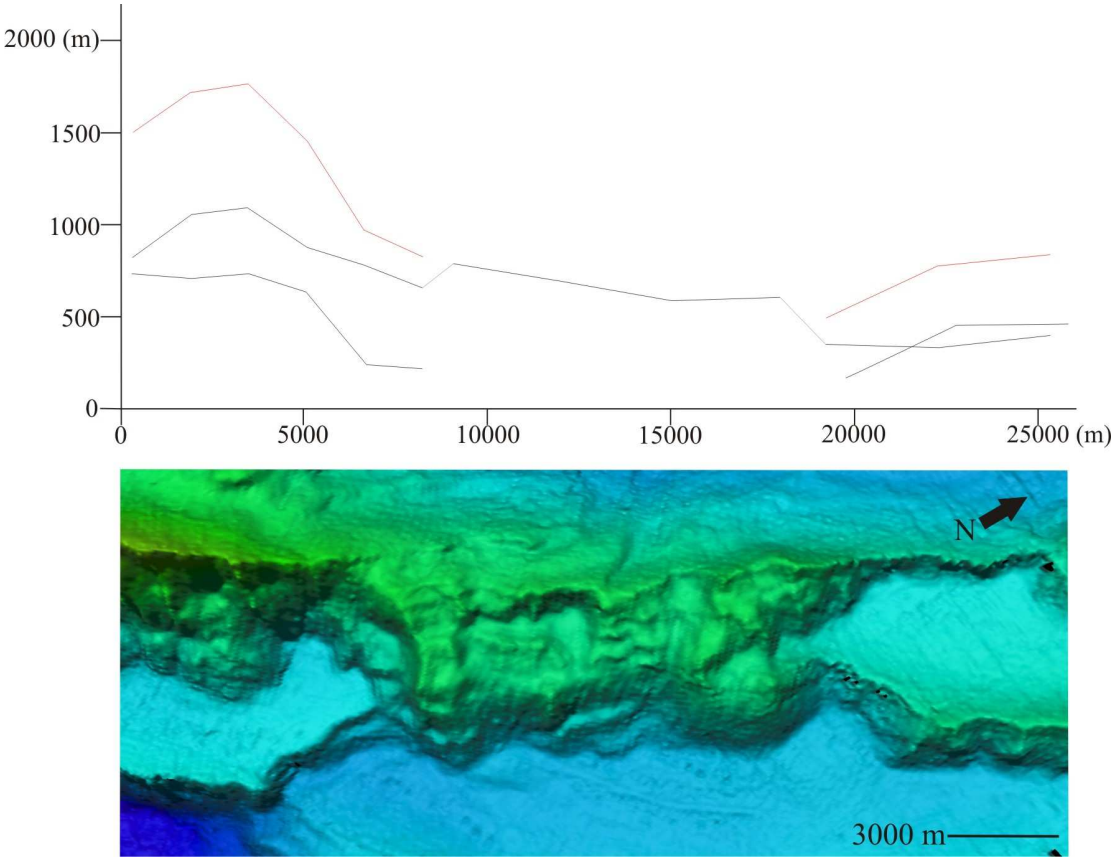

Figure 4.15: Throw – length profile. Black lines represent throw for individual faults whereas red for the sum of overlapping individual faults. The central single fault is interpreted after the scheme illustrated in Figure 3.2. The stippled lines show which individual fault on either side of the rugged topography overlaps with the adjacent fault. Close-up shaded color-coded bathymetric map of Feature C. Depth scale is indicated by the color bar in Figure 4.1. The snapshot corresponds to the red box to the NW in Figure 4.14.

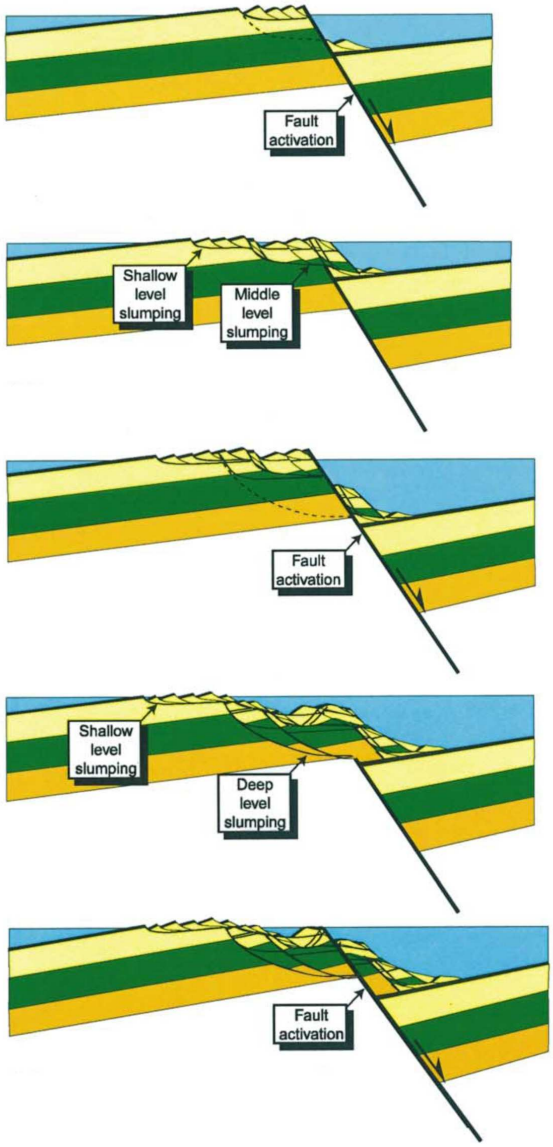

Figure 4.16: Schematic figure of how deeper seated rocks can be exposed by faulting and collapsing. In the figure slumping is the cause of exposure though the slumps are related to faulting and earthquakes. If the green layer in figure corresponds to crustal layer 3 (gabbro) we would se it locally exposed on the seafloor surface. Modified from Hesthammer & Fossen (1999).

The second alternative is that this structure represents a core complex that terminated at an earlier stage before evolving to the extent of the core complex compound described in Section 4.4.3. In profile the dome-shaped rugged structure displays many of the characteristics of core complexes. A fault trace dipping 20° has been noted followed by a depressed zone. Adjacent to the depressed zone is a rugged mounded topography towards the axial valley, extending for approximately 4000-5000 m. This is the amount of faulting needed to exhibit domed fault massifs (Buck, 1988). Other

factors supporting this alternative is a basin situated behind the detachment fault crest (Tucholke et al., 1998; Smith et al. 2006) as well as that the structure is intersecting the seafloor at a low angle of 14°. For this alternative the intersection corresponds to the tip of the detachment surface in map view (Figure 4.17). It has already been shown that the area is characterized by a core complex (Section 4.4.3) and this structure could be formed by the same processes terminating at an earlier stage. Figure 4.17 shows an interpretation of the detachment fault surface.

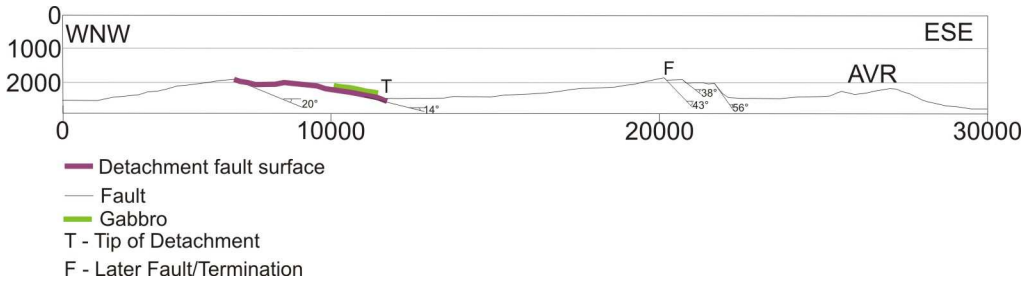

Figure 4.17: Section from profile 4 crossing Feature C (Figure 4.9) with no vertical exaggeration. Horizontal and vertical axis in meters. Fault dips are noted and the fault trace is interpolated downwards. Purple color indicates the detachment fault surface whereas the green color indicates where gabbro has been dredged.

Results from numerical modeling of core complexes show a striking similarity in topographic expression. Figure 4.18 shows a profile over the Feature C with 4 times vertical exaggeration compared to the topography results from the numerical model by Lavier et al. (1999) (position of profile seen in Figure 4.7). It is important to point out that the horizontal scale of the two topographic profiles differs dramatically. Note how the morphological characteristics, outward facing slope, fault break-away/fault crest and domed surface, are strikingly similar. The core complex (Feature C) is present off-axis and is interpreted to be extinct and therefore sediments may alter the topography, especially filling in the zone where the dipping surface intersects the seafloor.

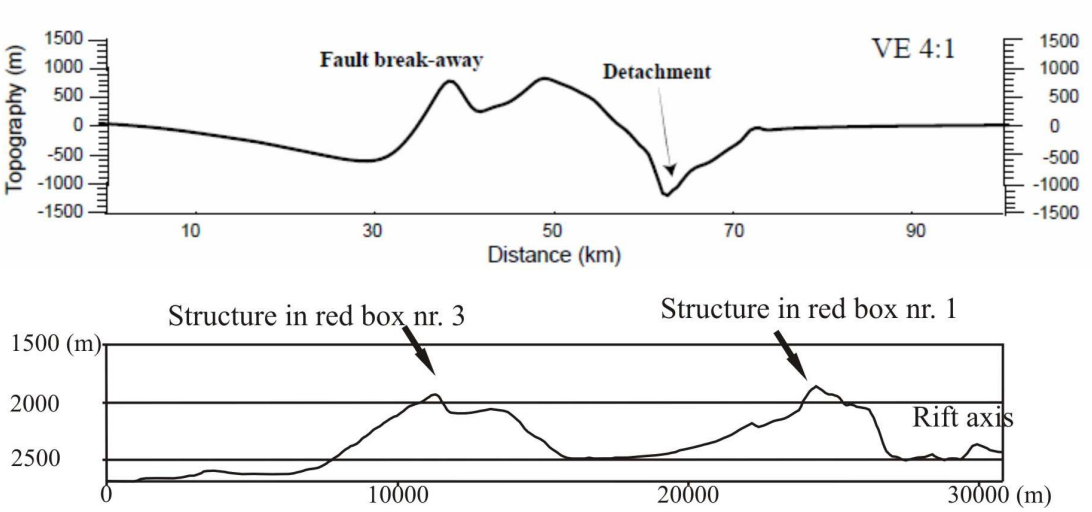

Figure 4.18: Modeled (numerical) topography for a detachment fault (modified from Lavier et al., 1999). Underneath is a section of profile 4 crossing the Feature C. The position of the profile is indicated in Figure 4.7. The topographic exaggeration is 4 times for both topographic profiles in the figure.

5. DISCUSSION

There are several interesting observations presented in the result chapter. This section discusses the data described in the result chapter as well as comparing features with other known field examples. The main themes that will be discussed are:

- Fault population and formation
- Reason for different geologic expression in area 1 and 2
- Fault evolution model for area 1 and 2
- Evolution of Feature C
- Lateral termination of core complexes
- Are several stages of core complex evolution present?

5.1. Fault population and formation

The data plotted in Figure 4.4 shows a general trend where large systems of linked faults display a throw-length relationship tending towards $\gamma = 0.01$ and single faults displaying a throw-length relationship tending towards $\gamma = 0.1$. The hard-link faults tend to plot at higher throw and length values as seen from this figure, although, as mentioned the faults for area 2 are to a lesser degree segregated. The reason we get this trend is illustrated by Jackson's et al. (2002) schematic illustration of fault growth (Figure 5.1) and how this affects the measurements in a logarithmic plot. Displacement/throw for single faults can be expressed by the equation $D=cL^n$ (c is equivalent to γ). As illustrated in Figure 5.1, single faults follow a linear trend. When overlapping the sum of the fault displacement/throw results in deviation from the linear trend as it steps to the right indicating larger length in comparison to displacement. After the fault segments have linked up displacement readjusts, resulting in the displacement-length relationship moving upwards towards the initial linear trend. Thus in a logarithmic plot one expects to see a segregation of single and

linked faults where the linked faults exhibit a higher length/displacement ratio than single faults.

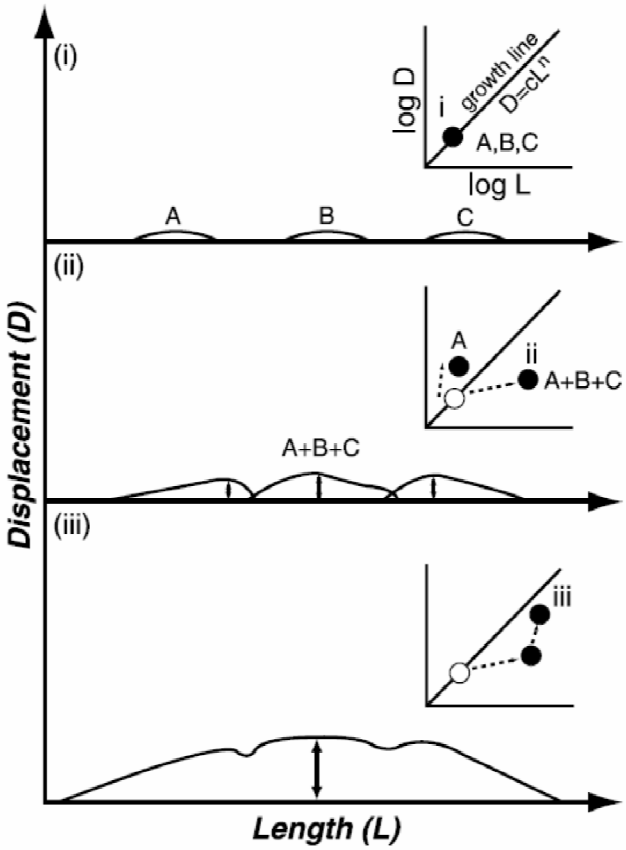

Figure 5.1: Maximum displacement, plotted against fault length for three stages of fault evolution. i) single faults, ii) overlapping faults, iii) post linkage displacement redistribution. Modified from Jackson et al. (2002).

Figure 5.2 shows the data from the Mohns Ridge plotted together with data from different locations consisting of measurements of faults at different scales and includes the three end members of faults; strike-slip, normal and thrust. The majority of faults in this dataset plot between $\gamma = 0.1$ and $\gamma = 0.01$. The main exception is the normal faults in the porous Navajo Sandstone (Utah), which plot between $\gamma = 0.01$ and $\gamma = 0.001$. It is evident from Figure 5.2 that many hard-link data plot lower displacement values than those of single faults, and this is consistent with the model shown in the previous figure (Figure 5.1). It also shows that the Dmax-L relation of at least this mid-ocean ridge conforms with Dmax-L data from continental rift settings and other fault populations in spite of differences in crustal thickness and rheology.

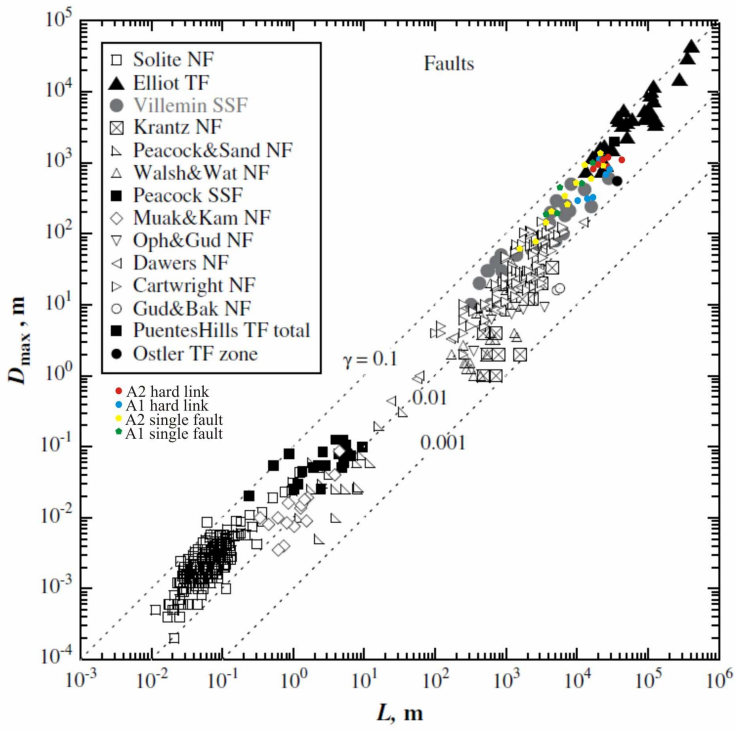

Figure 5.2: Displacement versus length plot for faults, compilation by Schultz et al. (2008) with Mohns Ridge data added. NF – normal faults; SSF – strike-slip faults; TF – thrust faults.

The sum of the throw-length profiles for the soft-linked relay structures in Figure 4.10a show that fault throw decreases as the fault dies out and that summing the profiles results in a depression where the faults overlap. Thus the sum of the two faults deviate from the C-shapes throw-length profile expected from a single fault (Fossen & Hesthammer, 1997). The soft-linked faults correspond to stage ii) in Figure 5.1. The throw-length diagram in Figure 4.10b exhibits only a slight depression where the faults link together thus displaying a higher degree of evolvement towards a plateau type profile (Fossen & Hesthammer, 1997). This corresponds to stage iii) in Figure 5.1, indicating post-linkage displacement redistribution. The throw-length diagrams can give an indication to the fault development since overlap structures are ephemeral features within developing fault systems and are thus created and destroyed during faulting, being preserved when fault growth stops (Childes et al., 1995).

The throw diagram for the fault to the west in Figure 4.10b shows dramatically different throw patterns on either side of the breaching point. To the northeast the throw decreases dramatically whereas the southwest shows a gentle decrease. This is

interpreted to be a result of hard-link faults which behave as single irregular faults (e.g. Peacock & Parfitt, 2002), thus implying the southwestern side being active longer than the northeastern side of the breaching point. The northeastern side of the breaching point has been locked as the two faults have linked, which has resulted in an asymmetric throw-length profile for that individual fault segment. Further it can be seen from the fault interpretation in Figure 4.10b that the western fault consists of several hard-linked faults. This can help illustrate how faults grow as it is evident that the western fault has initially consisted of several separate faults which have linked together with the surrounding faults forming a larger fault. In the next stage the large fault links together with another fault, thus the scale is increasing in magnitude as extension occurs. Throughout the fault maps presented in Figure 4.3 and 4.8, faults are seen to interlink to different degrees. Larger fault systems, e.g. the border faults, display numerous jagged changes in strike as seen in the fault maps, e.g. for segment 14 in Figure 4.11, indicating numerous fault linking during the border fault evolution.

Figure 5.3 shows two different analogies to segment 14. Figure 5.3a shows a color-coded bathymetric map of the Northern Viking Graben consisting of three segments, I to the south, II in the middle and III to the north. The segments show distinct right steps in proportion to one another. The faults display curved geometry and appear to be linked together by both hard-link and soft-link structures. In between the segments, at the segment ends, the seafloor is elevated. This is consistent with stage ii) in Figure 5.1, thus these relay structures are not as evolved as the relay structures presented in Section 4.4.1. The segment width is approximately 40 km and thus considerably wider than what is typical for the Mohns Ridge. Figure 5.3b is a color-coded bathymetric map of Devils Lane in Canyonlands Utah showing two segment ends linked together. The segment widths are approximately 200 m, thus one magnitude smaller than a typical width for the Mohns Ridge. Two well developed relay ramps are present on either side of the relay structure. The tip point for the north eastern fault is exceptionally well exposed as fault displacement increases northwards along this fault. There is a “fin” between the two segments also seen in Figure 5.3c. The Canyonlands area is faulted along preexisting joints due to lower laying stratigraphic salt which became unstable during exhumation by the Colorado River (e.g. Moore and Schultz, 1999). The North Viking Graben is believed to be formed during the Permian-Triassic phase of extension in the North Sea (Roberts et al. 1995). The rifting

ceased and no seafloor spreading occurred, thus this is an aborted rift. The Mohns Ridge segments are defined by AVRs defining the segment centers.

Although these three segments are a result of different styles of faulting and scale the similarities between the shift of the North Viking Graben, Devils Lane and that of the Mohns Ridge (i.e. segment 14) are striking. The elevated bathymetry at the segment ends in the Northern Viking Graben has been shown to correspond to the redistribution of displacement after a relay structure has formed. The “fin” in Devils lane represents a horst block and it is suggested that this is a structural artifact that resulted as the graben formed and overlapped. The relay structure between segment 13 and 14 correspond to transfer zones trending near parallel to the spreading direction accommodating the transition between second order segments (Dauteuil & Brun 1993 & 1996). Volcanism is interpreted in this transfer zone. The area in the vicinity of the transfer zone is thoroughly faulted compared to the border faults. This implies weakening of the curst. It may imply that the volcanism is a result of the transfer zone which may aid to decompression of upper mantle material as a consequence of a weakened (faulted) crust. Magma may therefore ascend to the seafloor surface due to larger amounts of fractures and faults. The largest interpreted volcanoes are not characterized by calderas and are therefore subject to uncertainty regarding their interpretation. Alternatively the local highs may correspond to tectonic derived horsts similar to the “fin” in Devils Lane (Figure 5.3). In either interpretation the elevation at the segment ends between segment 13 and 14 at the Mohns Ridge correspond to the elevated heights in the non-volcanic Northern Viking Graben and Devils Lane, in spite that they originate at different settings.

The fault interpretation in Figure 4.3 and the stereographic projection (Figure 4.5) show that for the oblique spreading area 1, the border faults are at an angle to the rift valley trend. The intra-rift faults show a similar orientation to the AVRs curving towards the border faults. The southern Knipovich Ridge is characterized by highly oblique spreading that has resulted in an en echelon fault geometry with intra-rift faults strongly curving towards the border faults (Figure 4.2). The Mohns-Knipovich Ridge Bend is experiencing less oblique spreading (Figure 4.5) and a result of this is the intra-rift faults oriented sub-perpendicular to the spreading direction. The fault characteristics for these different areas, showing different degrees of oblique

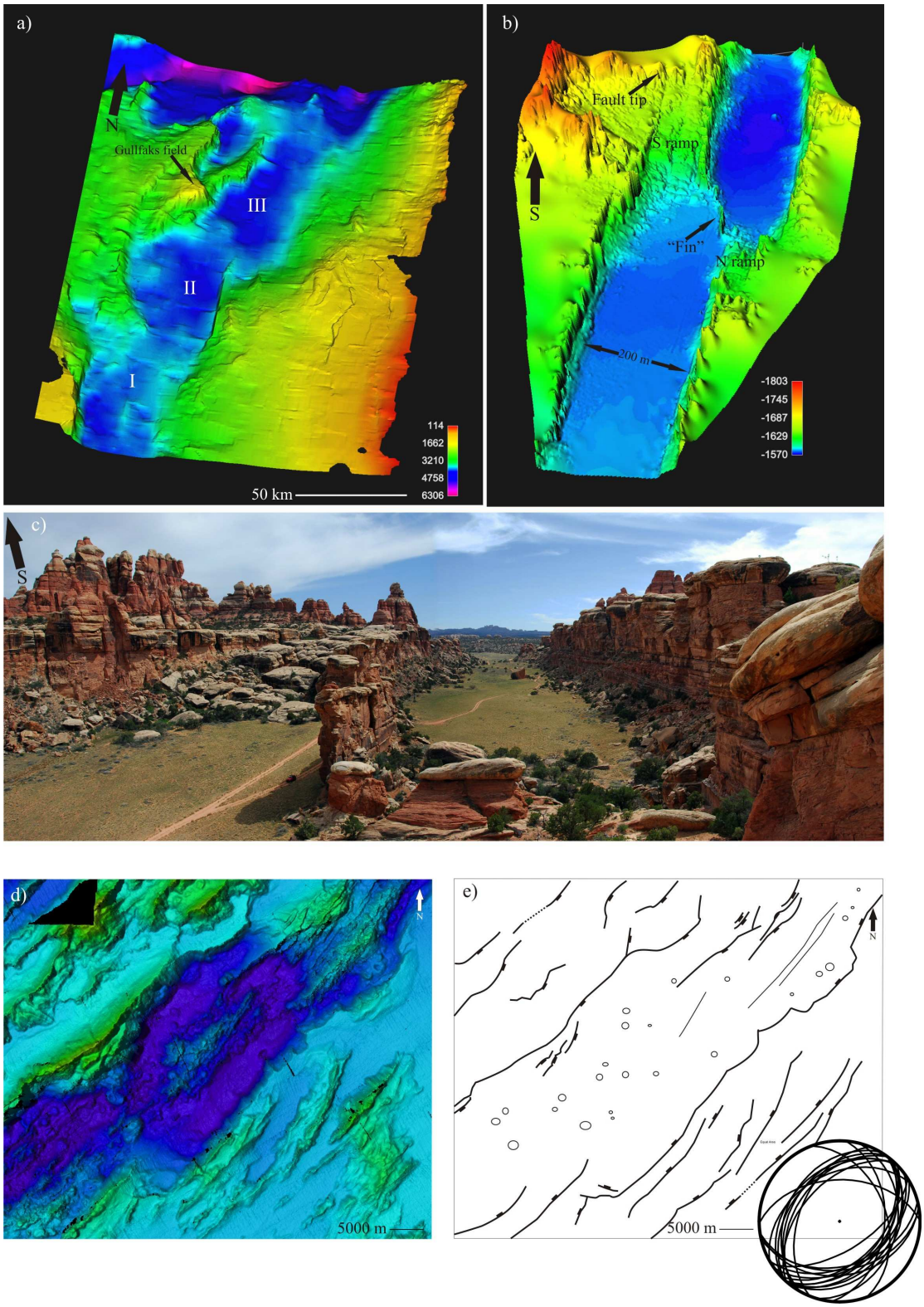

Figure 5.3: Relay analogies to the segments in the Mohns Ridge with emphasis on segment 14.

a) Depth-coded bathymetric map of the Norhern Viking Graben. From Fossen et al., (in review).

b) Depth-coded bathymetric map of Devils Lane in Canyonlands. The "fin" between the segments is the Son of a Bitch Hill also seen in c). From Fossen et al. (in review)

c) Photograph of the Devils Lane looking southward (photograph by H. Fossen)

d) and e) is the same Figure as presented in Figure 4.11 and the positioning is seen in yellow box number 2 in Figure 4.1.

spreading, is consistent with the observations done in analog sandbox rift modeling for orthogonal and oblique spreading rifts (McClay & White, 1995). Here oblique rifting results in en echelon fault geometry with shorter border faults and intra-rift faults forming at a higher angle to the mean ridge trend as obliquity increases.

5.2. Reason for different geological expression in area 1 and 2

It is evident from Section 4.3 that the two areas are distinguished by different topographic expression of the western flanks. This is apparent in bathymetry as well as in profile. The main evolutionary difference between the two areas is that oceanic core complexes have evolved at the Mohns-Knipovich Ridge Bend in area 2. Area 1 is delimited by two AVRs. Sparse volcanism is identified between these AVRs. Instead deep basins corresponding to higher-order magma-starved segmentation have been identified. From the profiles crossing the area (Figure 4.3) it is evident that the fault dips slightly decrease away from the axis. In contrast, area 2 shows severe fault rotation away from the axis and is situated in the vicinity of an AVR with abundant volcanism identified (Figure 4.8 and 4.9). The most southern profile, profile 4, in area 2, crosses the center of AVR 15 whereas the two other profiles cross the axial valley slightly further north. The area comprising the southern Knipovich Ridge is characterized by highly oblique tectonic dominated basins arranged in an en echelon geometry.

Crane et al. (2001) proposes a significant component of compression across the northern Mohns Ridge and southern Knipovich Ridge due to the curved nature of the spreading ridge. Compression often leads to thrusting and uplift. However the interpretations presented in this thesis have not identified any compressional structures. The western flank of the Mohns-Knipovich Ridge Bend is higher elevated than the eastern flank. This is believed to be a result of core complex formation (Pedersen et al., 2007). An additional factor that influences the asymmetry is isostatic response of the lithosphere due to the eastern flank's proximity to the glacial margin (Bruvoll et al., 2009).

The difference in the two areas may be attributed to variations in the thermal state of the lithosphere. Practically no volcanism has been identified for the southern Knipovich Ridge where no AVRs are interpreted. Although volcanism is not identified in the southern Knipovich Ridge from the interpretations presented in Chapter 4, rock dredges have illustrated the presence of volcanic rock within strongly faulted assumed tectonic dominated areas of the Knipovich Ridge (Hellevang & Pedersen, 2005). Sparse volcanism is identified for area 1 which lies between two AVRs. In the vicinity of area 2 in the Mohns-Knipovich Ridge abundant volcanism is identified. There are three areas showing different degrees of volcanism. It is reasonable to believe that the area in the vicinity of the Mohns-Knipovich Ridge Bend is experiencing a higher thermal state of the lithosphere, thus showing a larger degree of characteristics of magmatic extension and accretion.

Klingelhofer et al. (2000b) interpreted the crustal thicknesses at the central Mohns Ridge, 2°W to 4°E, using OBH (ocean bottom hydrophone) data. Here oceanic layer 2a is interpreted to consist of pillow basalt and has an average thickness of 500 m at the axis, decreasing off axis to 200 m, whereas oceanic layer 2b is interpreted to consist of dikes and have an average thickness of 1000 m – 1300 m. Crustal layer 3 consists of gabbro and is interpreted to be 2500 m thick. Recent research by Kandilarov et al. (2008 & 2009) presents two OBS (ocean bottom seismometer) profiles crossing the central Knipovich Ridge, 76° - 77°N. The data presented gives important information of the crustal layer characteristics as the two profiles target an AVR and a tectonic dominated basin respectively. They, therefore, illustrate variations in crustal thicknesses that may be expected along a slow to ultraslow spreading ridge. For the profile crossing a presumed AVR oceanic layer 2 is ~ 3000 m thick at the rift axis and decreases rapidly to ~1000 km some 15 km off-axis. Oceanic layer 3 is ~2000 m at the axis and thickens rapidly off-axis to a maximum of 7000 m 50 km off-axis. Under oceanic layer 3, young mantle is interpreted (Kandilarov et al., 2009). For the tectonic dominated transect (Kandilarov et al., 2008) oceanic layer 2 is interpreted to be in the range of 1000 m – 2000 m within 20 km from the rift axis. Oceanic layer 3 is ~2000 m at the rift axis and increases to ~5000 m 60 km from the rift axis (Figure 5.4).

Data from these publications can be used to produce an along-axis cross section of the study area in combination with bathymetric data and interpretations of morphological features, such as AVRs and higher-order tectonic dominated segments as presented in Chapter 4. A proposed along-axis cross section is presented in Figure 5.4. It is seen that accretion of oceanic crust is more abundant in the vicinity of the AVRs and is expressed by thicker oceanic crust, mainly due to an increase in accretion of oceanic layer 2. This corresponds to Lin et al. (1990) and Cannat et al. (1995) along-axis cross section over segment centers in that magmatic crust is thicker at segment centers (here segment center corresponding to the AVRs 12, 13, 14 & 15) and thinner at the intersection between segments. It can be inferred that magmatic accretion increases the thermal state of the lithosphere, and Figure 5.4 therefore illustrates the thermal differences in the study area.

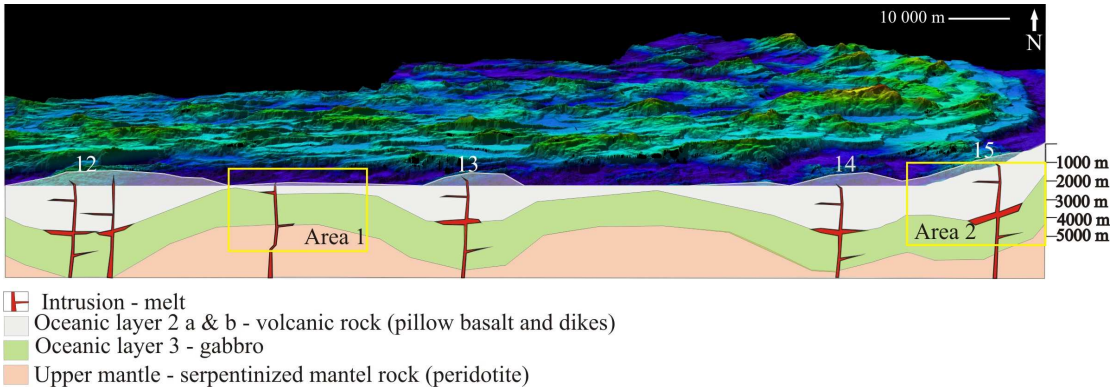

Figure 5.4: Rotated color-coded bathymetric map of the study area. Numbers in the bathymetric map indicate the AVRs. The vertical scale of the bathymetric map is 3 times. Depth is indicated by color bar in Figure 4.1. Vertical scale is sub-seafloor depth. The white line in the bathymetric map indicates the topographic height along the transect. The yellow boxes shows where the models for area 1 and 2 are situated.

5.3. Fault evolution model for area 1 and 2

5.3.1. Data and assumptions

The fault evolution model for areas 1 and 2 is based on the results presented in Chapter 4 (bathymetric and fault maps, topographic cross sections including fault dip

and rocks recovered and observed by dredges and submersibles). Further necessary information of crustal thicknesses is extracted from Klingelhofer et al. (2000b) and Kandilarov et al. (2008 & 2009) (see Section 5.2). The cross sections presented in Figures 5.4, 5.5 & 5.6 are simplified concerning lithologies. A comparison to Dick's et al. (2008) cross section presented for the Kane core complex at the Mid Atlantic Ridge, which is based on a great amount of petrological data, shows a complex interaction between the crustal layers and intrusions (dikes). Information as to how the detachment fault dips into the subsurface is derived from Lavier et al's. (1999) numerical model of large-offset low-angle normal faults. Here plastic strain shows that the active part of the fault dips between 45 - 60°, thus at a much higher angle than the exposed detachment fault surface, which intersects the seafloor with a dip of 13 - 20°. Faults are assumed to initiate at or close to the seafloor. Sparse ephemeral volcanic activity is assumed for area 1.

5.3.2. Evolution model for area 1 & 2

In Chapter 4, the profiles crossing area 1 are described as symmetric with respect to fault spacing and fault throw. The profiles are in between two AVRs and higher-order segmentation in form of tectonic dominated basins has been described. In Figure 5.5 a proposed model for fault evolution is presented, illustrated by cross sections and map views. The latter, to schematically illustrate the orientation faults initiate at as intra-rift faults, and how they propagate with time, evolving to border faults. At time 1, a fault (red fault in Figure 5.5) forms in the axial valley orthogonal to the spreading direction at the least principal stress, thus oblique to the local trend of the rift. Note that the border faults are sub-parallel to the local trend of the rift. This is inferred from the stereographic projection (Figure 4.5) where the faults are at a slight angle to the mean rift trend. The fault further propagates deeper into the crust, at the same time curving towards the border fault (T – 2). This happens as a new fault with opposite polarity initiates (blue fault in Figure 5.5). These two faults dipping towards each other form grabens corresponding to the higher-order tectonic dominated segmentation described in Figure 4.2a. In reality the faults correspond to fault zones or fault clusters, for simplicity indicated by a single fault. At time 3 the initial fault has evolved and is now a border fault with a similar trend as the previous border fault.

This coincides with a new fault initiating within the axial valley. Note how the blue fault with the opposite

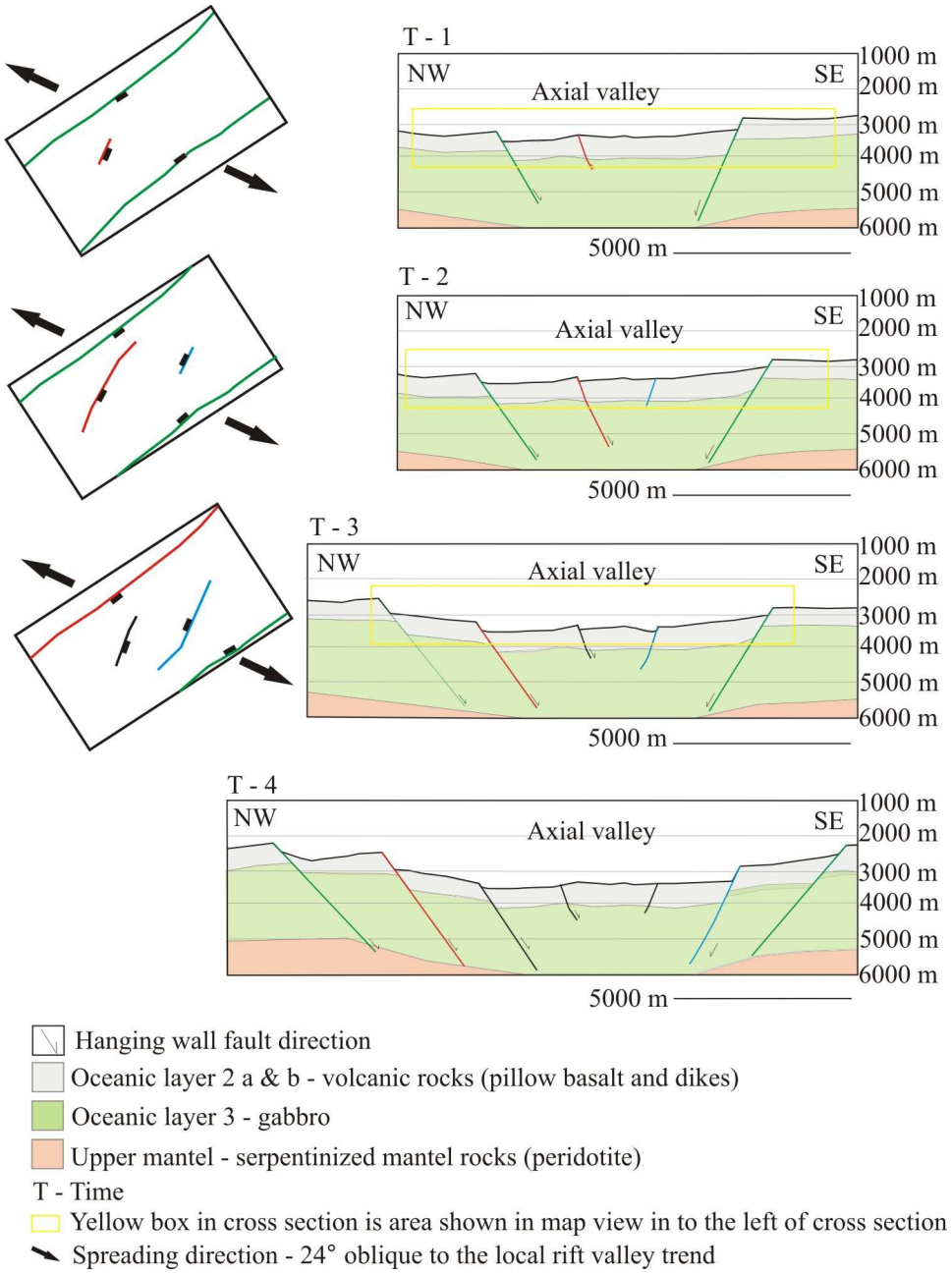

Figure 5.5: Fault evolution model for area 1. This area is situated between two AVRs, see yellow box in Figure 5.4 for positioning. Tectonic dominated accretion with sparse ephemeral magmatism is assumed. The boxes to the left of the cross sections represent the axial valley in map view. The local trend of the rift is parallel to the long side of the bounding boxes. Lines represent faults with black ticks indicating the downthrown side. They illustrate which orientation the faults are inferred to originate at and how they propagate with time. Green faults are initial border faults while red and blue

faults are initial intra-rift faults. The spreading direction is indicated by black arrows, and is 24° oblique (Hellevang & Pedersen, 2003).

polarity is now propagating towards the border fault (T-3 map view, Figure 5.5). It is seen from the final stage of the evolutionary model (not illustrated in map view) that faults have initiated as intra-rift faults with different polarities and have further evolved to become border faults. This coincides as new faults have initiated in the axial valley. This evolutionary model illustrates the symmetry of the area with respect to fault displacement and spacing. Oceanic layer 2 averages at 1000 m, and fault throw results from Chapter 4 range up to 1000 m, thus there may be exposures of gabbroic rock in this area, although this is not shown in the model. Note how the faults gradually rotate as they move away from the axis.

Figure 5.6 illustrates the evolution of the oceanic core complex at the Mohns-Knipovich Ridge Bend in area 2. At time 1, a fault oriented parallel to the axial valley intersects the AVR (red fault Figure 5.6). This eventually results in termination of the border fault to the west-northwest. At time 3, the fault shows characteristics of detachment faulting as the fault has been accommodated by severe displacement. Due to the elevated thermal state of the lithospere resulting from the proximity to the AVR, the fault surface begins to flex. It can be seen that the fault crest is now exhibiting a large amount of rotation, showing equal dips both towards the axis and off axis. At time 4, gabbroic rocks (oceanic layer 3) are exposed at the seafloor due to fault-related exhumation. Here the displacement in map view for the detachment fault is approximately 7 km. As seen from the Figure, the axial valley is increasing in width as more magmatic accretion occurs. At the final stage, time 5, the detachment fault surface is showing an extensive cross section of the upper oceanic lithosphere as oceanic layer 2 and 3 are fully exposed as well as the upper mantel characterized by talc-schist (serpentinzed mantel peridotite). Higher angle faults initiate intersecting the detachment surface. The displacement in map view for the detachment fault is approximately 10 km. The core complex formation is terminated when a new fault is initiated in the rift valley, here intersecting the AVR. This new fault is now the accreting fault and the core complex is extinct. Note how the fault to the east-southeast gradually becomes slightly rotated as it moves away from the spreading center. This is due to both magmatic and fault accretion. The flank east-southeast may

in fact consist of several faults that initiate at different stages, although this is not greatly confined within the data presented in Chapter 4 and therefore not the primary focus of this model.

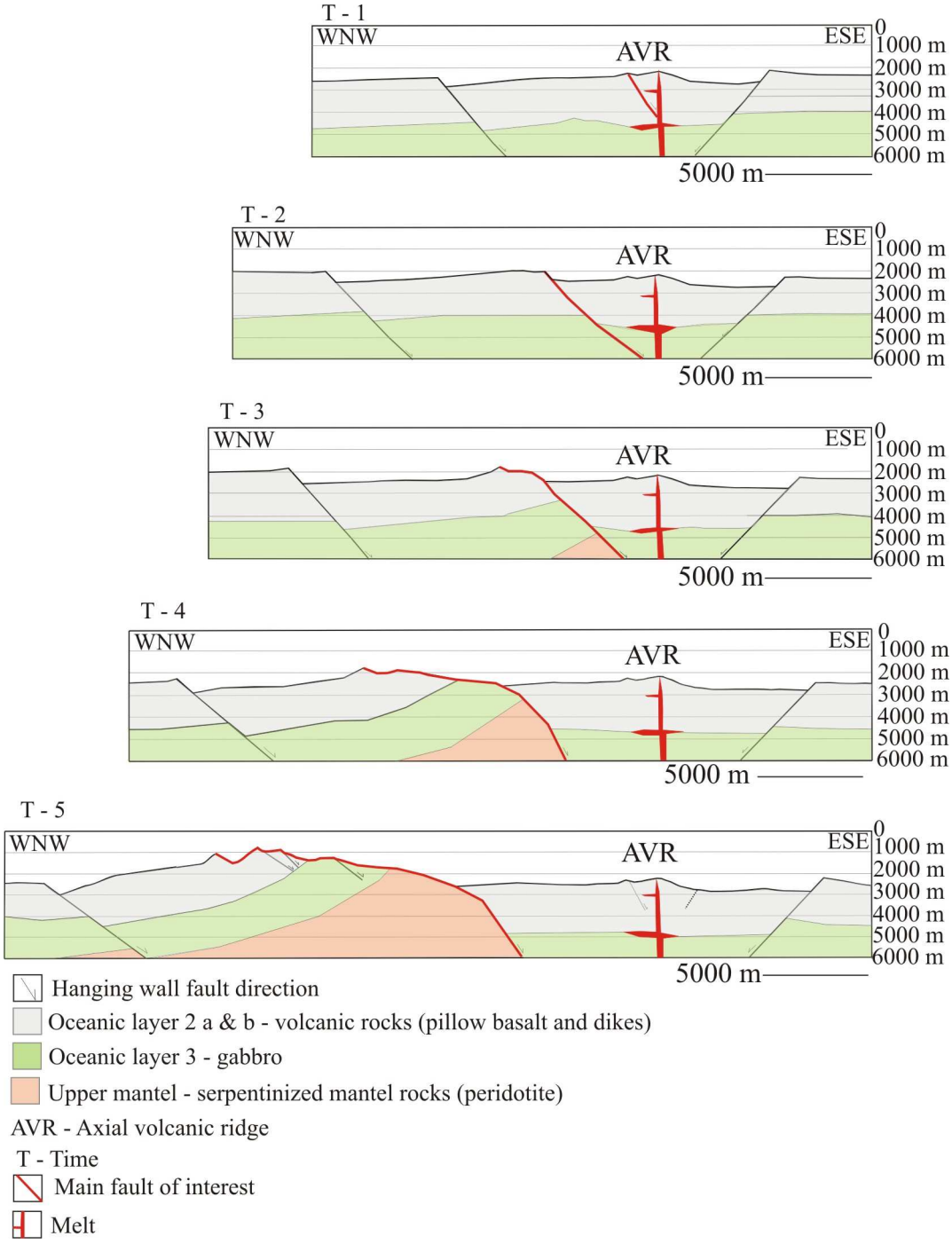

Figure 5.6: Model for evolution of oceanic core complex at the Mohns-Knipovich Ridge in area 2. No vertical exaggeration. See yellow box in Figure 5.4 for positioning.

T – 1 Faults initiate intersecting the AVR.

T – 2 The fault cluster evolves into one active detachment fault allowing larger amount displacement.

T – 3 Fault surface is characterized by flexure, also notice how the fault crest is rotated.

T – 4 Displacement in map view for the detachment fault is approximately 7 km. Gabbroic rock is exhumed at the seafloor. Also note how volcanic rock is continuously formed during in the axial valley.

T – 5 Extensive cross section of the oceanic lithosphere is exhumed with displacement of approximately 10 km. Faults initiate and intersect the exhumed surface. The detachment fault is terminated as a new fault forms, intersecting the AVR, thus now representing the active fault.

The cross sections proposed in Figure 5.4, 5.5 & 5.6 show that the assumed crustal thicknesses differ greatly for the two different models due to their tectonic setting. The most important difference is that the model for area 2 is situated adjacent to a heat anomaly (an AVR) which suggests altered rheological properties.
The difference between oblique- and orthogonal spreading faults has resulted in faults initiating at an angle to the rift trend in area 1 whereas they initiate orthogonal to the rift trend in area 2.

5.3.3. Existing models of oceanic core complex formation

The thermal state of a mid oceanic spreading ridge is an important contributor regarding deformation expression. There are several models for oceanic core complex formation proposed. The main difference in these is the assumed thermal state of the lithosphere dominating the phase of extension and how the detachment fault soles out with depth. The research is based on data such as bathymetric and fault maps, gravity and magnetic data, submersible investigations and rock samples collected either by submersibles, dredges or drilling. Both refraction and reflection seismic have been used to determine sediment cover and crustal layer thicknesses.

Models for continental lithospheric extension conclude that for a core complex to form in a continental environment heat flow has to be high so that the yield strength of the crust is low otherwise a symmetric rift will form (Buck, 1991). Previous published models for oceanic core complexes are contradictory to the high heat flow in that they assume amagmatic (tectonic) dominated extension (Tucholke et al., 1998 & 2001). This model has been developed from morphological characteristics, geological observations, and sampling of tectonic structures along the Mid Atlantic

Ridge. Here a detachment fault is proposed to cut through the whole thickness of the lithosphere, soling out at the brittle-ductile transition (Figure 5.7). In this model the detachment fault develops during a period of amagmatic accretion when the lithosphere is cold (strong) and the isotherms are depressed. The onset of amagmatic accretion results in detachment faulting exhuming the lower crust and upper mantle. The fault is terminated when magmatic activity raises the isotherm resulting in magmatic accretion of oceanic crust (Figure 5.7).

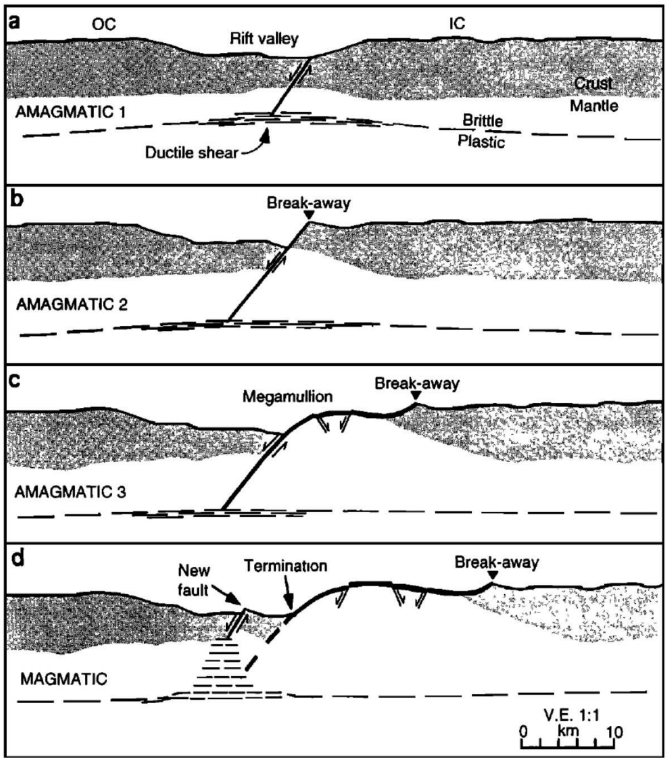

Figure 5.7: Schematic development of an oceanic core complex for an inner corner setting. From Tucholke et al. (1998)

a) The beginning of a long (1-2 Ma) amagmatic phase of seafloor accretion. A steep normal fault cuts through the brittle lithosphere and soles out in a ductile shear zone beneath the brittle-plastic transition.
b) With time the fault reaches greater depths as the isotherms, and hence the brittle-plastic zone, becomes depressed.
c) Continued slip exposes lower crust and upper mantle material in the footwall as the fault surface domes exhibiting corrugations (mullions).
d) A magmatic phase of seafloor spreading terminates the slip of the detachment fault that is in association with the core complex. This happens because a new fault initiates in the weakened (now hot) rift valley lithosphere.

Alternatively, it is proposed, from observations at the South West Indian Rise and the Mid-Atlantic Ridge that the detachment fault roots in the vicinity of a melt rich zone near the gabbro-dike transition in the shallow lithosphere (Dick et al., 1999; 2000 & 2008). Escartin et al. (2003) proposed that oceanic detachments root at shallow levels in the lithosphere, either at a melt rich zone at the gabbro-dike transition or within the altered lithosphere. This is based on observations from 15°45´N at the Mid Atlantic Ridge. Thus it has been demonstrated that detachments may also develop in the presence of active magmatism at the ridge axis.

Research of multiple core complexes between 13° - 15°N at the Mid Atlantic Ridge, including compound core complexes, has resulted in two models for multiple core complex formation (Smith et al., 2008). The first is a continuous model where a single detachment fault extends along the axis to include all of the core complexes and associated basins. The second is a discontinuous model in which local detachment faults form the core complexes and magmatic spreading forms the basins.

Numerical modeling suggests that the amount of magma emplaced by dikes can explain the fault geometry in settings where detachment core complexes form (slow to ultraslow class of spreading ridges) (Buck et al., 2005). Here a reduction in magma emplacement, to an account of half the spreading component, will favor large fault displacements, thus enabling prolonged displacement that can result in exposure of the lower crust and upper mantel.

5.3.4. Model proposed for the oceanic core complex at the Mohns-Knipovich Ridge in light of previous models

The model proposed in Figure 5.6 for the oceanic core complex at the Mohns-Knipovich Ridge Bend exhibits similar topography and exhumation history as the model proposed by Tucholke et al. (1998 & 2001) in Figure 5.7. A minor difference is that all the interpreted faults dip towards the rift axis in area 2. A fundamental difference is that the thermal state of the lithosphere is interpreted to be elevated for the model representing area 2. This is contradictory to the model proposed by Tucholke et al. (1998 & 2001) where the thermal state of the lithosphere is depressed

during detachment faulting. It should be noted that this model is proposed for inside corners at segment ends for slow spreading ridges, it is based on low magmatic activity that only periodically reaches the segment ends, terminating the detachment fault. This is opposed to the core complex inferred to form adjacent to an AVR which defines a segment center at a slow to ultraslow spreading ridge. Due to the proximity to the AVR it is reasonable to assume a melt rich zone at the gabbro-dike transition and the fault may sole out according to Dick et al. (1999; 2000 & 2008) and Escartin et al. (2003) in this transition. It must be noted that the data interpreted and presented in this thesis does not give direct insight as to how the fault propagates with depth and this has therefore not been illustrated for the model proposed

The evolutionary model proposed for core complex formation is characterized by both magmatic and fault accretion differing from the model assuming near pure fault accretion (Figure 5.7). Instead the model (Figure 5.6) corresponds to the numerical model of Buck et al. (2005) where faults with large displacement (detachment faults) form when half the plate separation at the ridge is due to dike intrusions. This coincides with small faults developing at the opposite side of the rift valley accreting smaller amounts of tectonic extension simultaneously as magmatic accretion accounts for the remaining component of extension.

The core complex at the Mohns-Knipovich Ridge Bend has been interpreted as a compound core complex (Section 4.4.3). It is therefore not necessarily straightforward which fault crest represents the detachment fault. It is possible that the detachment fault in reality is located further off axis and that the faults interpreted as detachment faults are actually rafted fault blocks on a larger detachment fault surface. This corresponds to the “continuous” model proposed by Smith et al. (2008). The detachment fault may, therefore alternatively, be the initial border fault at T – 1 in Figure 5.6, if not a fault further off-axis that may not be identified in the bathymetry.

5.4. Evolution of Feature C

The features described in Section 4.4.4 are not well constrained by previous studies and the mechanisms resulting in such features, therefore, relatively unknown. Feature A and B are characterized by faults on either side of the feature curving forming hard-link structures towards a common central area which consists of thoroughly faulted seafloor. Feature C is characterized by isochron off-axis faults which have linked together. Further off axis two faults are curving strongly off-axis intersecting an 11 km rugged topography. The rugged topography has been interpreted to represent a detachment fault surface (Section 4.4.4).

Keep & McClay (1997) described how rift systems and fault geometry are affected by multi-phases of rifting using analogue models. They argue that this is evident in the fault geometry for the central, 2°W - 4°E, Mohns Ridge. None of their test results show any resemblance to the features presented in Section 4.4.4, although this does not dismiss that the structures may be a consequence of change in spreading direction.

Figure 5.8 illustrates a model, developed during this study, of how Feature C may have evolved without incorporating the core complex interpretation. This is presented as there is uncertainty with the earlier, favored, interpretation since gravity collapse and/or multiple faults are also reasonable interpretations that could result in such morphological features. In the model (Figure 5.8) three initial faults form in the axial valley at T - 1. The AVR is only indicated at the present stage (T - 3). At T - 2 the faults have moved off axis and become border faults taking up more displacement. Two new faults form within the axial valley which terminates the growth of the faults on either side of the fault in the center. These two faults grow and curve towards the central fault off axis. Throughout the evolution the central fault experiences massive mass wasting and/or gravity collapse thoroughly degrading the fault crest. The faults on either side of the central fault show signs of gullies and sediment accumulations at the base. It is reasonable to suggest that the faults curving towards the off-axis central fault may propagate further towards each other, resulting in the rugged topography representing two degraded fault crests, although this is not incorporated in the model.

The system becomes extinct when new faults form in the rift valley and evolve to become border faults (T - 3) (Figure 5.8).

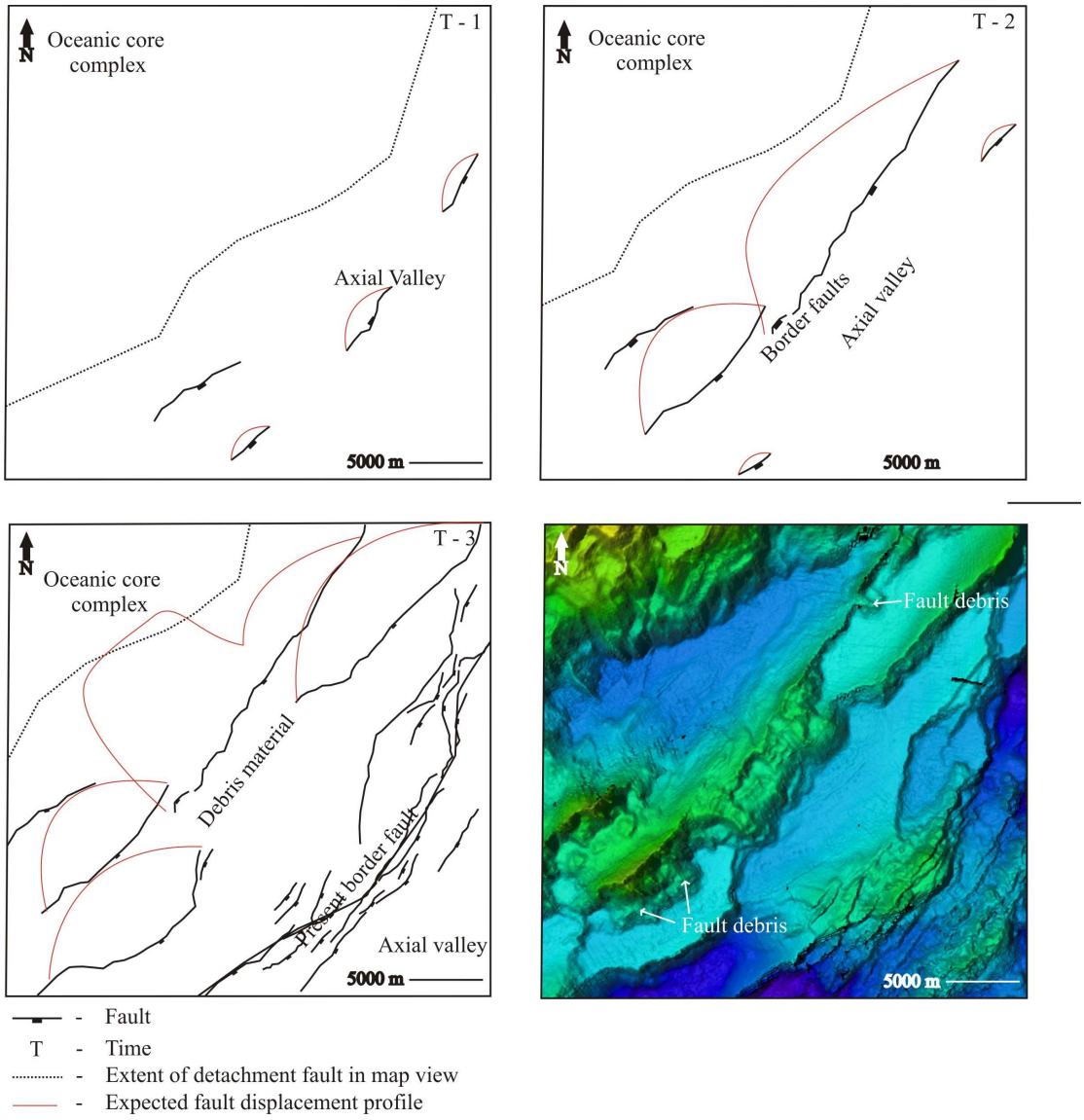

Figure 5.8: Model for evolution of Feature C. Color-coded bathymetric map of Feature C to the bottom right. Depth scale is indicated by the color bar in Figure 4.1. T - 3 is present time.

T - 1 Three faults form within the axial valley terminating a oceanic core complex (Section 4.4.3.)

T - 2 Faults grow and tend off axis becoming border faults. Two new faults are formed in the axial valley. Note that there is no fault growing in the central part resulting in the central border fault continuing to grow as seen from the displacement profile.

T - 3 The faults in relation (isochron) to the rugged topography is extinct as new border faults have formed in the axial valley. As seen from the Figure, this model produces an anomalous amount of sediments accumulating towards the axis from the central fault.

Feature C is situated directly off axis of an AVR as well as being in the vicinity of an extinct oceanic core complex situated further off-axis (Section 4.4.3). This indicates that the structure may be in a similar setting as the oceanic core complex, situated further off axis was, when exhumed. An alternative model incorporating core complex evolution is illustrated in Figure 5.9. This evolution is consistent with the interpretation where the middle fault evolves as a detachment fault that is rotated (backtilted) and flexures during exhumation. It also illustrates the involvement of elevated thermal conditions and lateral termination of a core complex.

In the initial stage the core complex, described in Section 4.4.3, is terminated as new faults develop in the axial valley, possibly intersecting an AVR (T - 1, Figure 5.9). The AVR is not indicated in the Figure for T - 1. It may be inferred that the thermal state of the lithosphere is depressed, possibly resulting in prohibiting and/or limiting diffusion creep and serpentinization (Jaroslow et al., 1996; Escartin et al., 1997). In the next stage (T - 2, Figure 5.9) the initial intra-rift faults have evolved to border faults and two new faults have formed within the axial valley. At this time it is presumed that all these faults are active. In the succeeding stage (T - 3, Figure 5.9) the intra-rift faults have grown and started to curve towards the center fault which now shows signs of doming and can be characterized as a detachment fault. The faults on either side are now extinct and the system consists of border faults stepping off-axis at the center where the detachment fault is situated. The faults curving towards the central fault from both sides do not propagate far enough to terminate the growth of the central fault. At the present stage (T - 4 in Figure 5.9) the system is extinct and new border faults are now active. It can be assumed that a similar thermal state that terminated the previous core complex has resulted in the extinction. This early stage of core complex evolution exposes gabbroic rock suggesting lower crustal rock (oceanic layer 3). The model's final stage (T - 4) coincides with time 4 in the model presented for the core complex evolution in Figure 5.6, thus representing a core complex that has not evolved to the same extent as the larger core complex situated further off-axis.

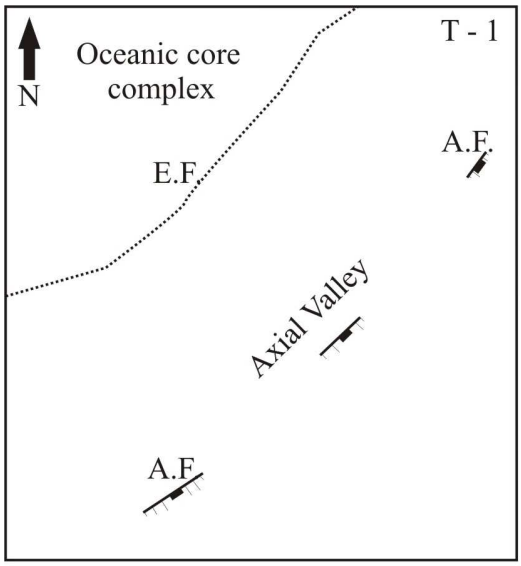

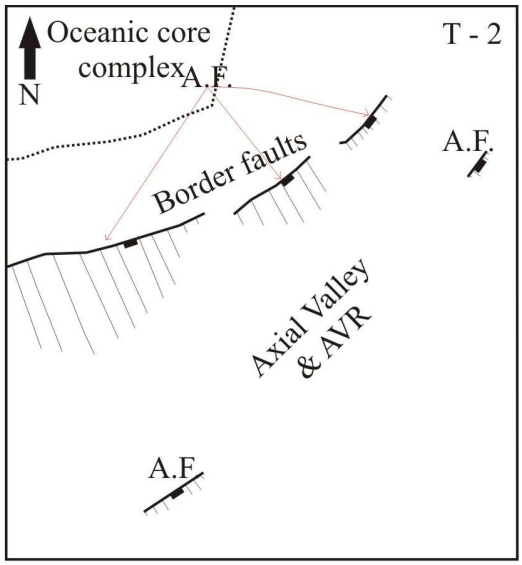

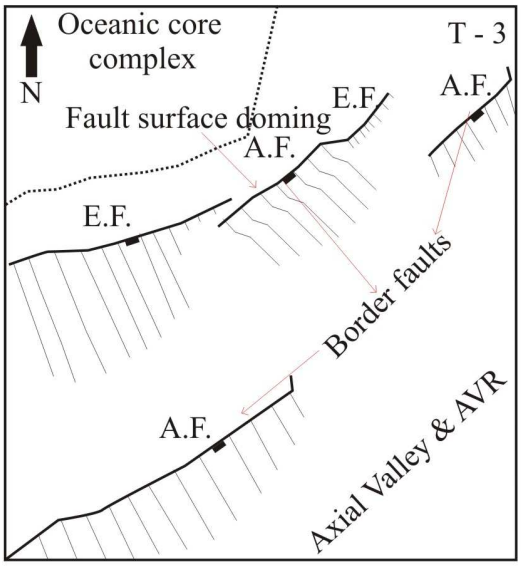

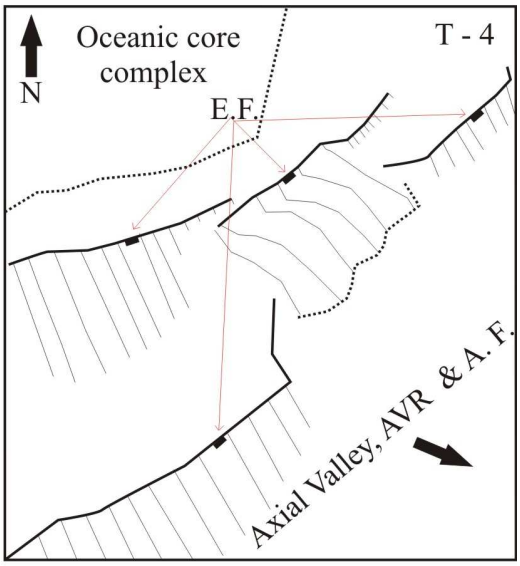

- Fault
A.F. - Active fault
E.F. - Extinct fault
T - Time
..... - Extent of corrugated detachment surface
\ \ - Fault surface

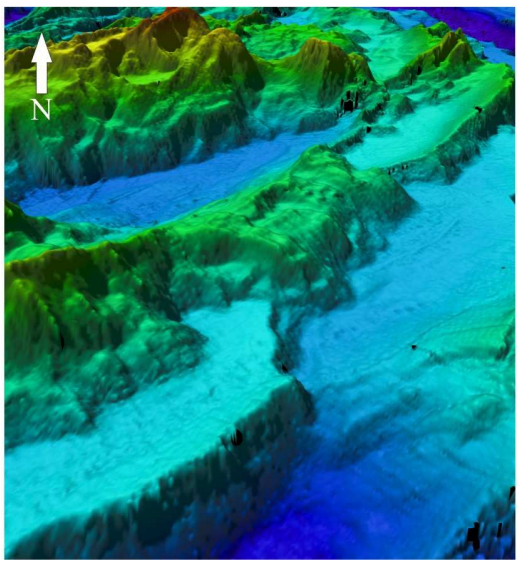

Figure 5.9 (previous page): Model of the evolution of Feature C where the central fault is interpreted as a dome-shaped detachment fault exposing gabbroic rock at its base towards the axial valley in Section 4.4.4. Scale is not presented as the capture view is from the south thus distorting the scale (i.e. the scale of features to the bottom of the Figure is strongly exaggerated in comparison to features at the top of the Figure). Vertical exaggeration: 3. Color-coded bathymetric map to the bottom right, depth scale is indicated by color bar in Figure 4.1. T - 4 is present time.

T - 1 The oceanic core complex described in Section 4.4.3. is terminated when three faults form within the axial valley.

T-2 The initial three faults evolve to border faults. Two new faults are initiated within the axial valley.

T - 3 The border faults to both sides of the central fault become extinct as the two faults in the axial valley continue to grow and start to curve slightly towards the central fault further off-axis. At this time the central off axis fault starts to flexure.

T - 4 The faults in relation (isochron) to the detachment fault have become extinct. The central fault furthest off-axis exposing gabbroic rock has thus terminated at an immature stage compared to the core complex situated further off-axis described in Section 4.4.3.

5.5. Brittle-ductile transition elevation - suggested cause of detachment faulting and lateral termination of core complexes

The model in Figure 5.9 raises several important questions; i) why does the fault flexure only happens locally for an 11 km long detachment fault? And, ii) why do the two faults lateral to the detachment fault not terminate the growth of the detachment fault by propagating further towards each other? It is reasonable to suggest that the detachment fault has formed due to an adjacent AVR which may be necessary to create the right thermal conditions for detachment faulting with subsequent flexure of the footwall. The positioning of the AVR, which obviously reveals the area with the highest volcanic activity in the area, is best seen in Figure 4.14 where it is situated directly adjacent to the interpreted detachment fault in Feature C. Evidence from gravity data (Lin et al., 1990) and magnetic data (Hellevang & Pedersen, 2003), from the Mid-Atlantic Ridge and the Mohns Ridge respectively, show that accretion of magma at the ridge is focused at discrete centers along the spreading axis (i.e. an AVR). Okino et al. (2002) proposed that the rate of passive upwelling of mantle is controlled by the effective rate of plate spreading. The effective rate of plate

spreading is lower for oblique spreading ridges and higher for orthogonal spreading ridges. This indicates more mantle upwelling at the Mohns-Knipovich Bend. Hellevang & Pedersen (2003) argue that this is the reason for elevated bathymetry and close spacing of AVRs at the Mohns-Knipovich Bend in comparison to the central and southern Mohns Ridge.

It is proposed that the detachment fault in Feature C initiated and evolved to its present extent because the lateral faults further towards the axis could not propagate past a locally elevated brittle-ductile transition (Figure 5.10). If faults adjacent to the detachment fault exist they must, therefore, have small displacements and/or be covered by sediments, as they do not appear in the bathymetry. Depressing the brittle-ductile transition zone may allow faults to propagate to deeper depths, thus it may be more energy efficient to continue displacement along a fault further towards the rift axis, thus allowing termination of the detachment fault.

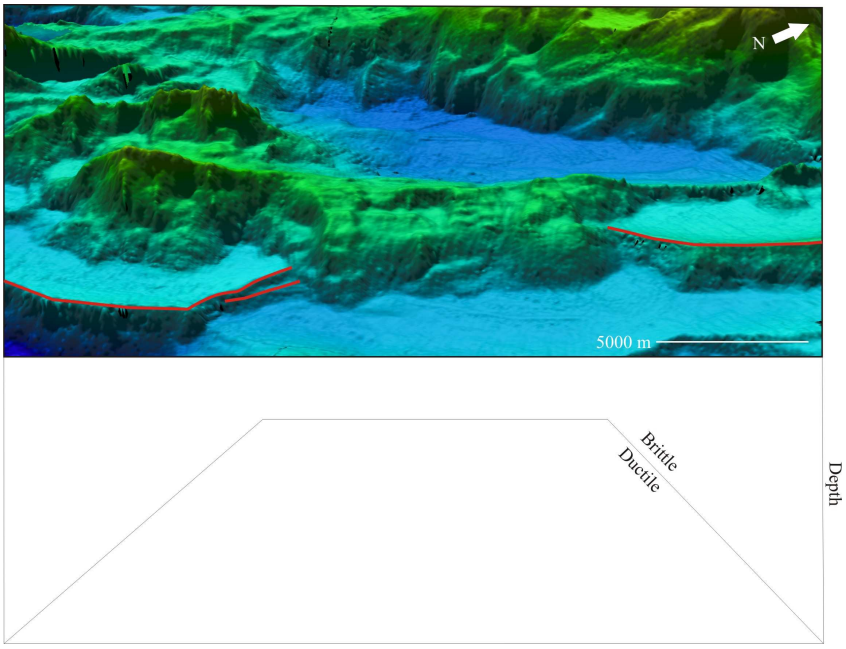

Figure 5.10: Rotated color-coded bathymetry of Feature C. Color scale in Figure 4.1. Beneath is a schematic brittle-ductile transition Figure. Lateral fault crests, further towards the axial valley, are marked with a red line. The brittle-ductile transition elevation implies a locally higher heat flow, which is suggested to be a result of the adjacent AVR 15. The AVR lies directly adjacent of the central detachment fault during exhumation. The anomalous heat flow affects the rheology allowing detachment faulting, as well as constraining the lateral faults further towards the axial valley.

The proposed evolution of the detachment fault in Feature C (Figure 5.9) adjacent to the AVR and subsequent brittle-ductile transition explains the mechanisms of how an oceanic core complex may evolve as well as illustrating lateral termination. For the compound core complex described in Section 4.4.3 it is suggested that a similar elevation of the brittle-ductile transition occurred due to higher heat flow and lithospheric temperatures in response to an AVR, allowing great amounts of displacement to occur along the detachment fault. The principal of lateral termination due to an elevated brittle-ductile transition applies to the compound core complex and can explain its northeastern step. Here the detachment fault *a* in Figure 4.12 is active as fault *b* situated northeast propagates southwest (see correlation Figure 4.13). Fault *b* forms a hard-link structure with a smaller fault (hard-link structure Figure 10.b). The smaller fault is interpreted to represent a fault that has formed on the detachment surface during exhumation. To the northeast fault *d* (Figure 4.12) initiates and begins to evolve. This happens simultaneously as fault *a* continues to grow. Fault *d* is active as fault *a* becomes extinct, resulting in further exhumation of both the southwest and northeast dome (Section 4.4.3)

The lateral termination of core complexes in this section explains why the faults situated lateral and further towards the axis do not propagate to terminate the core complex growth. This happens because the rheological properties are altered due to an elevation of the thermal state, which is suggested to further prohibit fault propagation and therefore also termination.

This principal may be applied to the compound core complex presented in Smith et al. (2006 & 2008) (Figure 5.11). Here it can be inferred that fault 1, 3 and 4 initiated as a detachment faults. At a later stage, fault 1 and 3 develop to represent a compound core complex as fault 2 initiates towards the axis lateral to faults 1, 3 and 4 and propagates in the north-south direction. Fault 2 has not propagated past the now doming core complexes (1, 3 and 4 in Figure 5.11) and it is suggested that this may be due to an elevation of the brittle-ductile transition adjacent to these core complexes. Thus, the compound core complex and core complex 3 are active simultaneously as core complex 2.

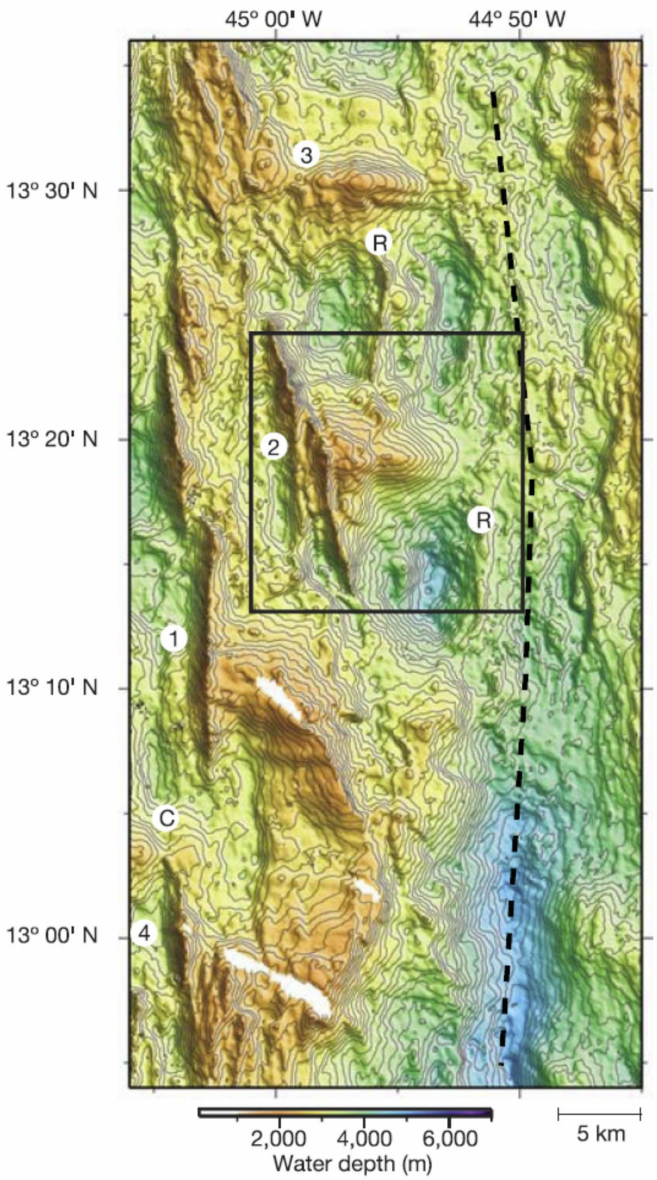

Figure 5.11: Compound core complex at the Mid Atlantic Ridge. Contour interval is 50 m. The dashed line indicates the spreading axis. R represents topographic ridges inferred to be breakaways for new detachment surfaces. Numbers are core complexes. C represents a compound core complex composed of complex 1 and 4. Note how complex 3 and especially 2 dip into the axial valley. From Smith et al. (2006 & 2008).

In summary, regarding core complex formation, previous publications point out tectonic (amagmatic) extension to be the main reason for core complex formation (Tucholke et al., 1998 & 2001). This has been a subject of debate in more recent literature (e.g., Dick et al., 1999; 2000 & 2008; Escartin et al., 2003). Common is lower volcanic activity, as the ridges where core complexes are reported are situated in slow to ultraslow spreading ridges. It is now generally agreed that there is interplay

between magmatic and tectonic extension that results in oceanic core complex formation (Buck et al., 2005). This is in correspondence to this thesis work where volcanic activity together with tectonic accretion results in favorable conditions for core complex formation for this particular setting.

5.6. Are several oceanic core complex evolutionary stages present?

In earlier sections a mature compound core complex has been identified, described and an evolutionary model has been presented. The displacement of the core complex is between 10 – 12 km, thus exhibiting an extensive cross section of the lower crust and upper mantle lithosphere. This is evident from rock dredges which have recovered serpentinized mantle peridotite. Another interpreted detachment fault representing a core complex is situated further towards the axis. This detachment fault exhibits displacement of approximately 5 km. At the base of the detachment fault gabbroic rock has been recovered during dredging indicating exposure of lower crust (oceanic layer 3). As implied in earlier sections this latter detachment fault is inferred to represent an early stage of core complex evolution. Mechanisms have been proposed for the evolution of these core complex features. Both are inferred to develop in the vicinity of hot asthenosphere elevating the brittle-ductile transition.

Bruvoll et al. (2009) suggested an incipient detachment fault corresponding to Feature A in Figure 4.14. In light of the discussion on the evolution for the two core complexes, it seems likely that this feature may represent an initial stage of core complex formation. This feature is situated adjacent to AVR 15 which is inferred to be at an early growth stage. Feature A is interpreted to represent the fault(s) that terminated the growth of Feature C and has initiated within an AVR (Section 4.4.4, Figure 4.14). It has further evolved to become a boarder fault. Detachment faulting is suggested to initiate during a phase of volcanism, resulting in favourable thermal conditions for detachment faulting for the study area. Feature A is suggested to correspond to the inferred incipient breakaway ridges further south along the Mid-Atlantic Ridge (ridge labelled “R” in Figure 5.11).

The resemblance is striking between Feature A and B (Figure 4.14) and the compound core complex (Section 4.4.3) and it is suggested that these faults, given the correct thermal state of the lithosphere, may evolve to become a compound core complex.

6. CONCLUSIONS

The overall objective of this thesis has been to document contrasting tectonic processes at the northeastern Mohns Ridge, with focus on fault evolution and core complex formation. The main conclusions of this study are:

- The western flank has initially consisted of several separate faults which have linked together with the surrounding faults forming larger faults. In the next stage the large fault links together with another fault resulting in increased length followed by redistribution of displacement. This illustrates how the faults grow in horizontal direction by forming relay structures.

- Maximum displacement-length relation, at least for this Mid-Ocean Ridge, conforms to displacement-length data from continental rift settings and other fault populations in spite of differences in crustal thickness and rheology.

- The local high at the segments ends between segment 13 and 14 are interpreted to be the result of volcanic processes, or more feasible tectonic extension. The characteristics of this transfer zone are conforming to observations in non volcanic settings.

- It is observed that the tectonic dominated area 1 is characterized by symmetrical profiles with slight fault rotation off-axis. This is in contrast to the asymmetric profiles for area 2 where a great amount of fault rotation occurs, forming basins off-axis of the fault crest. The thermal state of the lithosphere in area 1 and 2 is suggested to be the main contributing reason for the different topographic expressions. Area 1 is inferred to be characterized by a higher degree of tectonic accretion whereas area 2 is inferred to be characterized by interplay between both volcanic and tectonic accretion which has resulted in several core complexes and one suggested incipient stage of core complex formation.

- Lateral termination of core complexes has not earlier been subject for debate. The higher heat flow and lithospheric temperatures in the vicinity of the AVR are believed to result in the lateral faults not propagating past the locally elevated brittle-ductile transition. This principal appears to conform to data from core complexes indentified further south along the Mid-Atlantic Ridge.

REFERENCES

Abelson, M., & Agnon, A. (1997). Mechanics of oblique spreading and ridge segmentation. *Earth and Planetary Science Letters, 148*, 405-421.

Allerton, S., Searle, R. C., & Murton, B. J. (1996). Bathymetric segmentation and faulting on the Mid-Atlantic Ridge, 24°00'N to 24°40'N. In C. J. MacLeod, P. A. Tylor & C. Walker (Eds.), *Tectonic, Magmatic, Hydrothermal and Biological Segmentation of Mid-Ocean Ridges* (Vol. 118, pp. 49-60). London: Geological Society Special Publication.

Baker, E. T., Chen, Y. J., & Phipps Morgan, J. (1996). The relationship between near-axis hydrothermal cooling and the spreading rate of mid-ocean ridges. *Earth and Planetary Science Letters, 142*, 137-145.

Blackman, D. K., Cann, J. R., Janssen, B., & Smith, D. (1998). Origin of extensional core complexes: Evidence from the Mid-Atlantic Ridge at Atlantis Frature Zone. *Journal of Geophysical Research, 103*, 21315-21333.

Bown, J. W., & White, R. S. (1994). Variation with spreading rate of oceanic crustal thickness and geochemistry. *Earth and Planetary Science Letters, 121*, 435-449.

Breivik, A. J., Mjelde, R., Faleide, J. I., & Murai, Y. (2006). Rates of continental breakup magmatism and seafloor spreading in the Norway Basin - Iceland plume interaction. *Journal of Geophysical Research, 111*, 1-17. B07102, doi:10.1029/2005JB004004.

Bruvoll, V., Breivik, A. J., Mjelde, R., & Pedersen, R. B. (2009). Burial of the Mohns-Knipovich seafloor spreading ridge by the Bear Island fan: time constraints on tectonic evolution from seismic stratigraphy. *Tectonics*, in pres.

Buck, R. W. (1988). Flexural rotation of normal faults. *Tectonics, 7*, 959-973.

Buck, R. W. (1991). Modes of continental lithospheric extension. *Journal of Geophysical Research, 96*, 161-178.

Buck, W. R., Lavier, L. L., & Poliakov, A. N. B. (2005). Modes of faulting at mid-ocean ridges. *Nature, 434*, 719-723.

Cann, J. R., Prichard, H. M., Malpas, J. G., & Xenophontos, C. (2001). Oceanic inside corner detachments of the Limassol Forest area, Troodos ophiolite, Cyprus. *Journal of the Geological Society, 158*, 757-767.

Cannat, M., Mevel, C., Maia, M., Deplus, C., Durand, C., Gente, P., Agrinier, P., Belarouchi, A., Dubuisson, G., Humler, E., & Reynolds, J. (1995). Thin crust, ultramafic exposures, and rugged faulting patterns at the Mid-Atlantic Ridge (22°-24N°). *Geology, 23*, 49-52.

Childs, C., Watterson, J., & Walsh, J. (1995). Fault overlap zones within developing normal fault systems. *Journal of the Geological Society, 152*, 535-549.

Crane, K., Doss, H., Vogt, P., & Sundvor, E. (1999). Morphology of the northeastern Mohns Ridge; results from SeaMARC II surveys in the Norwegian-Greenland Sea. *Exploration and Mining Geology, 8*, 323-339.

Crane, K., Doss, H., Vogt, P., Sundvor, E., Cherkashov, G., Poroshina, I., & Joseph, D. (2001). The role of the Spitsbergen shear zone in determining morphology, segmentation and evolution of the Knipovich Ridge. *Marine Geophysical Researches, 22*, 153-205.

Crane, K., Sundvor, E., Foucher, J. P., Hobart, M., Myhre, A. M., & LeDouaran, S. (1988). Thermal evolution of the western Svalbard margin. *Marine Geophysical Researches, 9*, 165-194.

Dauteuil, O. (1995). Fault pattern from seabeam processing: The western part of the Blanco Fracture Zone (NE pacific). *Marine geophysical researches, 17*, 17-35.

Dauteuil, O., & Brun, J. P. (1993). Oblique rifting in a slow-spreading ridge. *Nature, 361*, 145-148.

Dauteuil, O., & Brun, J. P. (1996). Deformation partitioning in a slow spreading ridge undergoing oblique extension: Mohns Ridge, Norwegian Sea. *Tectonics, 15*, 870-884.

Dick, H. J. B., Lin, J., & Schouten, H. (2003). An ultraslow-spreading class of ocean ridge. *Nature, 426*, 405-412.

Dick, H. J. B., Natland, J. H., Alt, J. C., Bach, W., Bideau, D., Gee, J. S., Haggas, S., Hertogen, J. G. H., Hirth, G., Holm, P. M., Ildefonse, B., Iturrino, G. J., John, B. E., Kelley, D. S., Kikawa, E., et al. (2000). A long in situ section of the lower ocean crust: results of ODP Leg 176 drilling at the Southwest Indian Ridge. *Earth and Planetary Science Letters, 179*, 31-51.

Dick, H. J. B., Schouten, H., John, B., Kinoshita, M., Natland, J. H., MacLeod, C. J., & Hirth, G. (1999). Evidence of a "melt lense" equivalent in the lower crust at an ultraslow spreading ridge. *American Geophysical Union* (Fall meeting abstract).

Dick, H. J. B., Tivey, M. A., & Tucholke, B. E. (2008). Plutonic foundation of a slow-spreading ridge segment: Oceanic core complex at Kane Megamullion, 23°30´N, 45°20´W. *Geochmistry, Geophysics, Geosystems, 9*, 1-44. Q05014, doi:10.1029/2007GC001645.

Eldholm, O., Skogeid, J., Sundvor, E., & Myhre, A. M. (1990). The Norwegian-Greenland Sea. In A. Grantz, L. Johnson & J. F. Sweeney (Eds.), *The Geology of North America* Vol. L, The Arctic Ocean Region (pp. 351-364).Colorado: The Geological Society of America.

Escartin, J., Hirth, G., & Evans, B. (1997). Effects of serpentinization on the lithospheric strength and the style of normal faulting at slow-spreading ridges. *Earth and Planetary Science Letters, 151*, 181-189.

Escartin, J., MacLeod, C. J., & McCraig, A. M. (2003). Constraints on deformation conditions and the origin of oceanic detachmetns: The Mid-Atlantic Ridge core complex at 15°45´N. *Geochmistry, Geophysics, Geosystems, 4*, 1-37. 1067, doi:10.1029/2002GC000472.

Fossen, H., & Hesthammer, J. (1997). Geometric analysis and scaling relations of deformation bands in porous sandstone. *Journal of Structural Geology, 19*, 1479-1493.

GardlineSurveysLimited. (2001). *The Norwegian Petroleum Directorate, Law of the Sea Survey 2001 July-August* (Data acquisition and processing report).

Geli, L., Renard, V., & Rommevaux, C. (1994). Ocean crust formation processes at very slow spreading centers: A model for the Mohns Ridge, near 72°N, based on magnetic, gravity, and seismic data. *Journal of Geophysical Research, 99*, 2995-3013.

Hellevang, B., & Pedersen, R. B. (2003). Segmentation of the oblique spreading Mohns Ridge and the Mohns-Knipovich bend: interpretations from swath bathymetry and geophysical data. Unpublished Doctor Scientiarum thesis. Department of Earth Science, University of Bergen.

Hellevang, B., & Pedersen, R. B. (2005). Magmatic segmentation of the northern Knipovich Ridge: Evidence for high-pressure fractionation at an ultraslow spreading ridge. *Geochmistry, Geophysics, Geosystems, 6*, 1-17. doi:10.1093/petrology/egm081

Hesthammer, J., & Fossen, H. (1999). Evolution and geometries of gravitational collapse structures with examples from the Statfjord Field, northern North Sea. *Marine and Petroleum Geology, 16*, 259-281.

Hinz, K., Eldholm, O., Block, M., & Skogeid, J. (1993). Evolution of North Atlantic volcanic continental margins. In J. R. Parker (Ed.), *Petroleum Geology of Northwest Europe: Proceedings of the Fourth Conference* (pp. 901-913). London: Geological Society of London.

Jackson, C. A. L., Gawthorpe, R. L., & Sharp, I. R. (2002). Growth and linkage of the East Tanke faul zone, Suez rift: structural style and syn-rift stratigraphic response *Journal of the Geological Society, 159*, 175-187.

Jakobsson, M., Macnab, R., Mayer, L., Anderson, R., Edwards, M., Hatzky, J., Schenke, H. W., & Johnson, P. (2008). An improved batymetric protrayal of the Arctic Ocean: Implications or ocean modeling and geological, geophysical and oceanographic analyses. *Geophysical Research Letters, 35*.

Jaroslow, G. E., Hirth, G., & Dick, H. J. B. (1996). Abyssan peridotite mylonites: implications for grain-size sensitive flow and strain localization in the oceanic lithosphere. *Tectonophysics, 256*, 17-37.

Kandilarov, A., Landa, H., Mjelde, R., Pedersen, R. B., Okino, K., & Murai, Y. (2009). Crustal structure of the ultra-slow spreading Knipovich Ridge, North Atlantic, along a presumed ridge segment center. *Marine Geophysical Researches*, in pres.

Kandilarov, A., Mjelde, R., Okino, K., & Murai, Y. (2008). Crustal structure of the ultra-slow spreading Knipovich Ridge, North Atlantic, along a presumed amagmatic protion of oceanic crustal formation. *Marine Geophysical Researches, 29*, 109-134.

Kearey, P., & Vine, F. (1990). *Global Tectonics*: Blackwell Science.

Keep, M., & McClay, K. R. (1997). Analogue modelling of multipase rift systems. *Tectonophysics, 273*, 239-270.

Klingelhofer, F., Geli, L., Matias, L., Steinsland, N., & Mohr, J. (2000b). Crustal structure of a super-slow spreading centre:a seismic refraction study of Mohns Ridge, 72° N. *Geophysical Journal International, 141*, 509-526.

Klingelhofer, F., Geli, L., & White, R. S. (2000a). Geophysical and geochemical constraints on crustal accretion at the very-slow spreading Mohns Ridge. *Geophysical Research Letters, 27*, 1547-1550.

Kodaira, S., Mjelde, R., Gunnarsson, K., Shiobara, H., & Shimamura, H. (1998a). Evolution of oceanic crust on the Kolbeinsey Ridge, north of Iceland, over the past 22 Myr. *Terra Nova, 10*, 27-31.

Kodaira, S., Mjelde, R., Gunnarsson, K., Shiobara, H., & Shimamura, H. (1998b). Structure of the Jan Mayen microcontinent and implications for its evolution. *Geophysical Journal International, 132*, 383-400.

Kristoffersen, Y., & Talwani, M. (1977). Extinct triple junction south of Greenland and the Tertiary motion of Greenland relative to North America. *Geol Soc Am Bull, 88*, 1037-1049.

Lavier, L. L., Buck, R., & Poliakov, A. N. B. (1999). Self-consistent rolling-hinge model for the evolution of large-offset low-angle normal faults. *Geology, 27*, 1127-1130.

Lawver, L. A., Mullen, R. D., Spivastava, S. P., & Toest, W. (1990). The opening of the Arctic Ocean. In U. Bleil & J. Thiede (Eds.), *Geological History of the Polar Oceans: Arctic Versus Antarctic* (pp. 29-62). Netherland: Kluwer Academic Publishers.

Lin, J., Purdy, G. M., Schouten, H., Sempere, J.-C., & Zervas, C. (1990). Evidence from gravity data for focused magmatic accretion along the Mid-Atlantic Ridge. *Nature, 344*.

Lundin, E., & Dore, A. G. (2002). Mid-Cenozoic post-breakup deformation in the `passive' margins bordering the Norwegian-Greenland Sea. *Marine and Petroleum Geology, 19*, 79-93.

Macdonald, K. C. (1982). Mid-Ocean Ridges: Fine Scale Tectonic, Volcanic and Hydrothermal Processes Within the Plate Boundary Zone. *Annual Review of Earth and Planetary Sciences, 10*, 155-190.

Macdonald, K. C., Fox, P. J., Perram, L. J., Eisen, M. F., Haymon, R. M., Miller, S. P., Carbotte, S. M., Cormier, M. H., & Shor, A. N. (1988). A new view of the mid-ocean ridge from the behaviour of ridge-axis discontinuities. *Nature, 335*, 217-225.

Macdonald, K. C., Scheirer, D. S., & Carbotte, S. M. (1991). Mid-Ocean Ridges: Discontinuities, Segments and Giant Cracks. *Science, 253*, 986-994.

McClay, K. R., & White, M. J. (1995). Analogue modelling of orthogonal and oblique rifting. *Marine and Petroleum Geology, 12*, 137-151.

Michael, P. J., Langmuir, C. H., Dick, H. J. B., Snow, J. E., Goldstein, S. L., Graham, D. W., Lehnert, K., Kurras, G., Jokat, W., Muhe, R., & Edmonds, H. N. (2003). Magmatic and amagmatic seafloor generation at the ultraslow-spreading Gakkel ridge, Arctic Ocean. *Nature, 423*, 956-961.

Mjelde, R., Breivik, A. J., Raum, T., Mittelstaedt, E., Ito, G., & Faleide, J. I. (2008). Magmatic and tectonic evolution of the North Atlantic. *Journal of the Geological Society, 165*, 31-42.

Moore, J. M., & Schultz, R. A. (1999). Processes of faulting in jointed rocks of Canyonlands National Park, Utah. *Geological Society of America Bulletin, 111*, 808-822.

Mosar, J., Lewis, G., & Torsvik, T. (2002). North Atlantic sea-floor spreading rates: implications for the Tertiary development of inversion structures of the Norwegian-Greenland Sea. *Journal of the Geological Society, 159*, 503-515.

Neumann, E. R., & Schilling, J. G. (1984). Petrology of basalts from the Mohns-Knipovich Ridge; the Norwegian-Greenland Sea. *Contributions to Mineralogy and Petrology, 85*, 209-223.

Okino, K., Curewitz, D., Asada, M., Tamaki, K., Vogt, P., & Crane, K. (2002). Preliminary analysis of the Knipovich Ridge segmentation: influence of focused magmatism and ridge obliquity on an ultraslow spreading system. *Earth and Planetary Science Letters, 202*, 275-288.

Okino, K., Matsuda, K., Christie, D. M., Nogi, Y., & Koizumi, K. (2004). Development of oceanic detachment and asymmetric spreading at the Australian-Antarctic Discordance. *Geochmistry, Geophysics, Geosystems 5*. Q12012, doi:10.1029/2004GC000793.

Parson, L. M., Murton, B. J., Searle, R. C., Booth, D., Evans, J., Field, P., Keeton, J., Laughton, A., McAllister, E., Millard, N., Redbourne, L., Rouse, I., Shor, A. N., Smith, D., Spencer, S., Summerhayes, C., & Walker, C. (1993). En echelon axial volcanic ridges at the Reykjanes Ridge: a life cycle of volcanism and tectonics. *Earth and Planetary Science Letters, 117*, 73-87.

Peacock, D. C. P., & Parfitt, E. A. (2002). Active relay ramps and normal fault propagation on Kilauea Volcano, Hawaii. *Journal of Structural Geology, 24*, 729-742.

Pedersen, R. B., Thorseth, I. H., Nygaard, T. E., Lilley, M., & Kelley, D. S. (2009). Hydrothermal activity along the Arctic Mid-Ocean Ridge. In P. Rona, C. Devey, J. Dyment & B. Murton (Eds.), *Diversity of Hydrothermal, Systems on Slow-spreadig Ocean Ridges* (pp. in pres). Washington, D.C.: American Geophysical Union.

Pedersen, R. B., Thorseth, I. H., Olson, E., Hellevang, H., Okland, I., Baumberger, T., Lilley, M., Bruvoll, V., Mjelde, R., & Haflidason, H. (2007). Hydrothermal activity and core complex formation at the Arctic Mid-Ocean Ridge: An overview of preliminary results of the H2DEEP expedition to the southern Knipovich Ridge at 73N. *American Geophysical Union*(Fall Meeting abstract).

Phipps-Morgan, J., Harding, A., Orcutt, J., Kent, G., & Chen, Y. J. (1994). An Observational and Theoretical Synthesis of Magma Chamber Geometry and Crustal Genesis along a Mid-ocean Ridge Spreading Centre. In M. P. Ryan (Ed.), *Magmatic Systems* (pp. 139-178). San Diego: Academic Press.

Ranero, C. R., & Reston, T. J. (1999). Detachment faulting at ocean core complexes. *Geology, 27*, 983-986.

Reston, T. J., Weinrebe, W., Grevemeyer, I., Flueh, E. R., Mitchell, N. C., Kirstein, L., Kopp, C., Kopp, H., & 47/2, a. p. o. M. (2002). A rifted inside corner massif on the Mid-Atlantic Ridge at 5°S. *Earth and Planetary Science Letters, 200*, 255-269.

Roberts, A. M., Yielding, G., Kusznir, N. J., Walker, I. M., & Dorn-Lopez, D. (1995). Quantitative analysis of Triassic extension in the northern Viking Graben. *Journal of the Geological Society, 152*, 15-26.

Robinson, C. J., Bickle, M. J., Minshull, T. A., White, R. S., & Nichols, A. R. L. (2001). Low degree melting under the Southwest Indian Ridge: the roles of mantle temperature, conductive cooling and wet melting. *Earth and Planetary Science Letters, 188*, 383-398.

Schultz, R. A., Soliva, R., Fossen, H., Okubo, C. H., & Reeves, D. M. (2008). Dependence of displacement-length scaling relations for fractures and deformation bands on the volumetric changes across them. *Journal of Structural Geology, 30*, 1405-1411.

Searle, R. C., & Escartin, J. (2004). The Rheology and Morphology of Oceanic Lithosphere and Mid-Ocean Ridges. In C. R. German, J. Lin & L. M. Parson (Eds.), *Mid-Ocean Ridges: Hydrothermal interactions between the lithosphere and oceans* (pp. 63-94). Washington DC: American Geophysical Union.

Smith, D. K., Cann, J. R., & Escartin, J. (2006). Widespread active detachment faulting and core complex formation near 13°N on the Mid-Atlantic Ridge. *Nature, 422*, 440-443.

Smith, D. K., Escartin, J., Schouten, H., & Cann, J. R. (2008). Fault rotation and core complex formation: Significant processes in seafloor formation at slow-spreading mid-ocean ridges (Mid-Atlantic Ridge, 13°-15°N). *Geochmistry, Geophysics, Geosystems, 9*, 1-23.Q03003, doi:10.1029/2007GC001699.

Spencer, J. E. (1999). Geologic continuous casting below continental and deep-sea detachment faults and at the striated extrusion of Sacsayhaman, Peru. *Geology, 27*, 327-330.

Talwani, M., & Eldholm, O. (1977). Evolution of the Norwegian-Greenland Sea. *Geological Society of America bulletin, 88*, 969-999.

Torsvik, T. H., Mosar, J., & Eide, E. A. (2001). Cretaceous-Tertiary geodynamics: a North Atlantic exercise. *Geophysical Journal International, 146*, 850-866.

Tucholke, B. E., Fujioka, K., Ishihara, T., Hith, G., & Kinoshita, M. (2001). Submersible study of an oceanic megamullion in the central North Atlantic. *Journal of Geophysical Research, 106*, 16145-16161.

Tucholke, B. E., & Lin, J. (1994). A geological model for the structure of ridge segments in slow spreading ocean crust. *Journal of Geophysical Research, 99*, 11937-11958.

Tucholke, B. E., Lin, J., & Kleinrock, M. C. (1998). Megamullions and mullion structure defining oceanic metamorphic core complexes on the Mid-Atlantic Ridge. *Journal of Geophysical Research, 103*, 9857-9866.

Vogt, P. (1980). Morphology and magmatic anomalies north of Iceland. *Journal of Geophysics, 47*, 67-80.

Vogt, P. (1986). Geophysical and Geochemical signatures and plate tectonics. In B. G. Hurdle (Ed.), *The Nordic Seas* (pp. 413-662). New York: Springer Verlag.

Walsh, J., & Watterson, J. (1991). Geometric and kinematic coherence and scale effects in normal fault systems. *Geological Society Special Publication, 56*, 193-203.

White, R. S., Minshull, T. A., Bickle, M. J., & Robinson, C. J. (2001). Melt Generation at Very Slow-Spreading Oceanic Ridges: Constraints from Geochemical and Geophysical Data. *Journal of Petrology*, *42*, 1171-1196.